ORNL/TM-2019/1201
Revision 0

Safety Testing and Destructive Examination of AGR-2 UCO Compact 2-1-2

John D. Hunn
Tyler J. Gerczak
Robert N. Morris
Fred C. Montgomery
Darren J. Skitt
Brian D. Eckhart
Zachary M. Burns

June 2019

**Approved for public release.
Distribution is unlimited.**

OAK RIDGE NATIONAL LABORATORY
MANAGED BY UT-BATTELLE FOR THE US DEPARTMENT OF ENERGY

DOCUMENT AVAILABILITY

Reports produced after January 1, 1996, are generally available free via US Department of Energy (DOE) SciTech Connect.

Website www.osti.gov

Reports produced before January 1, 1996, may be purchased by members of the public from the following source:

National Technical Information Service
5285 Port Royal Road
Springfield, VA 22161
Telephone 703-605-6000 (1-800-553-6847)
TDD 703-487-4639
Fax 703-605-6900
E-mail info@ntis.gov
Website http://classic.ntis.gov/

Reports are available to DOE employees, DOE contractors, Energy Technology Data Exchange representatives, and International Nuclear Information System representatives from the following source:

Office of Scientific and Technical Information
PO Box 62
Oak Ridge, TN 37831
Telephone 865-576-8401
Fax 865-576-5728
E-mail reports@osti.gov
Website http://www.osti.gov/contact.html

This report was prepared as an account of work sponsored by an agency of the United States Government. Neither the United States Government nor any agency thereof, nor any of their employees, makes any warranty, express or implied, or assumes any legal liability or responsibility for the accuracy, completeness, or usefulness of any information, apparatus, product, or process disclosed, or represents that its use would not infringe privately owned rights. Reference herein to any specific commercial product, process, or service by trade name, trademark, manufacturer, or otherwise, does not necessarily constitute or imply its endorsement, recommendation, or favoring by the United States Government or any agency thereof. The views and opinions of authors expressed herein do not necessarily state or reflect those of the United States Government or any agency thereof.

ORNL/TM-2019/1201

Reactor and Nuclear Systems Division

SAFETY TESTING AND DESTRUCTIVE EXAMINATION OF AGR-2 UCO COMPACT 2-1-2

John D. Hunn
Tyler J. Gerczak
Robert N. Morris
Fred C. Montgomery
Darren J. Skitt
Brian D. Eckhart
Zachary M. Burns

Revision 0

Date Published: June 2019

Work sponsored by
US DEPARTMENT OF ENERGY
Office of Nuclear Energy - Advanced Reactor Technologies
under the
Advanced Gas Reactor Fuel Development and Qualification Program

Prepared by
OAK RIDGE NATIONAL LABORATORY
Oak Ridge, TN 37831-6283
managed by
UT-BATTELLE, LLC
for the
US DEPARTMENT OF ENERGY
under contract DE-AC05-00OR22725

CONTENTS

REVISION LOG

Revision	Date	Affected Pages	Revision Description
0		All	Initial issue

LIST OF FIGURES

LIST OF TABLES

ACRONYMS AND ABBREVIATIONS

3D	three dimensional
AGR	Advanced Gas Reactor (Fuel Development and Qualification Program)
AGR-1	first AGR program irradiation experiment
AGR-2	second AGR program irradiation experiment
BEC	backscattered electron/ secondary electron composite
BWXT	BWX Technologies
CCCTF	Core Conduction Cooldown Test Facility
CO	carbon monoxide
DLBL	deconsolidation and leach-burn-leach
EDS	energy-dispersive x-ray spectroscopy
EOL	end of life
FIMA	fissions per initial metal atom
HTGR	high temperature gas-cooled reactor
ID	identification
IFEL	Irradiated Fuels Examination Laboratory (hot cells)
IMGA	Irradiated Microsphere Gamma Analyzer
INL	Idaho National Laboratory
IPyC	inner pyrolytic carbon (TRISO layer)
M/C	measured vs. calculated (inventory fraction)
M/A	measured vs. average (inventory fraction)
MDL	minimum detection limit
OPyC	outer pyrolytic carbon (TRISO layer)
ORNL	Oak Ridge National Laboratory
PGS	Precision Gamma Scanner
PIE	post-irradiation examination
RS	randomly selected (particle)
SEI	secondary electron image
SEM	scanning electron microscope or scanning electron microscopy
SiC	silicon carbide (TRISO layer)
SP	special particle
TA_{min}	time-averaged minimum temperature
TA_{max}	time-averaged maximum temperature
TAVA	time-averaged/volume-averaged temperature
TRISO	tristructural-isotropic (coated particles)
UCO	uranium carbide/uranium oxide mixture (fuel kernels)
UO_2	uranium dioxide (fuel kernels)
XCT	x-ray computed tomography
Z	atomic number

ACKNOWLEDGMENTS

This work was sponsored by the US Department of Energy's Office of Nuclear Energy through the Idaho National Laboratory Advanced Reactor Technologies Technology Development Office as part of the Advanced Gas Reactor Fuel Development and Qualification Program. Analysis of leach solutions and Core Conduction Cooldown Test Facility furnace components was conducted by the Oak Ridge National Laboratory Nuclear Analytical Chemistry & Isotopics Laboratory. Hot cell activities were supported by the staff of the Oak Ridge National Laboratory Irradiated Fuels Examination Laboratory (IFEL).

1. INTRODUCTION AND BACKGROUND*

Post-irradiation examination (PIE) and elevated-temperature safety testing are being performed on tristructural-isotropic (TRISO) coated-particle fuel compacts from the Advanced Gas Reactor (AGR) Fuel Development and Qualification Program's second irradiation experiment (AGR-2). Details on this irradiation experiment have been previously reported (Collin 2014). The AGR-2 PIE effort builds upon the understanding acquired throughout the AGR-1 PIE campaign (Demkowicz et al. 2015) and is establishing a database for the different AGR-2 fuel designs.

The AGR-2 irradiation experiment included TRISO fuel particles coated at BWX Technologies (BWXT) with an engineering-scale coater, which had a coating chamber 150 mm in diameter. Two coating batches were tested in the AGR-2 irradiation experiment. Batch G73H-10-93085B had uranium dioxide (UO_2) kernels with an average diameter of 508 μm. Batch G83J-14-93073A had UCO kernels with an average diameter of 427 μm; in this kernel design, some of the uranium oxide is converted to uranium carbide during fabrication to provide a getter for oxygen liberated during fission and to limit CO production. Fabrication and property data for the AGR-2 coating batches have been compiled (Barnes and Marshall 2009) and compared to AGR-1 (Phillips, Barnes, and Hunn 2010). The AGR-2 TRISO coatings were most like the AGR-1 Variant 3 TRISO deposited in the Oak Ridge National Laboratory (ORNL) laboratory-scale coater, which had a coating chamber 50 mm in diameter (Hunn and Lowden 2006). In both cases, the hydrogen and methyltrichlorosilane coating gas mixture that was used to deposit the SiC was diluted with argon to produce a finer grained, more equiaxed SiC microstructure (Lowden 2006; Gerczak et al. 2016). In addition to the fact that AGR-1 fuel had smaller UCO kernels that were 350 μm in diameter, other notable differences in the TRISO particle properties included (1) the pyrocarbon anisotropy, which was slightly higher in the particles coated in the engineering-scale coater, and (2) the exposed kernel defect fraction, which was higher for AGR-2 fuel due to the detected presence of particles with impact damage that was introduced during TRISO particle handling (Hunn 2010).

Irradiation test compacts containing AGR-2 fuel particles were compacted at ORNL using the same blend of natural graphite, synthetic graphite, and phenolic resin that was used to make AGR-1 compacts and a modified pressing process that included a die heated to 65°C and a new computer-controlled servo press. Two compact lots were produced and qualified for the AGR-2 irradiation test: lot LEU09-OP2-Z contained the UCO TRISO particles (Hunn, Montgomery, and Pappano 2010a), and lot LEU11-OP2-Z contained the UO_2 fuel (Hunn, Montgomery, and Pappano 2010b). Unlike the AGR-1 compacts, which were compacted at room temperature using a manual press, the modified AGR-2 compacting process produced compacts with reduced variability in length and higher matrix density (1.6–1.7 g/cc for AGR-2 versus 1.2–1.3 g/cc for AGR-1). Compiled properties data for particles and compacts are available in pre-irradiation characterization summary reports for AGR-1 (Hunn, Savage, and Silva 2012) and AGR-2 (Hunn, Savage, and Silva 2010) fuel composites.

The *AGR-2 Post-Irradiation Examination Plan* (Demkowicz 2013) includes activities to (1) complete safety testing of irradiated compacts in the ORNL Core Conduction Cooldown Test Facility (CCCTF) and (2) perform post-safety-test destructive examination on these compacts to evaluate the effect of elevated temperature on fuel microstructure, individual particle coating failure, and overall fission product† and actinide retention. The safety tests typically involve heating compacts in flowing helium to maximum temperatures of 1,600, 1,700, or 1,800°C and holding at these temperatures for approximately 300 h. The standard test temperature of 1,600°C is the expected maximum temperature during a high-temperature gas-cooled reactor (HTGR) depressurization conduction-cooldown event, while tests with maximum temperatures of 1,700°C and 1,800°C explore the safety margin and provide additional data on

* The background text in this section was duplicated from a previous AGR-2 PIE report (Hunn et al. 2019) and is included herein for contextual information and definition of common terminology.

† In this report, the term *fission product* is used to collectively refer to all the various isotopes resulting from irradiation of the fuel compacts, namely, isotopes directly generated by the fission process, isotopes generated by neutron capture, and isotopes generated by radioactive decay.

mechanisms for particle coating failure, fission product and actinide diffusion, and other fission product and actinide interactions with the TRISO coatings.

Destructive PIE includes (1) deconsolidation and leach-burn-leach (DLBL) analysis for exposed fission products and actinides, (2) gamma surveys with short counting times performed using the ORNL Irradiated Gamma Microsphere Analyzer (IMGA) on all the recovered TRISO particles, (3) IMGA measurements with long counting times performed on special particles that have exhibited significant cesium release or other unusual radioisotope release, and (4) similar IMGA measurements performed on 40–60 randomly selected particles. After completing the IMGA measurements, microstructural analyses using x-ray microtomography and materialographic methods are performed to investigate radiation-induced changes in the particles and to elucidate the mechanisms responsible for observed fission product and actinide release. Materialographic methods typically include mechanical polishing of particle cross section, imaging with an optical microscope, imaging with a scanning electron microscope (SEM), and atomic analysis via energy-dispersive x-ray spectroscopy (EDS).

Previously reported results are available for many AGR-2 compacts. Destructive PIE after safety testing of AGR-2 UO_2 Compacts 3-3-2 and 3-4-2 at 1,600°C (Hunn et al. 2015) and AGR-2 UO_2 Compacts 3-4-1 at 1,700°C (Hunn et al. 2018a) confirmed cesium release from multiple particles in these UO_2 compacts due to CO corrosion. In contrast, 1,600°C safety testing of AGR-2 UCO Compacts 2-2-2, 2-3-1, 5-2-2, and 6-4-2 (Hunn et al. 2016a; Hunn et al. 2017) showed no indications of cesium release related to SiC failure, and there was most likely only one failed particle that released cesium in each of the previous two 1,800°C safety tests of AGR-2 UCO compacts. The 1,800°C safety test of AGR-2 UCO Compact 5-4-1 induced SiC failure in one particle as a result of palladium degradation; this was similar to the type of failure most often observed in AGR-1 safety testing (Hunn et al. 2016a; Hunn et al. 2018a; Hunn et al. 2014). The 1,800°C safety test of AGR-2 UCO Compact 2-3-2 showed cesium and krypton release from a particle with TRISO failure that was caused by molybdenum inclusion in the coating layers during TRISO deposition. Recently reported results from 1,800°C safety testing of AGR-2 UCO Compact 6-4-3, which was irradiated a lower average temperature and burnup than all other AGR compacts irradiated to date, appeared to have no failed particles (Hunn et al. 2019).

This report presents and discusses results from 1,800°C safety testing and post-safety-test destructive examination of AGR-2 UCO Compact 2-1-2. This compact came from Capsule 2, which was intentionally run at higher irradiation temperature to explore the upper regions of the fuel operating temperatures in a typical HTGR. Table 1-1 shows the calculated average burnup in percent fissions per initial metal atom (FIMA), the fast neutron fluence (neutron energies > 0.18 MeV), and the average compact temperatures during irradiation.

Table 1-1. Irradiation conditions for AGR-2 UCO Compact 2-1-2 discussed in this report

Compact ID [a]	Fabrication ID [b]	Fuel type	Average burnup [c] (FIMA)	Fast fluence [c] (E>0.18 MeV)	Temperature [d]		
					TAVA	TA_{min}	TA_{max}
AGR-2 2-1-2	LEU09-OP2- Z079	UCO	12.62%	3.25×10^{25} n/m^2	1,219°C	1,055°C	1,324°C

[a] The X-Y-Z compact identification (ID) numbering convention denotes the compact's location in the irradiation test train: *capsule-level-stack*.

[b] Physical properties data for individual compacts are available and referenced by fabrication ID (Hunn, Montgomery, and Pappano 2010a, 60–69).

[c] Burnup (Sterbentz 2014, Table 6) and fast fluence (Sterbentz 2014, Table 12) are based on physics calculations.

[d] Time-averaged, volume-averaged (TAVA) temperature, time-averaged minimum (TA_{min}) temperature, and time-averaged maximum (TA_{max}) temperature are based on thermal calculations (Hawkes 2014, Table 3).

2. EXPERIMENTAL METHODS*

2.1 SAFETY TESTING METHODS

Safety testing in the CCCTF furnace was accomplished using the same methods that were used for AGR-1 safety testing (Baldwin et al. 2012). Compacts were placed in a graphite holder that positions the compact in the furnace and simulates the graphite that surrounds the compacts in a prismatic block reactor. A water-cooled deposition cup located near the top of the tantalum-lined furnace chamber collected vaporized metallic elements that escaped from the compact and the surrounding graphite holder. Deposition cups were periodically removed and replaced with new cups using a maximum exchange interval of ~24 h, and shorter exchange intervals were used for the first few cups removed after heating up to the test temperature. The cups were monitored with gamma spectrometry to track safety test progress, with particular emphasis on the collected cesium inventory that would indicate SiC failure (Hunn et al. 2014). Gaseous fission products were collected from the helium sweep gas as it passed through a trap cooled with liquid nitrogen. The trap was monitored for ^{85}Kr, because significant krypton release would indicate complete failure of a TRISO coating (Morris et al. 2014). After each safety test was completed, additional analysis was performed to measure fission products on the deposition cups and other CCCTF furnace internals (graphite fuel holder, tantalum furnace liner, and tantalum gas inlet line). These data were used to determine the cumulative release of each detected fission product from the compact.

Fission product and actinide measurements were converted to fractions of the total compact inventory using the standard ORNL AGR PIE approach (Hunn et al. 2013, page 6). This method uses the total compact inventory of each isotope that was estimated by performing physics calculations (Sterbentz 2004) to determine the inventory at three specific times after the end of the irradiation, also called the *end of life* (EOL): one day after, one year after, and two years after. Radioisotope quantities measured by gamma spectrometry (e.g., ^{85}Kr, ^{110m}Ag, ^{134}Cs, ^{137}Cs, ^{154}Eu, and ^{155}Eu) or chemical separation and beta spectrometry in the special case of ^{90}Sr, were decay-corrected to one day after EOL and divided by the calculated total inventory at that time to determine the total inventory fraction. For stable isotopes such as ^{104}Pd and for actinides (e.g., ^{235}U, ^{236}U, ^{238}U, ^{239}Pu, and ^{240}Pu), the measured quantity was divided by the calculated total inventory at one year after EOL. This was done because many stable isotope inventories increased significantly over the first year after the compacts were removed from the reactor, while any further increase in the calculated inventories after one year was typically negligible, and the mass spectrometry analysis was almost always performed after one year based on the time required for the test train to cool down and be disassembled. Sometimes results were calculated in terms of the equivalent particle inventory or number of *particle-equivalents*, which is simply the total compact inventory fraction multiplied by the average number of particles per compact: 3,176 for AGR-2 UCO compacts (Hunn 2010).

The efficiency of collection from the deposition cup varied for different elements due to the variability in transport of elements out of the graphite holder and onto the water-cooled cups. The cumulative fraction of each fission product measured on the deposition cups—relative to the total measured on the cups, tantalum internals, and graphite holder at the end of each safety test—provided a measure of the average deposition cup collection efficiency, which is expected to have varied with time. However, this time dependence could not be determined by a single measurement at the end of the test. To estimate the time-dependent release of fission products from the compact, the collection efficiency was assumed to be constant and was used to scale the individual cup measurements. This standard method usually provides a fairly good estimate for some of the more volatile elements such as cesium and silver, but it is often inaccurate for other elements like europium and strontium, which are known to transport relatively slowly onto the deposition cups. Elements that transport slowly onto the deposition cups with respect to the deposition cup exchange interval may appear to have a greater time-dependent increase in the release rate,

* This experimental methods section was duplicated from a previous AGR-2 PIE report (Hunn et al. 2019) and included herein for contextual information and definition of common terminology.

especially in the early stages of the safety test, due to the assumption of constant cup collection efficiency.

2.2 DLBL AND IMGA METHODS

Post-safety test destructive examination was performed using the same methods that were developed for destructive PIE of as-irradiated AGR-1 compacts, and the details of the equipment and methods have been previously reported (Hunn et al. 2013). Figure 2-1 shows the typical process flow for DLBL and IMGA survey. Deconsolidation and hot leach solutions were analyzed by gamma and mass spectrometry, providing information about fission products and actinides that were not sealed inside retentive SiC layers. Fission products and actinides leached in the deconsolidation acid, pre-burn Soxhlet extraction of the particles and matrix, and post-burn pot leach of the matrix came from either (1) uranium contamination outside the SiC in the as-fabricated compacts, (2) diffusion through the SiC during irradiation or safety testing, or (3) exposed kernels in particles with *failed TRISO*. Fission products and actinides leached in the post-burn Soxhlet extraction of the particles came from either (1) exposed kernels in particles with *failed SiC*, or (2) diffusively released fission products and actinides that were not leached prior to the burn because they were previously sequestered in the outer pyrolytic carbon (OPyC) layer or in an insoluble chemical form.

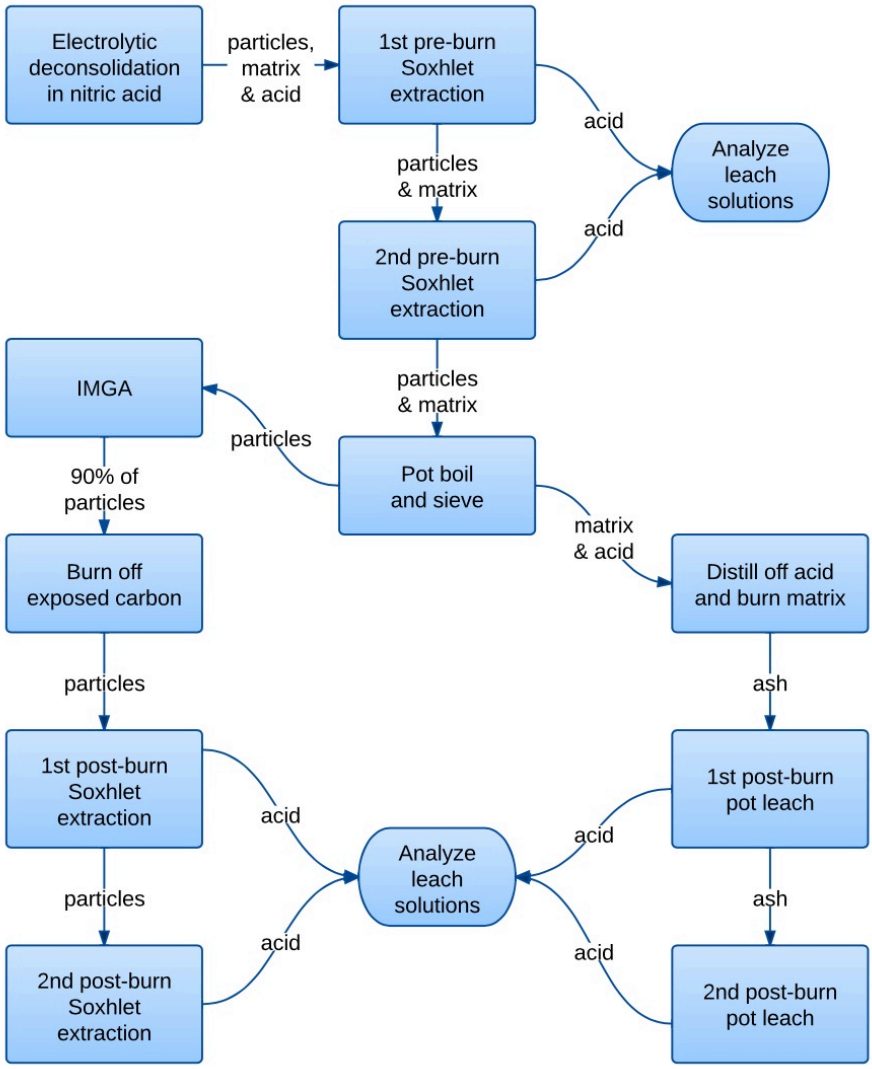

Figure 2-1. Process flow for DLBL and IMGA.

The DLBL data were decay-corrected and converted to compact inventory fraction and particle-equivalent values using the same protocol applied to the safety test data. The IMGA data are reported herein as activities in Bq/particle that were decay-corrected to one day after EOL or various unitless ratios that communicate the retained fraction of each isotope. The simplest ratio was the measured activity of a particle, A_i, normalized to the average measured activity for all particles in a sample of n particles. For example,

$$\frac{A_i(^{144}Ce)}{\sum_{i=1}^{n}\left(\frac{1}{n}\right)A_i(^{144}Ce)} \tag{2.1}$$

is the measured ^{144}Ce activity of Particle i, normalized to the average ^{144}Ce activity. Equation 2.1 was used to generate ^{137}Cs and ^{144}Ce histograms of the IMGA survey results, which were centered on unity and had a distribution that resulted from measurement uncertainty and real particle-to-particle variation in isotopic content. For particles with negligible radioisotope release, this real particle-to-particle variation was related to variation in fissionable material and burnup, which might occur due to variation in kernel size and local neutron fluence.

A calculated value for the expected activity of a given isotope in each particle was estimated from the calculated compact activity for that isotope multiplied by the normalized activity of a different and preferably well-retained isotope to adjust for particle-to-particle variation in fissionable material and burnup. For instance,

$$A_{calc}(^{137}Cs)\,\frac{A_i(^{144}Ce)}{\sum_{i=1}^{n}\left(\frac{1}{n}\right)A_i(^{144}Ce)} \tag{2.2}$$

is the calculated ^{137}Cs activity of Particle i adjusted for particle-to-particle variation in fissionable material and burnup using the normalized ^{144}Ce activity. The ratio of the measured activity in a particle vs. the calculated expected activity is reported herein as the measured vs. calculated (M/C) value. For example,

$$\frac{A_i(^{137}Cs)}{A_{calc}(^{137}Cs)\frac{A_i(^{144}Ce)}{\sum_{i=1}^{n}\left(\frac{1}{n}\right)A_i(^{144}Ce)}} \tag{2.3}$$

is the ^{137}Cs M/C value for Particle i. Equation 2.3 was used to generate a ^{137}Cs M/C histogram that illustrated the cesium retention in each particle, where particles with low cesium retention could be identified as discrete values below the main distribution. The M/C values were also calculated for other isotopes as useful indicators of particle retention. The average M/C for well-retained isotopes was not always close to unity, because error in the calculated inventory sometimes resulted in an offset which could be significant. The offset was substantial for the isotopes of europium and antimony as a result of large errors in the calculated values.

Another calculated ratio, reported herein as the measured vs. average (M/A) value, was determined in a manner similar to that used to determine M/C, except the offset in the calculated activity was mostly removed by replacing the calculated activity in Equation 2.3 with the average measured activity. For instance,

$$\frac{A_i(^{137}Cs)}{\sum_{i=1}^{n}\left(\frac{1}{n}\right)A_i(^{137}Cs)\frac{A_i(^{144}Ce)}{\sum_{i=1}^{n}\left(\frac{1}{n}\right)A_i(^{144}Ce)}} \tag{2.4}$$

is the ^{137}Cs M/A value for Particle i. This is useful for identifying particles with average retention.

2.3 SEM AND EDS METHODS

Analysis was performed with a JEOL JSM-6390L SEM equipped with an Oxford X-Max 50 silicon drift detector and the Oxford AZtec analysis software suite for EDS. The SEM was located in a contamination control area in Room 120 of the ORNL IFEL hot cells. The SEM analysis was performed on the mounts previously imaged by optical microscopy. To facilitate analysis, the mounts were transferred out of the hot cell to the IFEL charging area, where initial decontamination was performed to reduce radiological contamination. The mounts were then transferred to a radiological hood located in Room 120 for final radiological decontamination and surface cleaning. The mounts underwent ultrasonic cleaning in deionized water, were rinsed with isopropyl alcohol, and were wiped with a cotton swab. These cleaning and decontamination processes were repeated three times. Following decontamination, the samples were smeared and surveyed prior to being released from the hood. After the samples were released, their surfaces were checked with an optical microscope located in the contamination control area. If the sample surfaces were free of significant debris, then they were secured onto an aluminum SEM stub using conductive carbon tape and colloidal graphite to facilitate SEM analysis.

Two complementary SEM imaging modes—secondary electron imaging (SEI) and backscattered electron composition (BEC)—were performed, as they provide different information on particle cross sections. The secondary electron signal was surface sensitive, which allowed for identification of surface features and any irregularities. The SEI micrographs were obtained using a 3-kV accelerating voltage with a spot size of 40 (a unitless value) and a working distance of 8 mm. The backscattered electron signal was dependent on the atomic number (Z) of the elements near the surface. Because they appeared as bright spots, the high-Z fission products and actinides embedded in the relatively low-Z TRISO layers could be readily identified. The BEC micrographs were obtained using a 20-kV accelerating voltage with a spot size of 64 and a working distance of 10 mm. Image pairs of the same areas were acquired using both imaging modes to ensure that surface features (such as loose debris) were not misinterpreted as embedded features. A general image set was taken for each particle cross section. The image set consisted of particle overview images, low magnification (500×) images of the TRISO layers in four cardinal directions, and higher magnification (1,500×) images of the SiC layer in four cardinal and four inter-cardinal directions around the circumference of the particle. Additional images of selected areas of interest were also acquired when necessary.

Two or more locations were chosen on each particle cross section for EDS analysis to gain an understanding of the distribution of fission products and actinides in the TRISO layers after irradiation and safety testing. Point-ID analysis was used to identify local compositions in high-Z features. The Point-ID analysis was acquired under the same conditions as images acquired in the BEC mode, which resulted in a sufficient count rate. The general acquisition parameters used for Point-ID analysis were to collect spectra within an energy range of 0–20 keV with 10 eV/channel, 4,096 channels, a unitless process time of 2, and a live time of 30 s. Data acquired by Point-ID analysis were processed using standardless analysis, and significant contributions from the surrounding matrix were included in the data due to the submicron size of the analyzed features; therefore, information on feature composition was not quantitative. In addition, minor constituents present in the high-Z fission product and actinide features may not be observed. However, the Point-ID analysis information on feature composition was useful for qualitative classification of the features, which supported identification of general trends and comparison of the features observed in different locations in the TRISO layers.

3. SAFETY TEST RESULTS

Figure 3-1 shows the estimated time-dependent release of various fission product isotopes during 1,800°C safety testing of Compact 2-1-2. Table 3-1 shows the cumulative release and the relative fractions of these fission products on the furnace internals at the end of the safety test. As described in Section 2.1, the relative fraction of each isotope on the deposition cups was used to estimate the average collection efficiency for each isotope, and these estimated values were used to generate the time-dependent curves presented in Figure 3-1. Collection efficiencies were very high for palladium, silver, and cesium. Strontium and europium collection efficiencies were also high relative to many CCCTF tests, but some strontium and europium were held up in the graphite holder and on the tantalum components, as expected. Cesium release midway through the safety test was indicative of at least one particle with a failed SiC layer but at least one intact pyrocarbon layer, given that the ^{85}Kr release remained low. Strontium, palladium, silver, and europium releases were typical for a Capsule 2 compact and are discussed in the following sections.

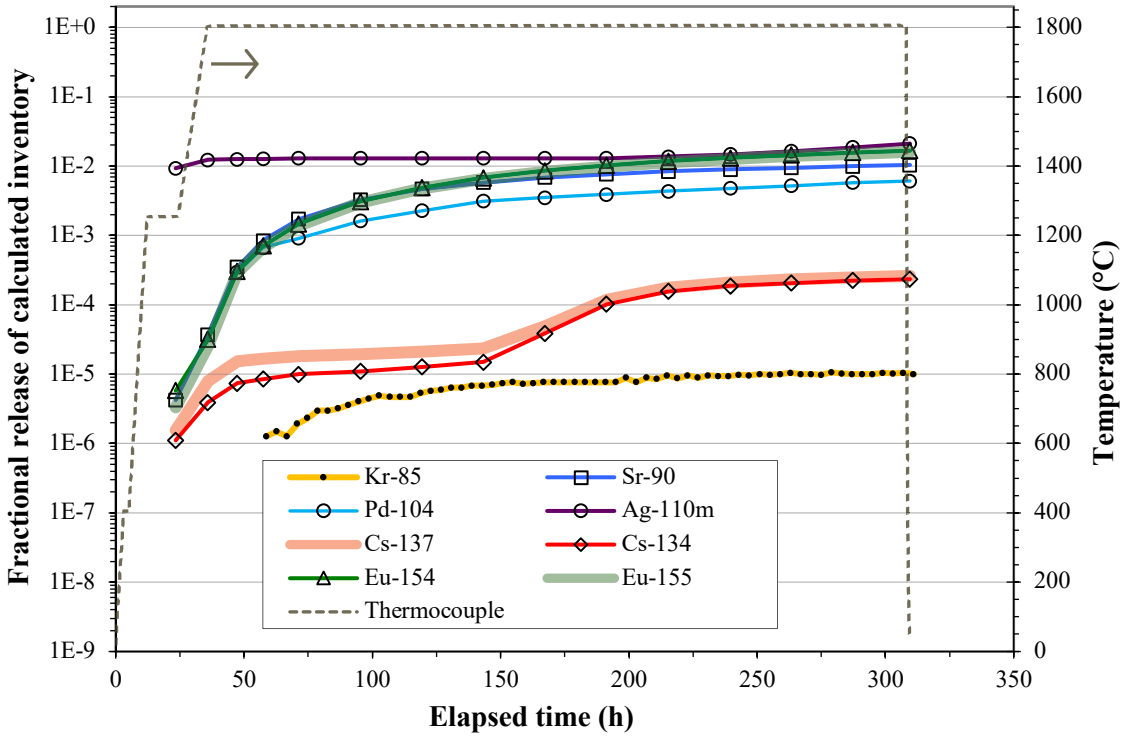

Figure 3-1. Release of fission products from Compact 2-1-2 during safety testing to 1,800°C.

Table 3-1. Fission product distribution on furnace internal components after the safety test

Component	^{90}Sr	^{104}Pd	^{110m}Ag	^{134}Cs	^{137}Cs	^{154}Eu	^{155}Eu
Deposition cups [a]	91%	~100%	~100%	98%	98%	74%	70%
Tantalum parts	2.7%	~0%	~0%	1.8%	1.7%	5.7%	7.0%
Graphite holder	6.3%	~0%	~0%	0.16%	0.67%	20%	23%
Cumulative release [b]	1.04E-2 (33)	6.09E-3 (19)	2.10E-2 (67)	2.34E-4 (0.74)	2.61E-4 (0.83)	1.67E-2 (53)	1.61E-2 (51)

[a] Cumulative fraction collected on all deposition cups.
[b] Release from compact as fraction of calculated compact inventory and particle-equivalent inventory (in parentheses).

3.1 CESIUM AND KRYPTON RELEASE DURING SAFETY TESTING

A few percent of one particle-equivalent of cesium was released as the compact was heated up and then held at 1,800°C for about 100 h (Figure 3-1). Figure 3-2 shows that the rate of cesium release dropped after peaking during the third cup residence period, which was removed after the furnace was at test temperature for ~12 h. The cesium collection rate reached a minimum value during the sixth cup residence period (72–95 h at 1,800°C), and then it increased very slightly for the next two cups (95–143 h at 1,800°C). This was followed by a sharp increase in the cesium release rate to the ninth cup sometime during the next 24 h. The initial release of cesium as the compact was heated to test temperature, because it only reached 2–3% of one particle-equivalent of cesium, did not indicate SiC failure. This initial release of cesium may have come from contamination picked up in the hot cell during handling of the graphite holder and/or low levels of cesium sequestered in the matrix and/or OPyC of the irradiated compact. The order-of-magnitude increase in release rate between 143–167 h indicated that significant cesium release through degraded SiC began during the period that the ninth cup was in the furnace. However, the barely discernable rate increase on the two preceding cups could possibly have been related to the onset of SiC failure. The cesium release rate remained high for several days after the initial sharp increase, but there was no additional step-like change in the release rate curve as sometimes occurs when multiple particles fail during separate cup residence periods. The release rate over the final 100 h of the test indicated that there was no further SiC failure during this period. The total ^{134}Cs release was equivalent to the 74% of the average inventory in one particle (Table 3-1). The shape of the release rate curve and the total amount of cesium released were consistent with either a single particle failure or perhaps two particles failing simultaneously. Additional examination discussed later in this report points to single particle failure.

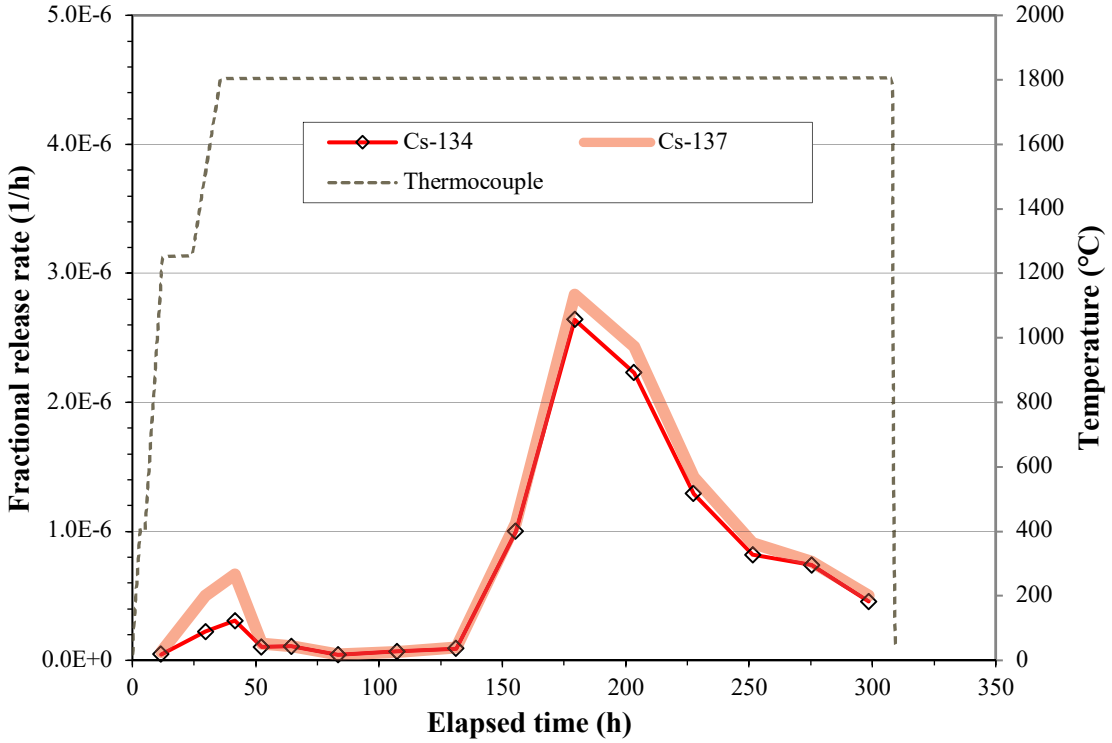

Figure 3-2. Rate of cesium release from Compact 2-1-2 during safety testing to 1,800°C.

About 3% of one particle-equivalent of ^{85}Kr was released during the Compact 2-1-2 safety test, and some of this was likely related to diffusion of krypton through the degraded SiC responsible for the cesium release. However, the total release fraction of ^{85}Kr indicates that there were no particles with full TRISO failure.

3.2 SILVER RELEASE DURING SAFETY TESTING

Gamma scanning of Compact 2-1-2 with the Idaho National Laboratory (INL) Precision Gamma Scanner (PGS) (Harp et al. 2014) prior to safety testing determined that the compact retained 19.8% of the calculated ^{110m}Ag inventory at the end of irradiation (Harp, Demkowicz, and Stempien 2016). This can be considered the starting inventory for ^{110m}Ag in the compact at the beginning of the safety test. Figure 3-1 shows 1.2% of the calculated ^{110m}Ag inventory was released as the compact was heated to 1,800°C, presumably from silver that was sequestered in the matrix and/or OPyC. After about 60 h at 1,800°C, the release rate dropped to a negligible value, and no additional silver came out until the compact had been at 1,800°C for ~160 h, at which point additional silver was released at an increasing rate throughout the remainder of the test (Figure 3-3). This is consistent with the observed delay for diffusive release of silver at 1,800°C in AGR-1 and AGR-2 compacts with SiC deposited with an argon-diluent (Morris et al 2014, Hunn et al. 2018b). The total ^{110m}Ag release from Compact 2-1-2 during 1,800°C safety testing was 2.1% of the calculated inventory (Table 3-1).

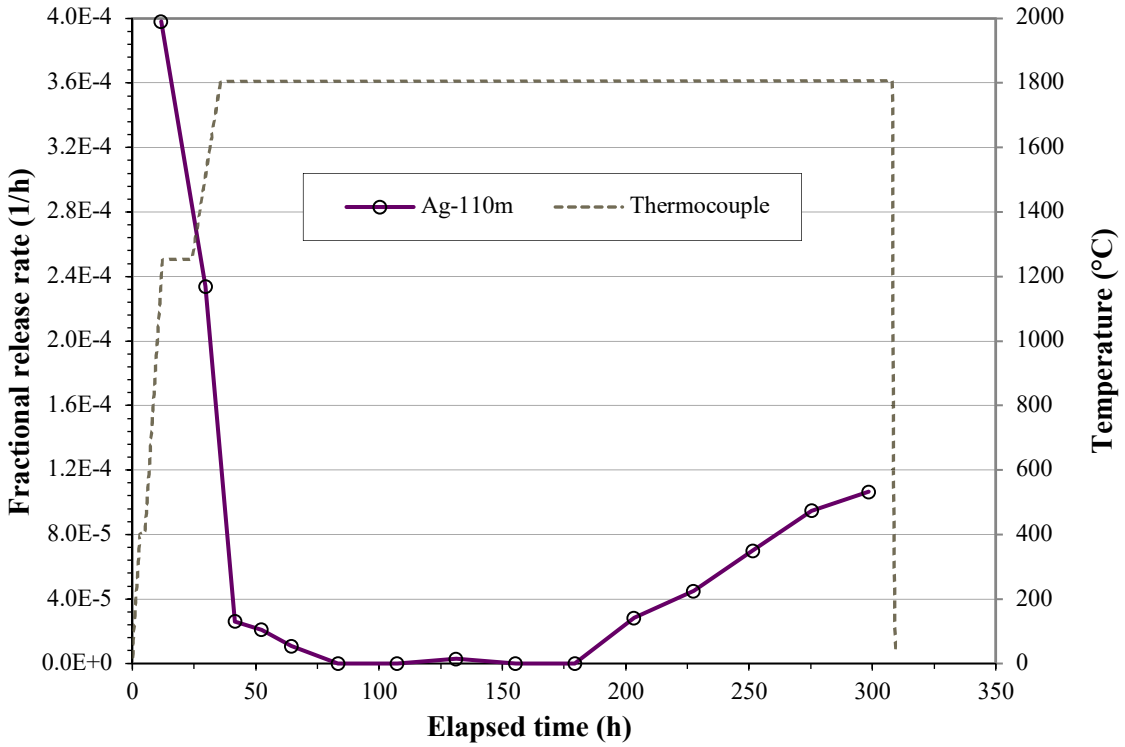

Figure 3-3. Rate of ^{110m}Ag release from Compact 2-1-2 during safety testing to 1,800°C.

3.3 STRONTIUM, EUROPIUM, AND PALLADIUM RELEASE DURING SAFETY TESTING

Analysis of the Capsule 2 graphite holder revealed that significant amounts of ^{90}Sr and ^{154}Eu were released from the compacts in that capsule during irradiation as a result of the relatively high irradiation temperature. The reported amount of ^{90}Sr on the graphite holder was 1.24% of the Capsule 2 inventory, and the reported amount for ^{154}Eu was 3.70% of the capsule inventory (Stempien and Demkowicz). Releases during safety testing and DLBL of as-irradiated AGR-2 Capsule 2 compacts have shown that these compacts also had significant amounts of strontium and europium sequestered in the matrix and/or OPyC at the end of irradiation (Hunn et al. 2018b). Figure 3-1 and Figure 3-4 show the typical safety test release behavior for ^{90}Sr, ^{154}Eu, and ^{155}Eu, where the collection rate slowly increases over the first several days of the test as strontium and europium slowly migrate out of the compact, through the graphite holder, and eventually collect on the deposition cups. The ^{90}Sr release rate peaked after ~60 at 1,800°C and the ^{154}Eu and ^{155}Eu peaked after ~100 h at 1,800°C. The subsequent reduction in release rate indicated depletion of the concentration of these fission products in the matrix and OPyC. If there were any

contributions to strontium and europium release from diffusion through the SiC layers, then they could not be resolved above the already high releases. The cumulative ^{90}Sr release during the 1,800°C safety test of Compact 2-1-2 was ~1% of the calculated inventory, and the europium release was 1.6–1.7% (Table 3-1).

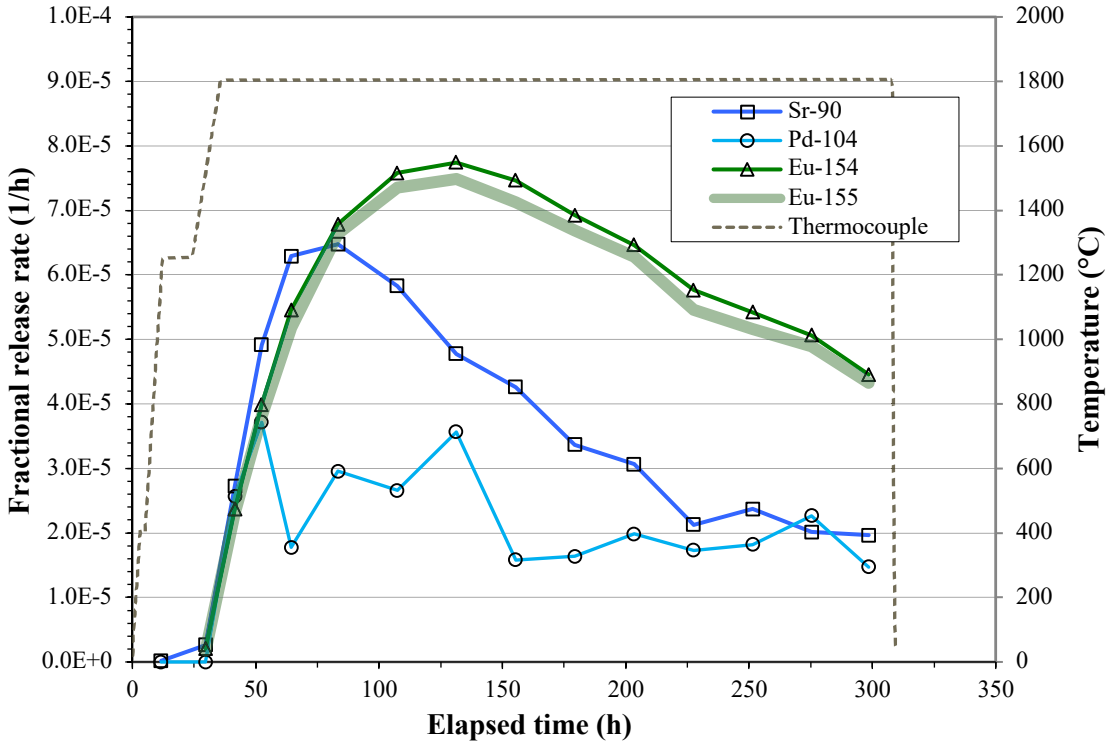

Figure 3-4. Rate of ^{90}Sr, ^{104}Pd, ^{154}Eu, and ^{155}Eu release from Compact 2-1-2 during safety testing to 1,800°C.

While palladium is of great interest because of its observed interactions with SiC, it is often not thoroughly tracked during safety testing because of its high detection limit for measurement by mass spectrometry. Measurement of the ^{105}Pd isotope normally tracked during DLBL analysis is hampered in analysis of the deposition cup leachate because of a $^{65}Cu^{40}Ar^{+}$ interference that forms in the mass spectrometer plasma (the CCCTF deposition cups are copper coated), therefore the ^{104}Pd isotope has been chosen for analysis of palladium release in the CCCTF. Palladium release during 1,800°C safety testing of Compact 2-1-2 was high enough to obtain a quantitative analysis on all but the first two deposition cups, which was unusual for CCCTF safety testing. Figure 3-1 shows the accumulation of ^{104}Pd throughout the 1,800°C hold, with a final cumulative release of 0.6% of the calculated inventory. The level and time dependence of ^{104}Pd release from 1,800°C safety-tested AGR-2 Compact 2-1-2 was similar to that reported for 1,800°C safety-tested AGR-1 Compact 5-1-3 (Hunn et al. 2013b).

4. DECONSOLIDATION AND LEACH-BURN-LEACH ANALYSIS

Electrolytic deconsolidation and acid leaching were performed after safety testing to recover the particles for IMGA survey and analyze for exposed actinides and fission products remaining in the compact. The measured amounts of several uranium and plutonium isotopes are shown in Table 4-1. Uranium isotopes in the deconsolidation acid, in the pre-burn leach of the particles and matrix debris, and in the post-burn leach of the matrix can be good indicators of whether there were any exposed kernels in a deconsolidated compact. For Compact 2-1-2, the levels of uranium detected in these leachates were too low to have come from a particle with failed TRISO, which is consistent with the conclusion that there were no failed TRISO particles based on the measured ^{85}Kr release during safety testing. Similarly, the measured amounts of uranium isotopes in the post-burn particle leaches were not high enough to have come from a particle with failed SiC. It may be presumed that the measured uranium and plutonium were from diffusive release through intact SiC during irradiation and/or safety testing. Given the relatively high temperatures of both the irradiation and safety test, it is conceivable that these actinides were released through the SiC in both cases.

Table 4-1. Exposed U and Pu detected by DLBL

DLBL step	^{235}U	^{236}U	^{238}U	^{239}Pu	^{240}Pu
Deconsolidation acid	3.54E-5 (0.113)	3.30E-5 (0.105)	3.36E-5 (0.107)	1.53E-4 (0.485)	2.14E-4 (0.679)
Pre-burn leach 1	1.89E-5 (0.060)	1.70E-5 (0.054)	1.86E-5 (0.059)	2.02E-4 (0.641)	2.81E-4 (0.891)
Pre-burn leach 2	7.04E-6 (0.022)	6.50E-6 (0.021)	7.51E-6 (0.024)	2.62E-5 (0.083)	3.78E-5 (0.120)
Post-burn matrix leach 1	5.65E-5 (0.180)	5.11E-5 (0.162)	6.26E-5 (0.199)	3.62E-4 (1.148)	4.84E-4 (1.537)
Post-burn matrix leach 2	3.82E-7 (0.0012)	3.61E-7 (0.0011)	7.31E-7 (0.0023)	2.14E-6 (0.007)	2.93E-6 (0.009)
Post-burn particle leach 1 [a]	8.61E-5 (0.273)	7.45E-5 (0.237)	9.16E-5 (0.291)	3.66E-4 (1.163)	4.88E-4 (1.551)
Post-burn particle leach 2 [a]	2.63E-6 (0.008)	2.22E-6 (0.007)	4.15E-6 (0.013)	1.60E-5 (0.051)	2.28E-5 (0.073)
Total	2.07E-4 (0.66)	1.85E-4 (0.59)	2.19E-4 (0.70)	1.13E-3 (3.58)	1.53E-3 (4.86)

Note: Values are reported as compact inventory fraction and equivalent-particle inventory (in parentheses).
[a] The measured post-burn particle leach data were divided by 2,724/3,176 to account for the fraction of particles included in the analysis.

Table 4-2 and Table 4-3 show some of the radioactive and stable isotopes detected in the leachates, respectively. Comparison of Table 3-1 to Table 4-2 shows that the amounts of ^{90}Sr, ^{110m}Ag, ^{134}Cs, ^{137}Cs, ^{154}Eu, and ^{155}Eu remaining in the compact matrix and/or OPyC at the end of the safety test were only a small fraction of what was released during the test.

Table 4-2. Exposed compact inventory fractions [a] of typically tracked beta/gamma-emitting fission products detected by DLBL

DLBL step	^{90}Sr [a]	^{106}Ru	^{110m}Ag	^{125}Sb	^{134}Cs	^{137}Cs	^{144}Ce	^{154}Eu	^{155}Eu
Deconsolidation acid	6.49E-5 (0.206)	<8.80E-7 (<0.003)	<1.44E-4 (<0.458)	<1.37E-6 (<0.004)	5.27E-8 (0.0002)	7.51E-7 (0.0024)	3.13E-5 (0.099)	6.46E-5 (0.205)	7.80E-5 (0.248)
Pre-burn leach 1	1.30E-4 (0.413)	<2.04E-6 (<0.006)	<3.00E-4 (<0.953)	<2.74E-6 (<0.009)	<1.06E-7 (<0.0003)	3.88E-7 (0.0012)	1.57E-4 (0.499)	2.36E-4 (0.750)	2.86E-4 (0.908)
Pre-burn leach 2	1.16E-5 (0.037)	<1.48E-6 (<0.005)	<2.19E-4 (<0.694)	<2.52E-6 (<0.008)	<8.62E-8 (<0.0003)	5.35E-7 (0.0017)	1.61E-5 (0.051)	2.86E-5 (0.091)	3.51E-5 (0.111)
Post-burn matrix leach 1	1.19E-4 (0.377)	<2.16E-6 (<0.007)	<3.55E-4 (<1.128)	1.11E-5 (0.035)	4.16E-6 (0.013)	9.25E-6 (0.029)	2.72E-4 (0.862)	4.85E-4 (1.540)	5.59E-4 (1.777)
Post-burn matrix leach 2	8.20E-7 (0.003)	<4.51E-7 (<0.0014)	<6.36E-5 (<0.202)	<8.30E-7 (<0.003)	8.68E-7 (0.0003)	3.45E-7 (0.0011)	1.20E-6 (0.004)	2.38E-6 (0.008)	2.74E-6 (0.009)
Post-burn particle leach 1 [b]	1.17E-4 (0.372)	1.71E-5 (0.054)	<6.41E-4 (<2.036)	1.56E-5 (0.050)	5.46E-6 (0.017)	1.33E-5 (0.042)	2.01E-4 (0.639)	3.10E-4 (0.984)	3.87E-4 (1.230)
Post-burn particle leach 2 [b]	6.32E-6 (0.020)	<2.36E-6 (<0.008)	<3.02E-4 (<0.960)	<4.66E-6 (<0.015)	1.56E-6 (0.005)	3.59E-6 (0.011)	7.51E-6 (0.024)	1.34E-5 (0.043)	1.48E-5 (0.047)
Total	4.50E-4 (1.43)	1.71E-5 (0.054)		2.67E-5 (0.085)	1.13E-5 (0.036)	2.81E-5 (0.089)	6.86E-4 (2.18)	1.14E-3 (3.62)	1.36E-3 (4.33)

Note: Values are reported as compact inventory fraction and equivalent-particle inventory (in parentheses).
Note: A less-than value indicates that the concentration in the leachate was below the minimum detectable limit; these values are not included in the totals.
[a] Chemical separation and beta analysis were used to measure ^{90}Sr; other isotopes were measured by gamma spectrometry.
[b] The measured post-burn particle leach data were divided by 2,724/,3176 to account for the fraction of particles included in the analysis.

Table 4-3. Exposed compact inventory fractions [a] of stable isotopes of interest detected by DLBL

DLBL Step	^{105}Pd	^{109}Ag	^{133}Cs	^{139}La	^{140}Ce	^{141}Pr	^{146}Nd	^{152}Sm	^{153}Eu	^{156}Gd
Deconsolidation acid	<1.31E-5 (<0.042)	3.30E-5 (0.105)	1.60E-6 (0.005)	6.07E-5 (0.193)	5.91E-5 (0.188)	4.42E-5 (0.140)	3.23E-5 (0.103)	4.71E-5 (0.150)	9.06E-5 (0.288)	5.97E-4 (1.896)
Pre-burn leach 1	<1.61E-5 (<0.051)	3.53E-5 (0.112)	1.60E-6 (0.005)	2.36E-4 (0.750)	3.09E-4 (0.980)	1.61E-4 (0.512)	1.19E-4 (0.378)	1.77E-4 (0.562)	3.02E-4 (0.959)	2.10E-3 (6.678)
Pre-burn leach 2	<2.79E-5 (<0.089)	<2.90E-5 (<0.092)	<1.13E-6 (<0.004)	2.73E-5 (0.087)	3.84E-5 (0.122)	1.79E-5 (0.057)	1.34E-5 (0.042)	1.77E-5 (0.056)	4.71E-5 (0.150)	2.27E-4 (0.720)
Post-burn matrix leach 1	1.63E-5 (0.052)	1.03E-4 (0.328)	1.14E-5 (0.036)	4.22E-4 (1.341)	5.08E-4 (1.615)	2.95E-4 (0.938)	2.20E-4 (0.699)	2.55E-4 (0.811)	6.20E-4 (1.969)	2.64E-3 (8.374)
Post-burn matrix leach 2	<1.32E-5 (<0.042)	<1.37E-5 (<0.044)	<5.31E-7 (<0.002)	2.30E-6 (0.007)	1.01E-5 (0.032)	1.58E-6 (0.005)	1.19E-6 (0.004)	<4.75E-6 (<0.015)	<6.69E-6 (<0.021)	1.64E-5 (0.052)
Post-burn particle leach 1 [a]	<2.56E-5 (<0.081)	6.29E-5 (0.200)	1.59E-5 (0.051)	3.12E-4 (0.992)	3.60E-4 (1.144)	2.14E-4 (0.681)	1.60E-4 (0.508)	1.96E-4 (0.622)	4.26E-4 (1.354)	2.27E-3 (7.194)
Post-burn particle leach 2 [a]	<2.63E-5 (<0.083)	<2.73E-5 (<0.087)	3.74E-6 (0.012)	9.34E-6 (0.030)	1.48E-5 (0.047)	6.68E-6 (0.021)	5.68E-6 (0.018)	<9.48E-6 (<0.030)	1.73E-5 (0.055)	5.95E-5 (0.189)
Total	1.63E-5 (0.052)	2.35E-4 (0.74)	3.43E-5 (0.11)	1.07E-3 (3.40)	1.30E-3 (4.13)	7.41E-4 (2.35)	5.52E-4 (1.75)	6.93E-4 (2.20)	1.50E-3 (4.77)	7.90E-3 (25.10)

Note: Values are reported as compact inventory fraction and equivalent-particle inventory (in parentheses).
Note: A less-than value indicates that the concentration in the leachate was below the minimum detectable limit; these values are not included in the totals.
[a] The measured post-burn particle leach data were divided by 2,724/3,176 to account for the fraction of particles included in the analysis.

5. IMGA MEASUREMENTS

5.1 IMGA SURVEY OF DECONSOLIDATED TRISO PARTICLES

An IMGA survey of all available particles was performed to find any particles with low cesium or cerium inventory. The deconsolidated material separated from the fine matrix debris by sieving included 3,089 TRISO particles with no remaining spots or only small localized spots of matrix remaining on the surface of the OPyC. There was also a small piece from the top of the compact that was not deconsolidated that may have held 20–50 particles based on its apparent size, 31 individual particles with significant matrix remaining on the surface of the OPyC that were counted separately, and 5 particles in multiparticle clumps that could not be counted individually. The clean TRISO particles and the matrix-coated particles were surveyed with IMGA, while the small piece that was not deconsolidated and the two multiparticle clumps were set aside for particle burn-leach analysis. A total of 3,098 individual particles were successfully surveyed out of the 3,120 single particles loaded into the IMGA hopper. Throughout the IMGA survey, there were numerous intermittent failures of the particle handler translation stages that resulted in some particles being dropped where they could not be recovered, and one instance in which the vacuum needle was driven down into the particle source container and broken off. That container was kept separate so that any broken particles in the container would not be included in the particle burn-leach analysis. However, the suspect particles were still run through the IMGA to complete the survey. The AGR-2 Compact 2-1-2 IMGA survey included 97.5% of the particles in the compact, assuming the compact started with the average number of particles in an AGR-2 UCO compact, which was 3,176.

Figure 5-1 is a histogram of the measured ^{137}Cs activity in each particle divided by its particle-specific calculated activity, which was based on an adjustment to the average calculated activity using the normalized ^{144}Ce activity to account for variation in initial fissile inventory and burnup, as described in Section 2.2. The bin locations for the two special particles (SPs) identified during the IMGA survey are labeled in Figure 5-1. Particle 212-SP02 was automatically set aside by the IMGA because its ^{137}Cs/^{144}Ce ratio was on the margin of the main distribution. However, the histogram in Figure 5-2 of the normalized ^{137}Cs activities shows that the measured ^{137}Cs activity for Particle 212-SP02 was close to the average measured value, while the histogram in Figure 5-3 of the normalized ^{144}Ce activities shows that the measured ^{144}Ce activity for Particle 212-SP02 was abnormally high.

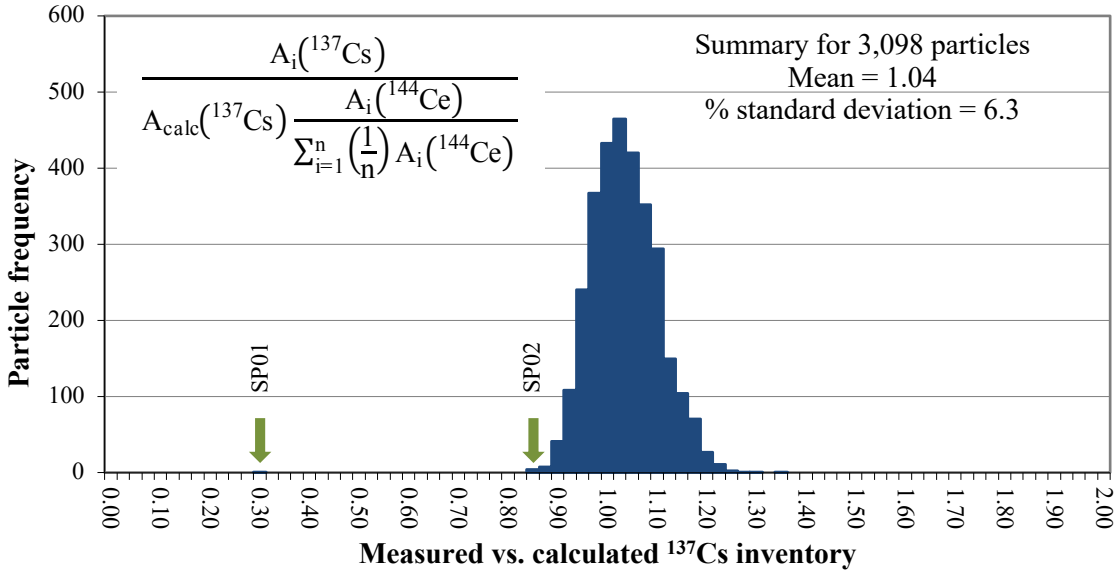

Figure 5-1. Ratio of ^{137}Cs retained in 3,098 Compact 2-1-2 particles after safety testing to 1,800°C vs. the calculated inventory adjusted for variation in fissionable material and burnup with the measured ^{144}Ce activity.

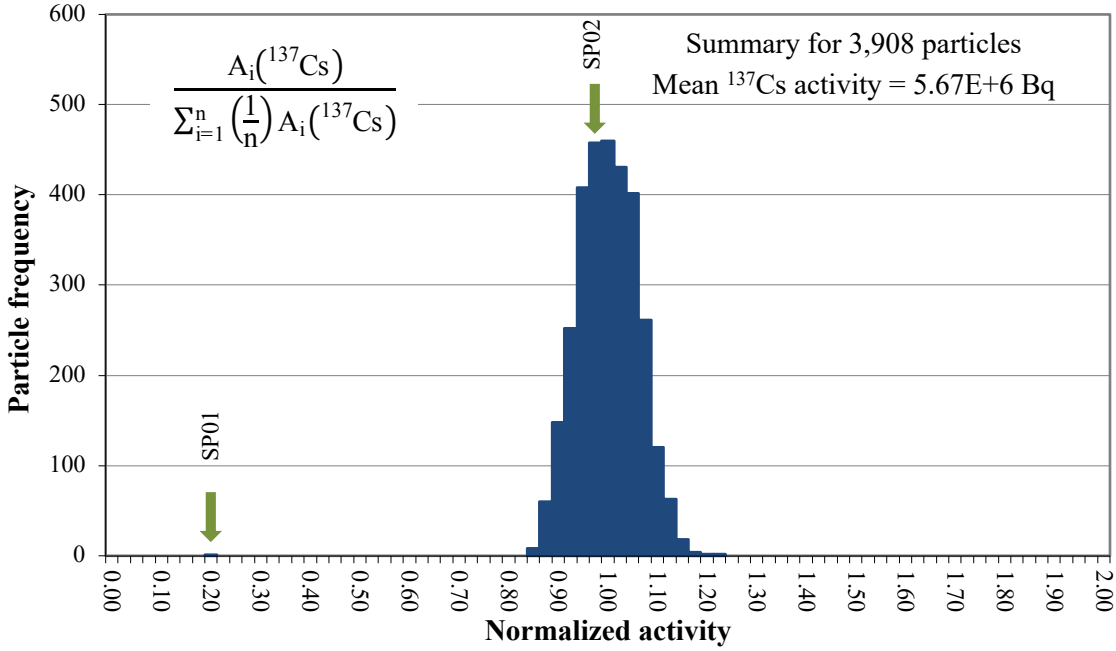

Figure 5-2. Particle distribution for measured ^{137}Cs activity normalized to the average.

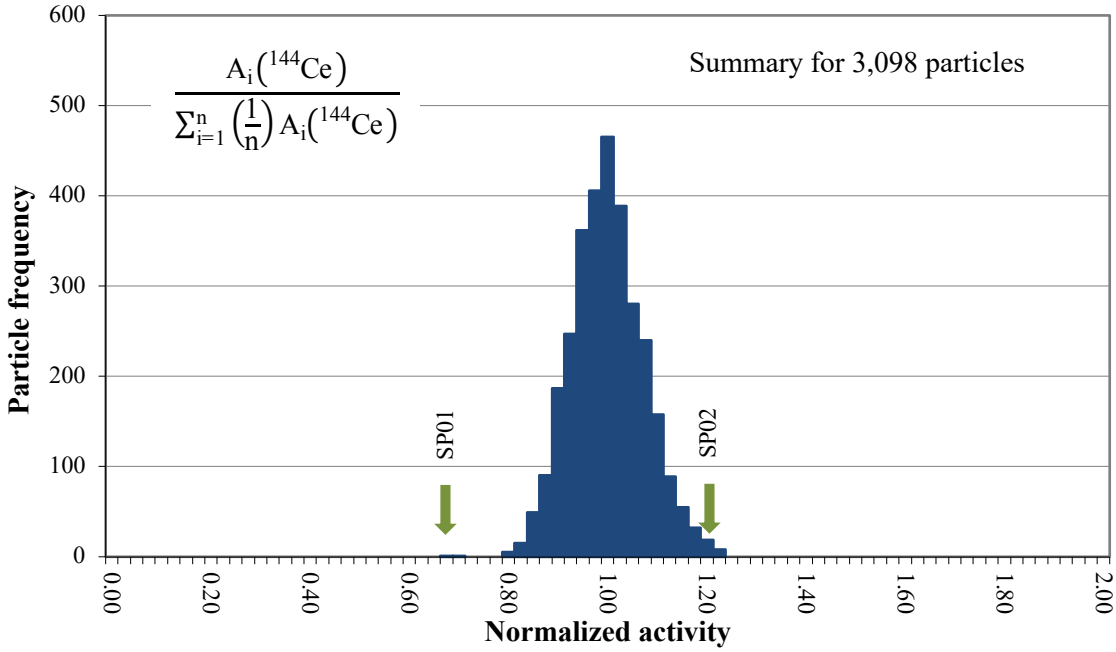

Figure 5-3. Particle distribution for measured ^{144}Ce activity normalized to the average.

It is likely that the marginal ^{137}Cs/^{144}Ce ratio for Particle 212-SP02 was from a larger-than-normal error in the ^{144}Ce measurement rather than preferential release of cesium. The IMGA survey was performed using a live time of 180 s, which did not always provide a well-defined ^{144}Ce peak in the gamma spectra during the survey of Particle 212-SP02, because the gamma emission rate was low after ~5.7 ^{144}Ce half-lives had passed. The ^{106}Ru isotope has a half-life of 372 days, which is longer than that of ^{144}Ce at 285 days, and the 511.9 keV ^{106}Ru peak has a lower background continuum compared to 133.5 keV for ^{144}Ce. Therefore, ^{106}Ru can sometimes provide more accurate measurement of the variation in fissionable material and burnup. Both ^{144}Ce and ^{106}Ru have historically been used for comparison to ^{137}Cs during IMGA survey at ORNL because they are retained well, even when defective or failed SiC causes significant cesium release. Figure 5-4 is a histogram of the normalized ^{106}Ru activities, with the relative locations of the

activities for Particle 212-SP01 and Particle 212-SP02 labeled. Particle 212-SP02 is closer to the center of the distribution in Figure 5-4 compared to its location in Figure 5-3. This supports a conclusion that the measured ^{144}Ce activity may have included a significant positive error. The position of Particle 212-SP01 relative to the main distribution is also significantly different in Figure 5-4 than in Figure 5-3. However, this difference is due to cerium release from Particle 212-SP01. Figure 5-5 shows the distribution in ^{137}Cs M/C calculated using the normalized ^{106}Ru rather than using the normalized ^{144}Ce as was done for Figure 5-1. Using ^{106}Ru rather than ^{144}Ce resulted in a lower standard deviation and shifted the value for Particle 212-SP02 to be within the main distribution.

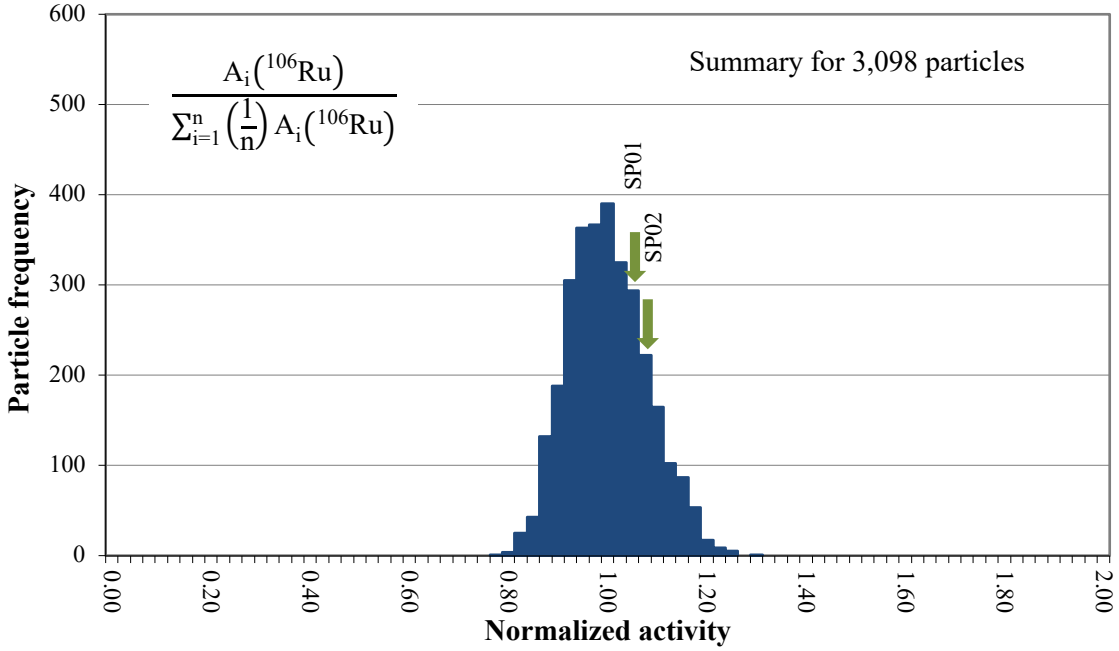

Figure 5-4. Particle distribution for measured ^{106}Ru activity normalized to the average.

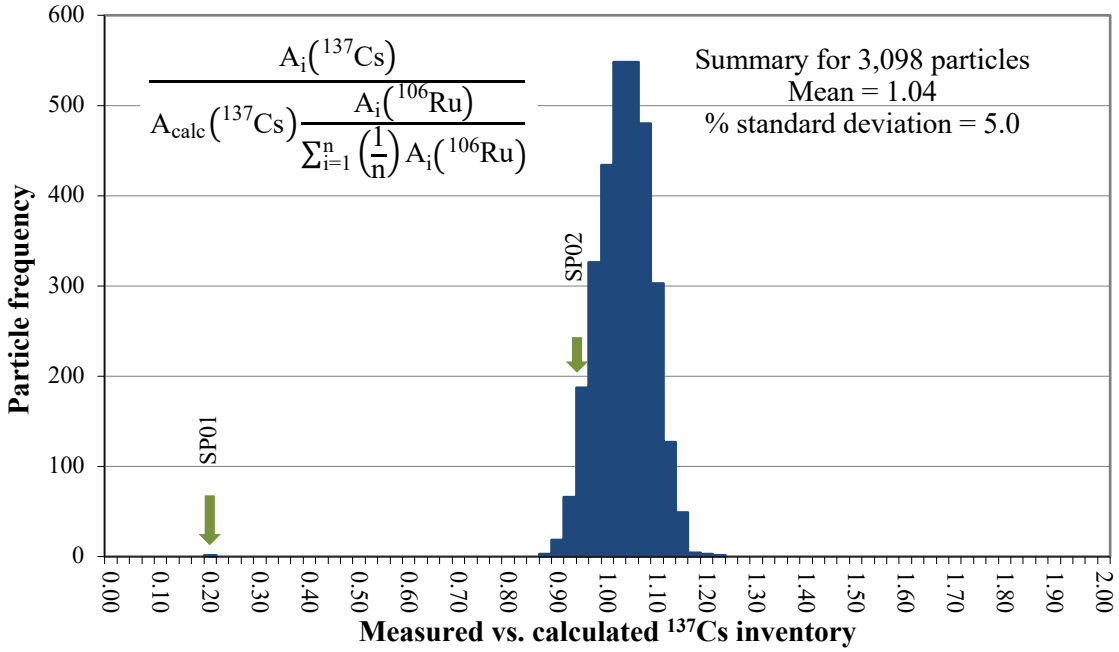

Figure 5-5. Ratio of ^{137}Cs retained in 3,098 Compact 2-1-2 particles after safety testing to 1,800°C vs. the calculated inventory adjusted for variation in fissionable material and burnup with the measured ^{106}Ru activity.

5.2 SIX-HOUR GAMMA COUNTING

Particle 212-SP01 and Particle 212-SP02 were subjected to gamma counting using a live time of 6 h. The gamma counting was performed with the IMGA working in vial-handling mode so that individual particle identity could be retained. Table 5-1 shows the measured activities for these two special particles that were sorted out by the IMGA. Particle 212-SP01 had a retained ^{134}Cs activity that was 18% of the average calculated ^{134}Cs inventory in one particle, which was 6.09E+6 Bq one day after EOL. The amount of residual ^{134}Cs in Particle 212-SP01 is consistent with the conclusion that this one particle was responsible for the majority of cesium released during safety testing, which was 74% of the average ^{134}Cs inventory in one particle (Table 3-1). Particle 212-SP01 was examined with x-ray computed tomography (XCT) and cross sectioned for materialographic inspection to confirm that it was a particle with failed SiC (Section 7.4 and Section 7.5). Particle 212-SP02, which was within the normal range for retained cesium inventory (Figure 5-5), was also examined by XCT and confirmed to be a non-failed particle (Section 6).

Table 5-1. Activity in special particles

Particle	^{106}Ru	^{110m}Ag [a]	^{125}Sb	^{134}Cs	^{137}Cs	^{144}Ce	^{154}Eu
212-SP01	1.74E+7	<1.34E+4	2.86E+5	1.11E+6	1.11E+6	3.34E+7	2.07E+4
212-SP02	1.84E+7	<2.24E+4	2.88E+5	5.80E+6	5.68E+6	5.86E+7	1.83E+5

Note: Activities are reported in Bq, decay-corrected to one day after EOL.
[a] Less-than values indicate that the ^{110m}Ag activity was below the detection limit.

Gamma counting in vial-handling mode using a live time of 6 h was also performed on 46 randomly selected (RS) particles. Table 5-2 shows the IMGA data for the 46 RS-series particles. The ^{110m}Ag had a relatively high minimum detection limit (MDL) of <33–42% because there was only ~1% of the end-of-irradiation activity remaining after 6.7–6.8 half-lives. Figure 5-6 shows the histogram for the measured ^{110m}Ag in these particles. The distribution of ^{110m}Ag retention varied from essentially full retention in two particles to retention below the MDL. Eight out of the 46 particles had measurable ^{110m}Ag activities. Variability in silver retention is conjectured to be a result of the individual thermal history of each particle, which can vary several hundred degrees across the compact (Hawkes 2014).

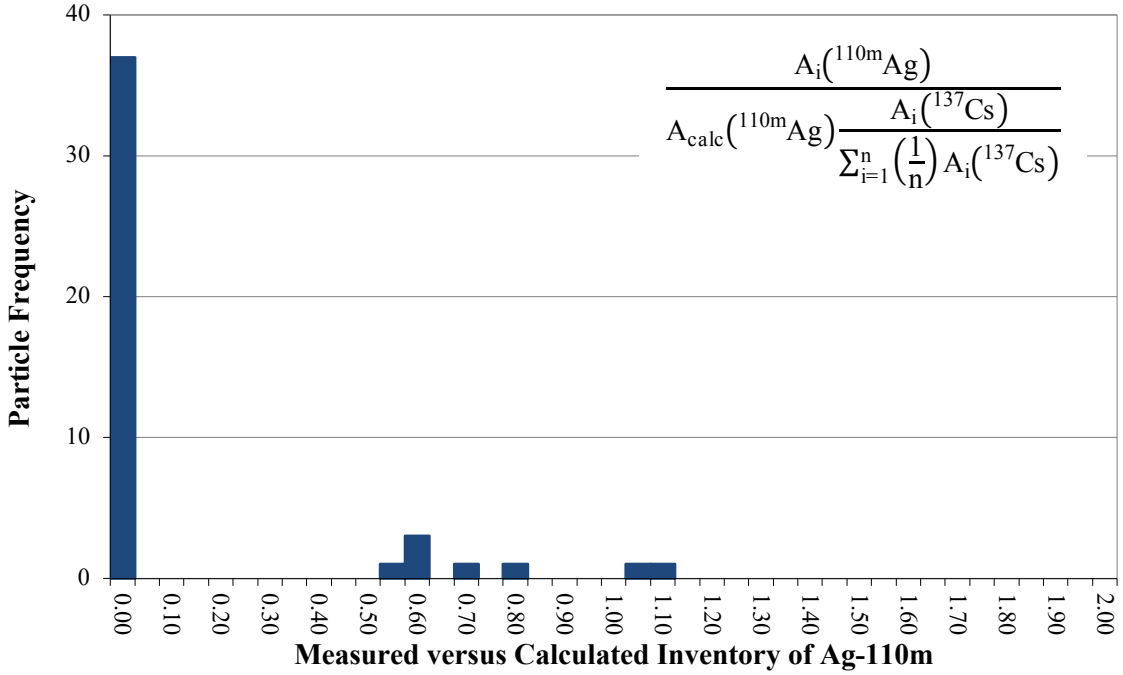

Figure 5-6. Ratio of ^{110m}Ag retained in 46 randomly selected Compact 2-1-2 particles after safety testing to 1,800°C vs. the calculated inventory adjusted for variation in fissionable material and burnup with the measured ^{137}Cs activity (particles plotted as "zero" were below a detection limit of ^{110m}Ag M/C <33–42%).

Table 5-2. Activity in 46 randomly selected particles

Particle	^{106}Ru	^{110m}Ag [a]	^{125}Sb	^{134}Cs	^{137}Cs	^{144}Ce	^{154}Eu
212-RS01	2.01E+7	7.90E+4	3.11E+5	7.24E+6	6.34E+6	5.32E+7	2.26E+5
212-RS02	1.79E+7	3.60E+4	2.97E+5	6.62E+6	6.03E+6	5.31E+7	2.30E+5
212-RS03	1.80E+7	7.23E+4	2.93E+5	7.02E+6	6.17E+6	4.87E+7	2.22E+5
212-RS04	1.61E+7	3.47E+4	2.59E+5	5.73E+6	5.20E+6	4.63E+7	1.86E+5
212-RS05	1.66E+7	4.25E+4	2.69E+5	6.31E+6	5.59E+6	4.68E+7	2.01E+5
212-RS06	1.56E+7	<2.24E+4	2.64E+5	5.84E+6	5.52E+6	5.00E+7	1.84E+5
212-RS07	1.65E+7	<2.32E+4	2.79E+5	6.03E+6	5.76E+6	5.08E+7	1.98E+5
212-RS08	1.75E+7	<2.31E+4	2.94E+5	6.17E+6	5.89E+6	5.41E+7	1.79E+5
212-RS09	1.55E+7	<2.20E+4	2.60E+5	5.69E+6	5.48E+6	4.90E+7	1.54E+5
212-RS10	1.63E+7	<2.26E+4	2.61E+5	5.49E+6	5.32E+6	5.15E+7	1.73E+5
212-RS11	1.63E+7	<2.40E+4	2.76E+5	6.08E+6	5.76E+6	5.00E+7	1.98E+5
212-RS12	1.76E+7	<2.28E+4	2.95E+5	6.38E+6	6.00E+6	5.14E+7	2.02E+5
212-RS13	1.77E+7	<2.34E+4	2.94E+5	6.21E+6	5.95E+6	5.74E+7	1.72E+5
212-RS14	1.75E+7	<2.50E+4	2.94E+5	6.42E+6	5.99E+6	5.50E+7	2.01E+5
212-RS15	1.64E+7	<2.14E+4	2.69E+5	5.44E+6	5.32E+6	5.30E+7	1.74E+5
212-RS16	1.61E+7	3.63E+4	2.69E+5	5.98E+6	5.48E+6	4.78E+7	1.96E+5
212-RS17	1.66E+7	<2.23E+4	2.68E+5	5.59E+6	5.48E+6	5.13E+7	1.76E+5
212-RS18	1.75E+7	<2.23E+4	2.86E+5	6.03E+6	5.83E+6	5.62E+7	1.94E+5
212-RS19	1.79E+7	5.18E+4	2.87E+5	6.66E+6	5.80E+6	4.51E+7	2.10E+5
212-RS20	1.46E+7	<2.15E+4	2.36E+5	5.38E+6	4.98E+6	4.38E+7	1.81E+5
212-RS21	1.89E+7	4.05E+4	3.05E+5	7.08E+6	6.15E+6	4.80E+7	2.27E+5
212-RS22	1.82E+7	<2.26E+4	2.97E+5	6.37E+6	6.04E+6	5.51E+7	1.80E+5
212-RS23	1.72E+7	<2.38E+4	2.82E+5	5.97E+6	5.67E+6	5.45E+7	1.72E+5
212-RS24	1.67E+7	<2.28E+4	2.92E+5	6.11E+6	5.83E+6	5.48E+7	1.78E+5
212-RS25	1.69E+7	<2.30E+4	2.99E+5	6.43E+6	6.02E+6	5.53E+7	1.99E+5
212-RS26	1.66E+7	<2.14E+4	2.71E+5	5.47E+6	5.32E+6	5.33E+7	1.75E+5
212-RS27	1.62E+7	<2.28E+4	2.79E+5	6.02E+6	5.66E+6	5.13E+7	1.85E+5
212-RS28	1.62E+7	<2.19E+4	2.69E+5	5.77E+6	5.42E+6	4.80E+7	1.94E+5
212-RS29	1.66E+7	<2.29E+4	2.93E+5	6.42E+6	6.04E+6	5.43E+7	1.89E+5
212-RS30	1.62E+7	<2.21E+4	2.77E+5	5.91E+6	5.63E+6	5.27E+7	1.73E+5
212-RS31	1.61E+7	<2.33E+4	2.80E+5	6.20E+6	5.75E+6	5.15E+7	1.93E+5
212-RS32	1.56E+7	<2.24E+4	2.69E+5	5.88E+6	5.55E+6	4.90E+7	1.46E+5
212-RS33	1.43E+7	<2.23E+4	2.54E+5	5.46E+6	5.17E+6	4.65E+7	1.69E+5
212-RS34	1.83E+7	<2.41E+4	3.00E+5	6.26E+6	6.02E+6	5.78E+7	1.92E+5
212-RS35	1.71E+7	<2.30E+4	2.91E+5	5.94E+6	5.67E+6	5.44E+7	1.78E+5
212-RS36	1.88E+7	<2.36E+4	3.05E+5	6.21E+6	6.00E+6	5.92E+7	1.96E+5
212-RS37	1.76E+7	<2.30E+4	2.89E+5	5.79E+6	5.65E+6	5.43E+7	1.78E+5
212-RS38	1.67E+7	<2.18E+4	2.77E+5	5.60E+6	5.53E+6	5.37E+7	1.69E+5
212-RS39	1.69E+7	<2.30E+4	2.90E+5	6.31E+6	5.98E+6	5.36E+7	1.95E+5
212-RS40	1.70E+7	<2.36E+4	2.89E+5	6.32E+6	5.98E+6	5.21E+7	1.53E+5
212-RS41	1.66E+7	<2.36E+4	2.80E+5	6.00E+6	5.68E+6	5.33E+7	1.82E+5
212-RS42	1.73E+7	<2.22E+4	2.84E+5	6.12E+6	5.66E+6	4.98E+7	1.96E+5
212-RS43	1.63E+7	<2.48E+4	2.70E+5	5.86E+6	5.57E+6	5.20E+7	1.76E+5
212-RS44	1.58E+7	<2.52E+4	2.67E+5	5.73E+6	5.39E+6	4.81E+7	1.59E+5
212-RS45	1.81E+7	<2.72E+4	3.04E+5	6.48E+6	6.16E+6	5.65E+7	1.87E+5
212-RS46	1.83E+7	<2.49E+4	3.03E+5	6.27E+6	5.97E+6	5.69E+7	2.00E+5
Maximum	2.01E+7	7.90E+4	3.11E+5	7.24E+6	6.34E+6	5.92E+7	2.30E+5
Minimum	1.43E+7	<2.14E+4	2.36E+5	5.38E+6	4.98E+6	4.38E+7	1.46E+5
Mean	1.69E+7	0.85–2.76E+4	2.82E+5	6.09E+6	5.73E+6	5.20E+7	1.87E+5
Std. Dev.	6.6%	234–44%	5.7%	7.0%	5.3%	6.8%	9.9%

Note: Values are reported in Bq decay-corrected to one day after EOL.

[a] Less-than values indicate that the ^{110m}Ag activity was below the MDL. Summary values for ^{110m}Ag are presented as a range in which particles below the MDL were treated as ranging from a minimum value of zero to a maximum value of their individual MDLs.

Table 5-3 shows how the measured activities in the randomly selected particles compare to the calculated values. The mean and standard deviations for the measured ^{110m}Ag activity are reported as ranges in which particles below the MDL were treated as ranging from a minimum value of zero to a maximum value of the MDL. This range roughly indicates the overall silver retention, but the uncertainty is high due to the high MDL. Europium release was indicated in the safety test data at levels above 1%. However, because of a known offset error in the calculated values, the significant bias between the measured and calculated activities for ^{125}Sb and ^{154}Eu cannot be used to determine how much of these isotopes may have been released during irradiation and safety testing. The observed biases for ^{125}Sb and ^{154}Eu were similar to the biases observed between calculated averages and gamma scanning measurements of the AGR-1 compacts with the Idaho National Laboratory (INL) Precision Gamma Scanner (PGS) (Harp et al. 2014). Europium release from AGR-1 compacts during irradiation was well below 0.1% (Demkowicz et al. 2013), so the difference between the ^{154}Eu activity measured by the PGS and the calculated activity can be assumed to be an error in the calculated value. A similar argument holds for ^{125}Sb.

Table 5-3. Summary of results from 6-hour IMGA analysis of Compact 2-1-2 particles

Isotope	Calculated activity [a] (Bq/particle)	Measured activity [b] (Bq/particle)		Ratio of measured vs. calculated activity [c]		Measured-to-calculated ratio in AGR-1 compact activity [d]	
		mean	std. dev.	mean	std. dev.	mean	std. dev.
^{106}Ru	1.51E+7	1.69E+7	6.6%	1.12	0.07	0.96	0.04
^{110m}Ag [e]	6.40E+4	0.85–2.76E+4	234–44%	0.13–0.43	0.31–0.19	not in reference	
^{125}Sb	3.82E+5	2.82E+5	5.7%	0.74	0.04	0.70	0.04
^{134}Cs	6.24E+6	6.09E+6	7.0%	0.98	0.07	0.97	0.05
^{137}Cs	5.49E+6	5.73E+6	5.3%	1.04	0.06	0.99	0.03
^{144}Ce	4.81E+7	5.20E+7	6.8%	1.08	0.07	1.00	0.04
^{154}Eu	2.27E+5	1.87E+5	9.9%	0.82	0.08	0.83	0.04

[a] Calculated activity for one day after EOL.
[b] Measured activity decay-corrected to one day after EOL.
[c] Not the same as M/C, which is also adjusted for variation in fissionable material and burnup.
[d] Summary results from gamma scanning of whole AGR-1 compacts (Demkowicz et al. 2015, Table 14).
[e] Values for ^{110m}Ag are presented as a range in which particles below the detection limit were treated as ranging from a minimum value of zero to a maximum value of the detection limit.

6. X-RAY COMPUTED TOMOGRAPHY

Table 6-1 lists the three particles selected for XCT. One representative particle was selected from the randomly selected particles listed in Table 5-2. The other two were the special particles identified using the IMGA (Section 5.1). Particle inventory in Table 6-1 is presented in terms of M/C and M/A as described in Section 2.2. The M/A ratio removed possible biases introduced by error in the calculated inventory, making it easier to survey the results with respect to the average. The values in Table 6-1 were adjusted for particle-to-particle variation in initial fissile inventory and burnup using the normalized ^{106}Ru values. The adjustment was based on ^{106}Ru instead of ^{144}Ce because Particle 212-SP01 released a significant fraction of its cerium, while ruthenium appeared to be well retained (Table 5-1). Therefore, ^{144}Ce was a poor indicator for initial fissile inventory and burnup in Particle 212-SP01. For consistency, values for the other particles in the table were also calculated using the normalized ^{106}Ru. Table 6-1 shows that Particle 212-SP01 had below average values for ^{134}Cs, ^{137}Cs, ^{144}Ce, and ^{154}Eu, while ^{106}Ru and ^{125}Sb were retained well. Losses of cesium, cerium, and europium were related to the SiC failure in Particle 212-SP01, which is discussed further in Section 7.4 and Section 7.5.

Table 6-1. Particles selected for x-ray tomography

Measured vs. calculated inventory(M/C) [a]

Particle	^{106}Ru	^{110m}Ag [c]	^{125}Sb	^{134}Cs	^{137}Cs	^{144}Ce	^{154}Eu
212-SP01	1.12	<0.20	0.73	0.17	0.20	0.67	0.09
212-SP02	1.12	<0.32	0.69	0.86	0.95	1.12	0.74
212-RS14	1.12	<0.38	0.74	0.99	1.05	1.10	0.86

Measured vs. average inventory (M/A) [a]

Particle	^{106}Ru	^{110m}Ag [b, c]	^{125}Sb	^{134}Cs	^{137}Cs	^{144}Ce	^{154}Eu
212-SP01	1.00	<0.27	0.98	0.18	0.19	0.62	0.11
212-SP02	1.00	<0.42	0.94	0.88	0.91	1.04	0.90
212-RS14	1.00	<0.49	1.01	1.02	1.01	1.02	1.04

[a] M/C and M/A values were adjusted for fissile material and burnup using the normalized ^{106}Ru activity.
[b] Less-than values indicate that the ^{110m}Ag activities were below the MDL.
[c] M/A values for ^{110m}Ag were calculated using the average of the eight particles with measurable ^{110m}Ag.

Figure 6-1 shows two orthogonal tomograms through the center of Particle 212-SP02. This particle had a normal internal microstructure, and there were no indications for SiC failure. The outer three layers appeared to be intact, with some separation between the SiC and OPyC, as is often observed, especially after 1,800°C safety testing (Hunn et al. 2013c, Figure 27). The buffer in Particle 212-SP02 exhibited the typical detachment from the inner pyrolytic carbon (IPyC) layer, and there was no apparent radial fracture in the buffer. Figure 6-2 shows two orthogonal tomograms through the center of Particle 212-RS14. This particle had the same typical general layer microstructures as Particle 212-SP02 except for a higher-than-normal population of high-Z clusters in the buffer layer, which appear as white areas in the tomogram. X-ray images of Particle 212-SP01 are provided in Section 7.4, which provides discussion of the failed particle.

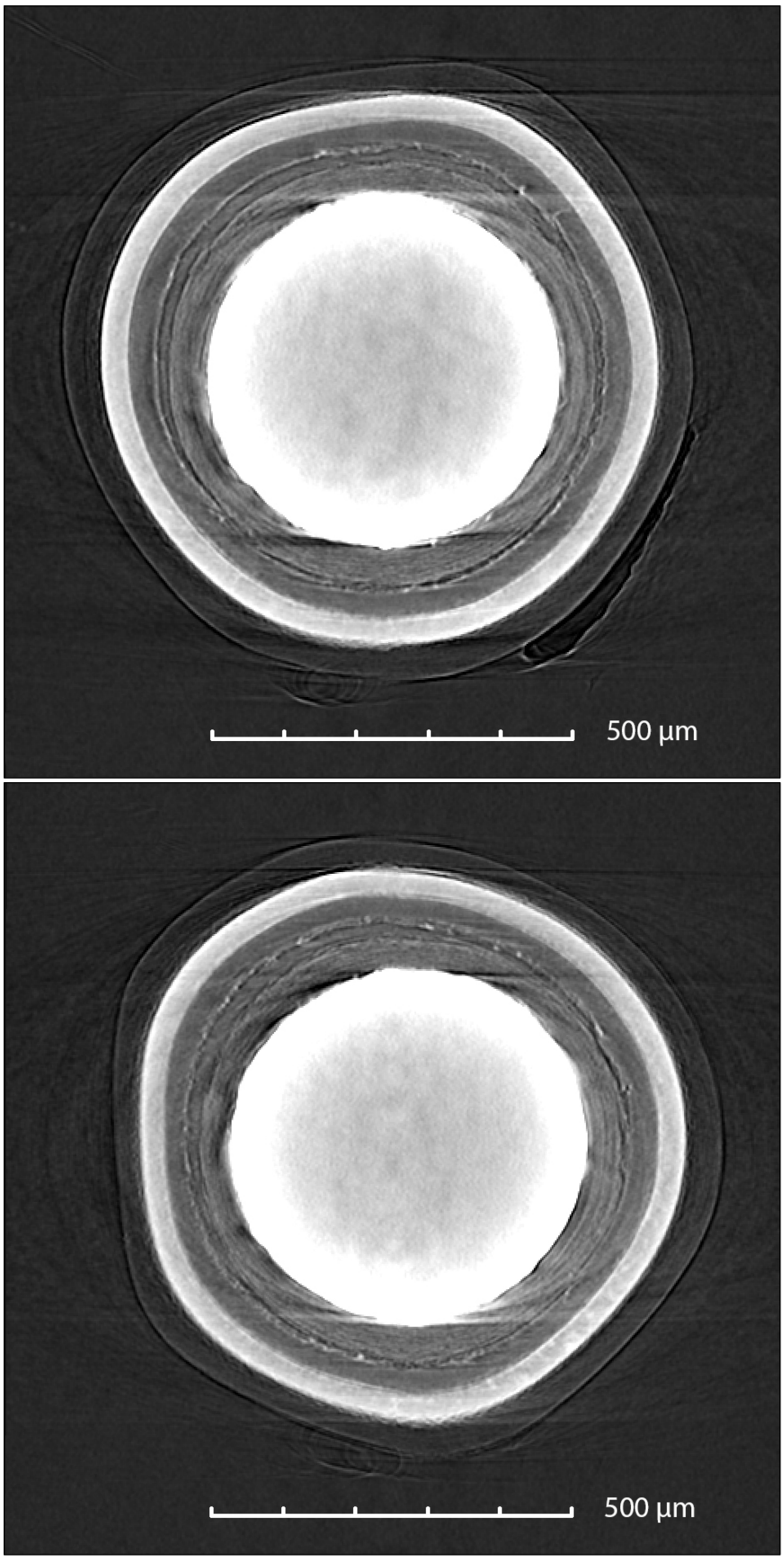

Figure 6-1. Orthogonal tomograms through the center of Particle 212-SP02.

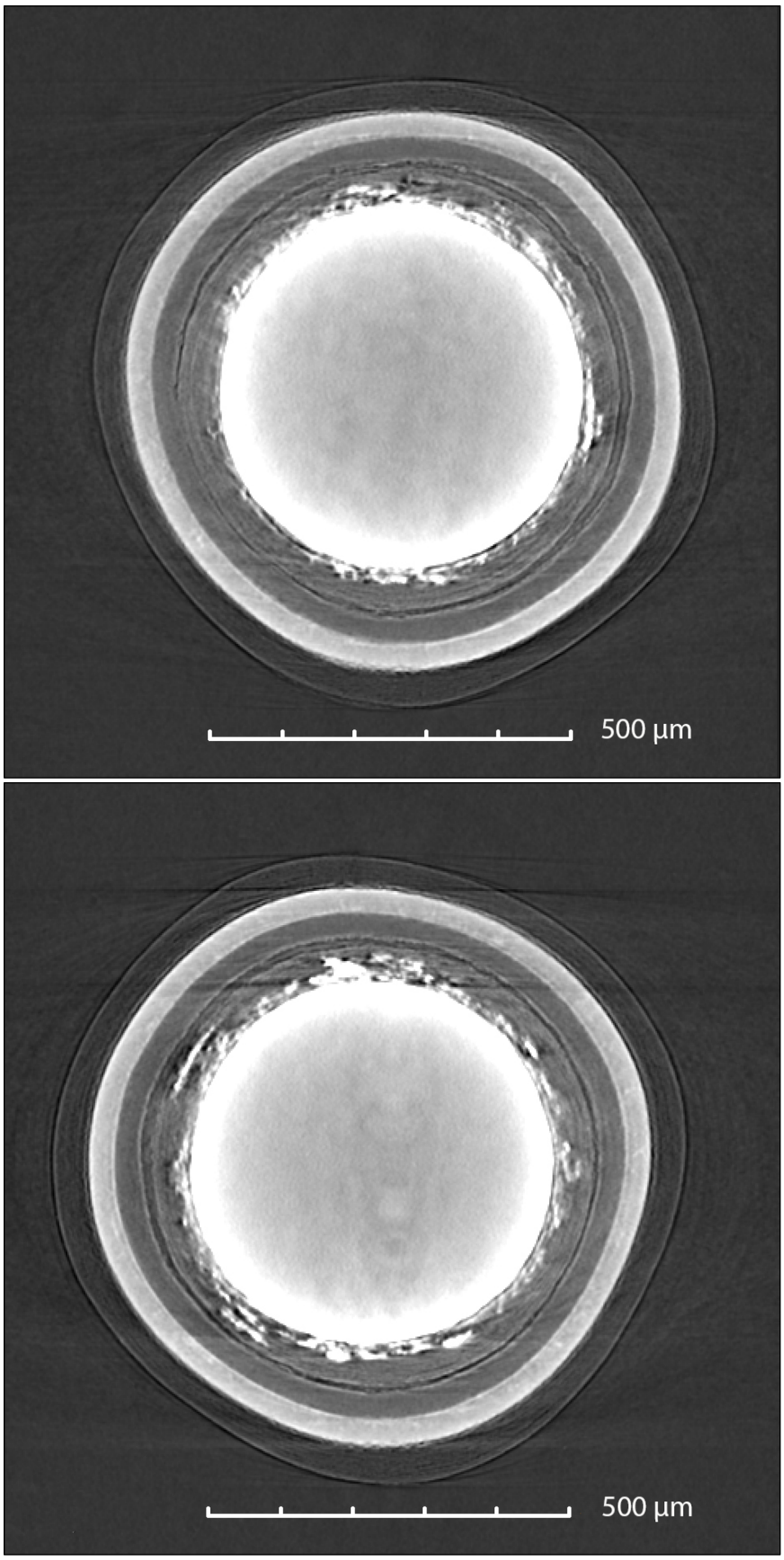

Figure 6-2. Orthogonal tomograms through the center of Particle 212-RS14.

7. MATERIALOGRAPHY

Table 7-1 lists the particles selected for materialographic examination. Particles were selected from the randomly selected particles listed in Table 5-2. Selection focused on particles with low-to-moderate silver release, with a secondary criterion of choosing particles with other isotope inventories close to average (M/A close to unity). Four particles were selected with ^{110m}Ag inventories below the MDL, and two particles were selected that released ^{110m}Ag but retained measurable ^{110m}Ag inventories.

Table 7-1. Particles selected for materialography

Measured vs. calculated inventory(M/C) [a]

Particle	^{106}Ru	^{110m}Ag [c]	^{125}Sb	^{134}Cs	^{137}Cs	^{144}Ce	^{154}Eu
212-RS08	1.12	<0.35	0.74	0.96	1.04	1.09	0.76
212-RS44	1.12	<0.42	0.75	0.99	1.05	1.07	0.75
212-RS43	1.12	<0.40	0.73	0.97	1.05	1.12	0.80
212-RS45	1.12	<0.40	0.75	0.97	1.05	1.10	0.77
212-RS05	1.12	0.68	0.72	1.03	1.04	0.99	0.90
212-RS16	1.12	0.60	0.74	1.01	1.05	1.05	0.91
212-SP01	1.12	<0.20	0.73	0.17	0.20	0.67	0.09

Measured vs. average inventory (M/A) [a]

Particle	^{106}Ru	^{110m}Ag [b, c]	^{125}Sb	^{134}Cs	^{137}Cs	^{144}Ce	^{154}Eu
212-RS08	1.00	<0.45	1.01	0.98	1.00	1.01	0.93
212-RS44	1.00	<0.55	1.02	1.01	1.01	0.99	0.92
212-RS43	1.00	<0.52	0.99	1.00	1.01	1.04	0.97
212-RS45	1.00	<0.52	1.01	1.00	1.01	1.02	0.94
212-RS05	1.00	0.88	0.97	1.06	1.00	0.92	1.10
212-RS16	1.00	0.78	1.01	1.03	1.01	0.97	1.10
212-SP01	1.00	<0.27	0.98	0.18	0.19	0.62	0.11

[a] M/C and M/A values were adjusted for fissile material and burnup using the normalized ^{106}Ru activity.
[b] Less-than values indicate that the ^{110m}Ag activities were below the MDL.
[c] M/A values for ^{110m}Ag were calculated using the average of the eight particles with measurable ^{110m}Ag.

7.1 OPTICAL IMAGING OF NORMAL PARTICLES

The particles listed in Table 7-1 were mounted and polished to near midplane and were imaged with an optical microscope using the methods and equipment developed for AGR-1 PIE (Hunn et al. 2013). Figure 7-1 through Figure 7-6 show the polished cross sections of the six particles from the RS particle set, which are representative of normal particle behavior for this compact. Optical micrographs of Particle 212-SP01 are provided in Section 7.4. The missing kernel material in the particles shown in Figure 7-3 and Figure 7-4 was caused by material falling out during the grinding and polishing process. The other particle cross sections show smaller regions of missing kernel material for the same reason. The buffer layer shrank and tore away from the buffer/IPyC interface in all particles that were examined. Particle RS45 had a region visible in the polish plane where the buffer was still attached to the IPyC (Figure 7-4). Other particles may have had similar regions that were not visible in the single-imaged plane. None of the buffer layers were fractured, which is a common observation for Capsule 2 compacts that appears to be related to the high irradiation temperature enhancing thermal creep (Hunn et al. 2016b). The gray material visible in the gap between the buffer and IPyC in all particles is epoxy that was injected into this region by vacuum infiltration after grinding had exposed the gap. Darker areas in the gap are voids where the epoxy is missing. The outer three TRISO layers all appeared intact, and no unusual features were observed in the optical images. Straight lines crossing these layers are scratches induced during sample preparation.

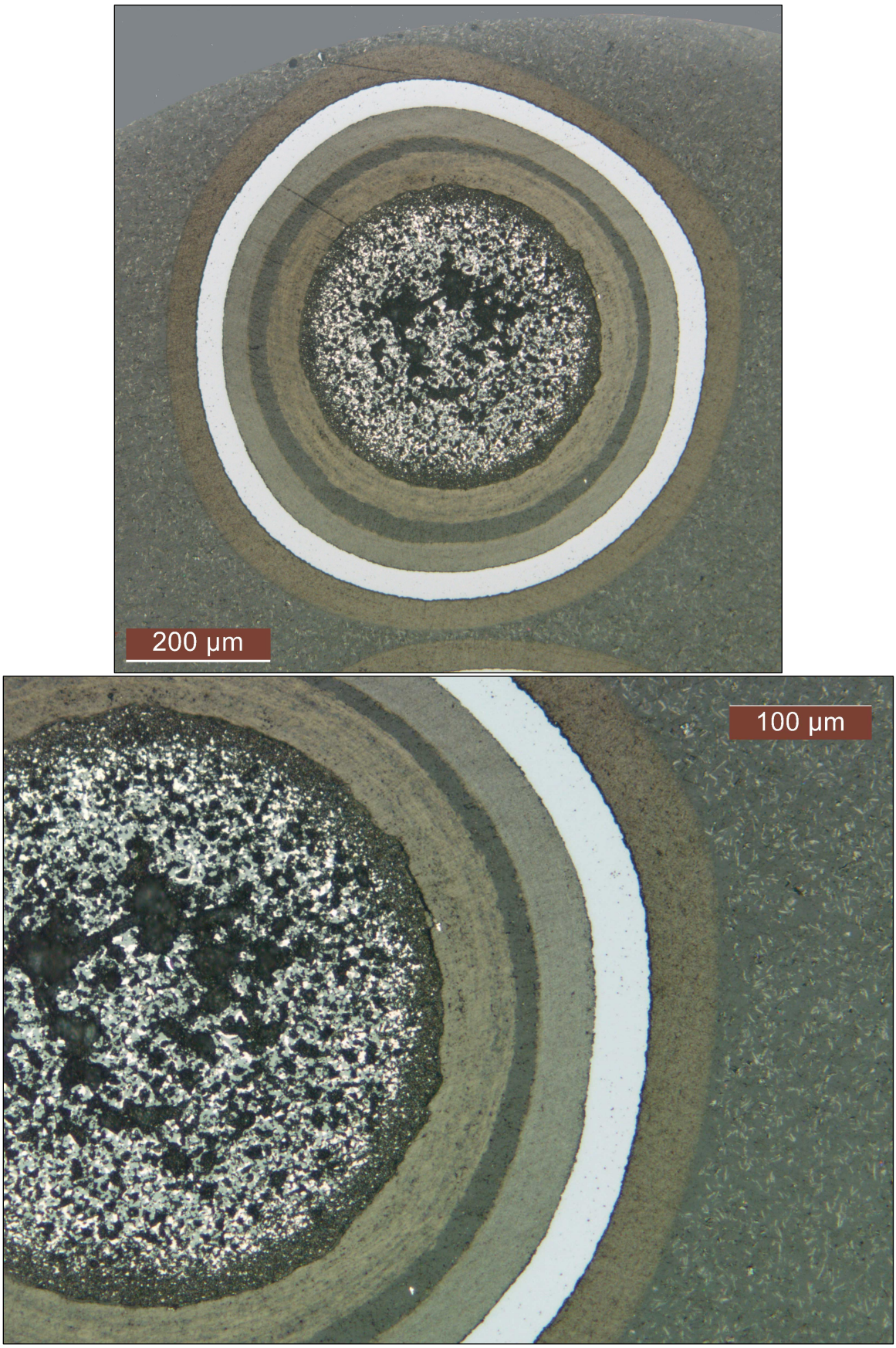

Figure 7-1. Optical micrographs of Particle 212-RS08 near midplane.

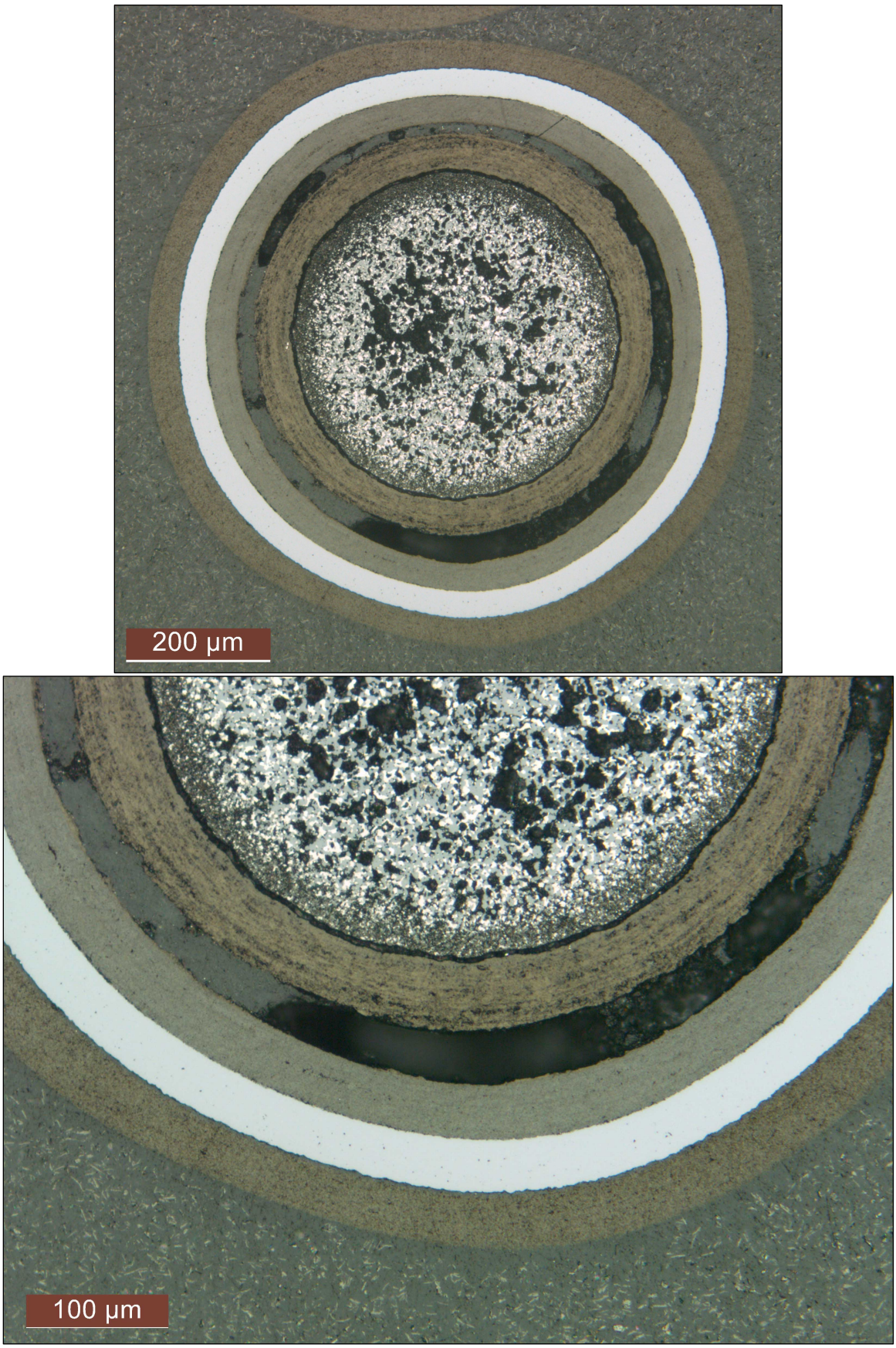

Figure 7-2. Optical micrographs of Particle 212-RS44 near midplane.

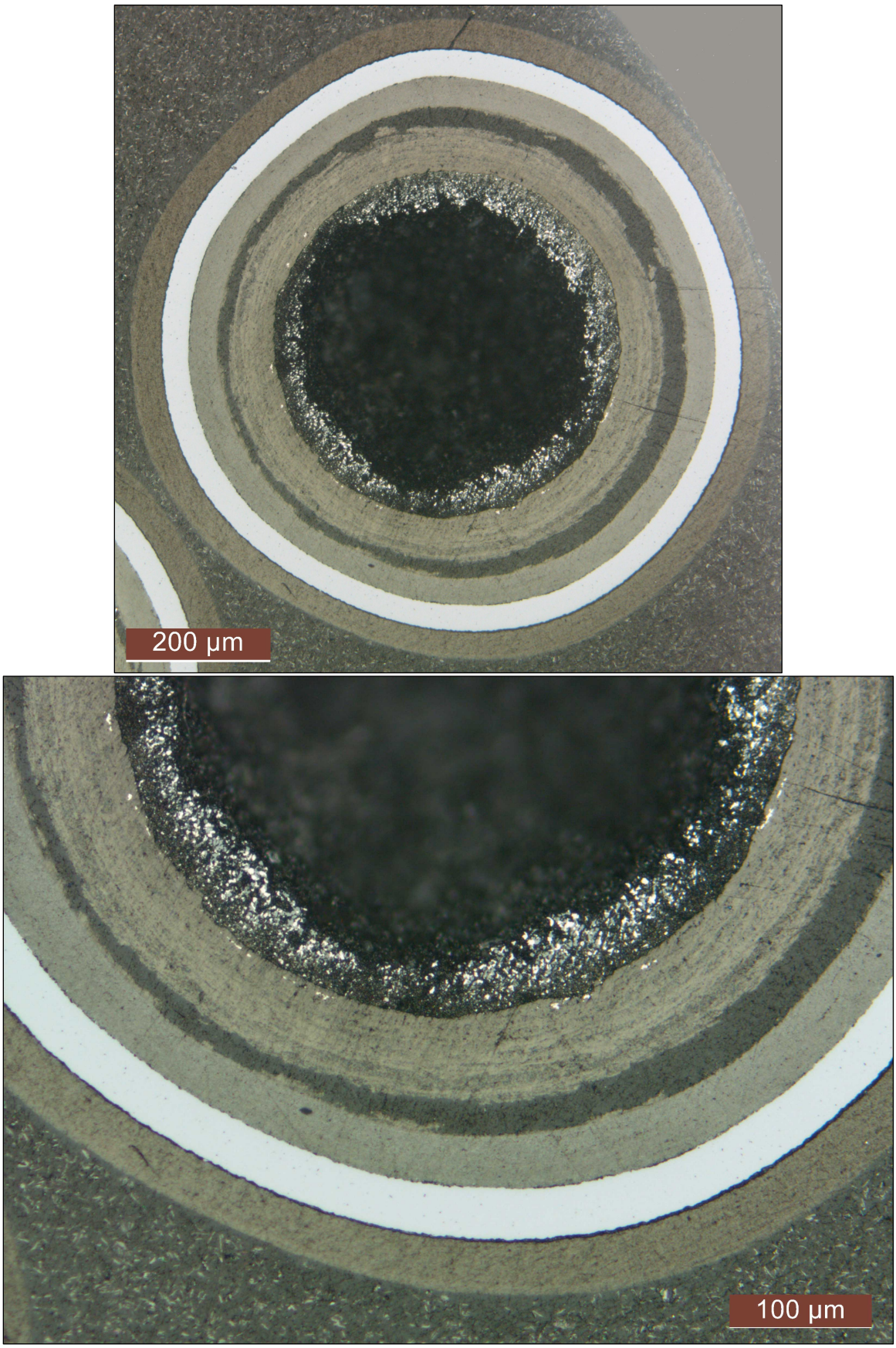

Figure 7-3. Optical micrographs of Particle 212-RS43 near midplane.

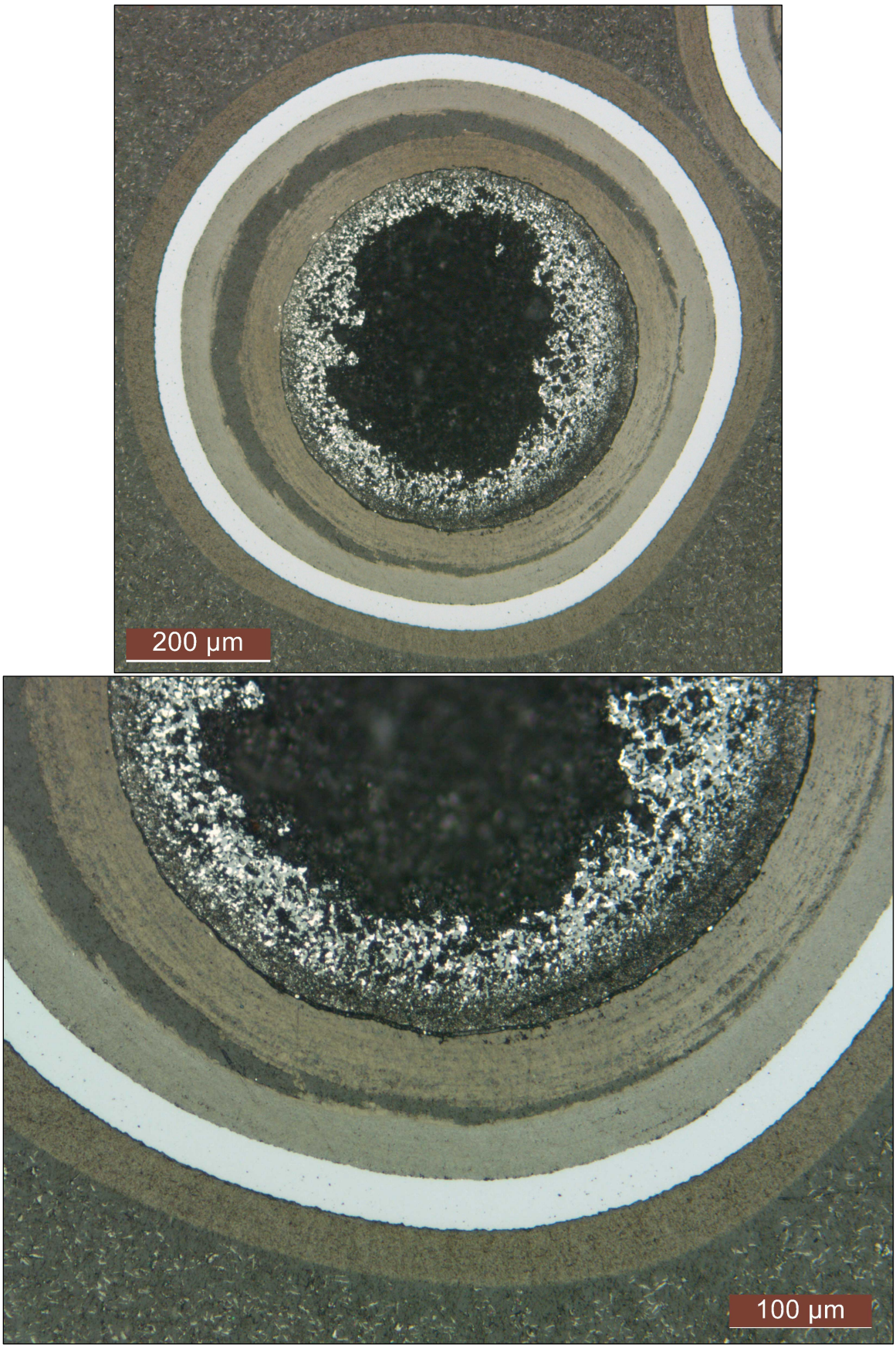

Figure 7-4. Optical micrographs of Particle 212-RS45 near midplane.

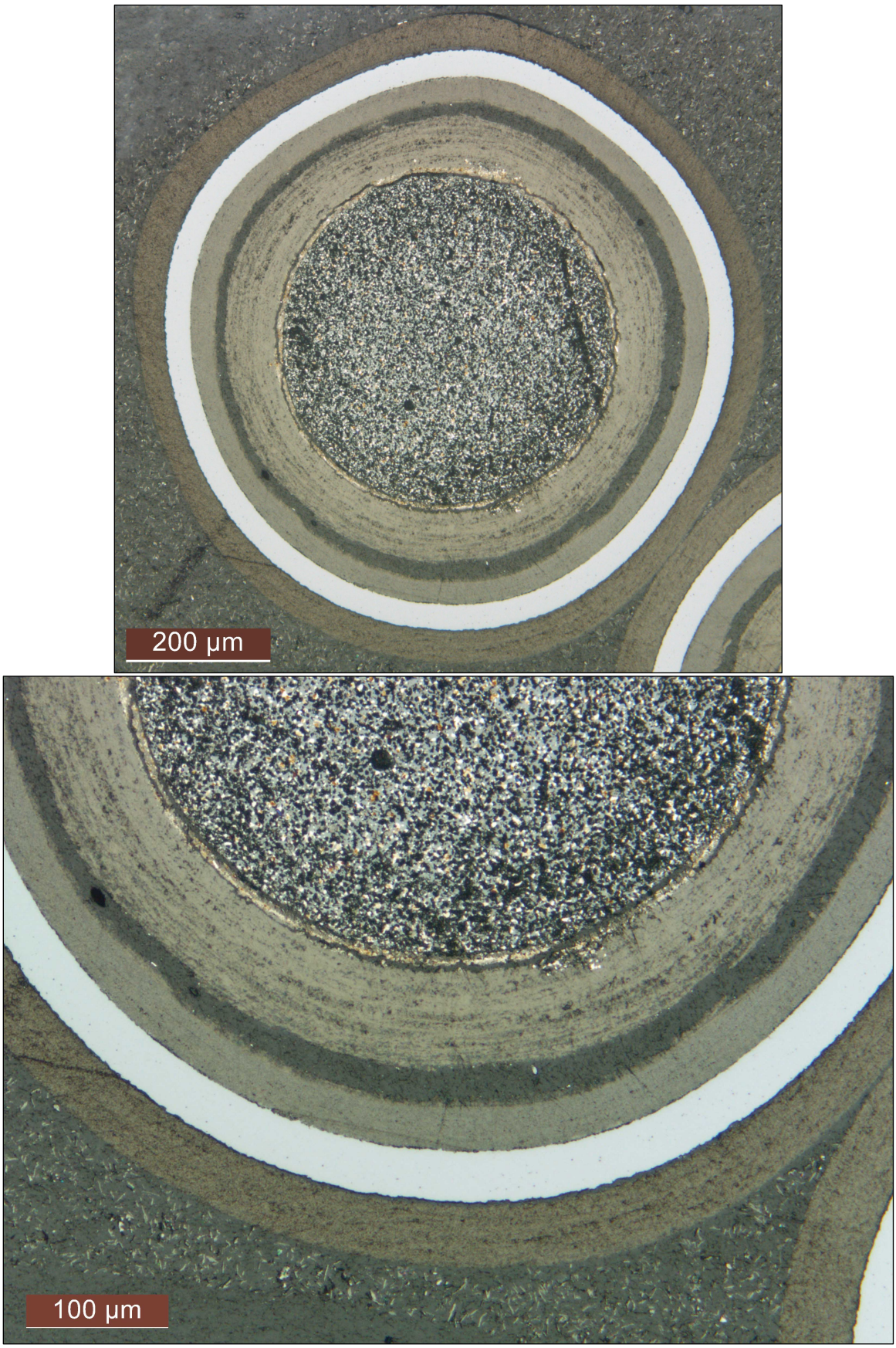

Figure 7-5. Optical micrographs of Particle 212-RS05 near midplane.

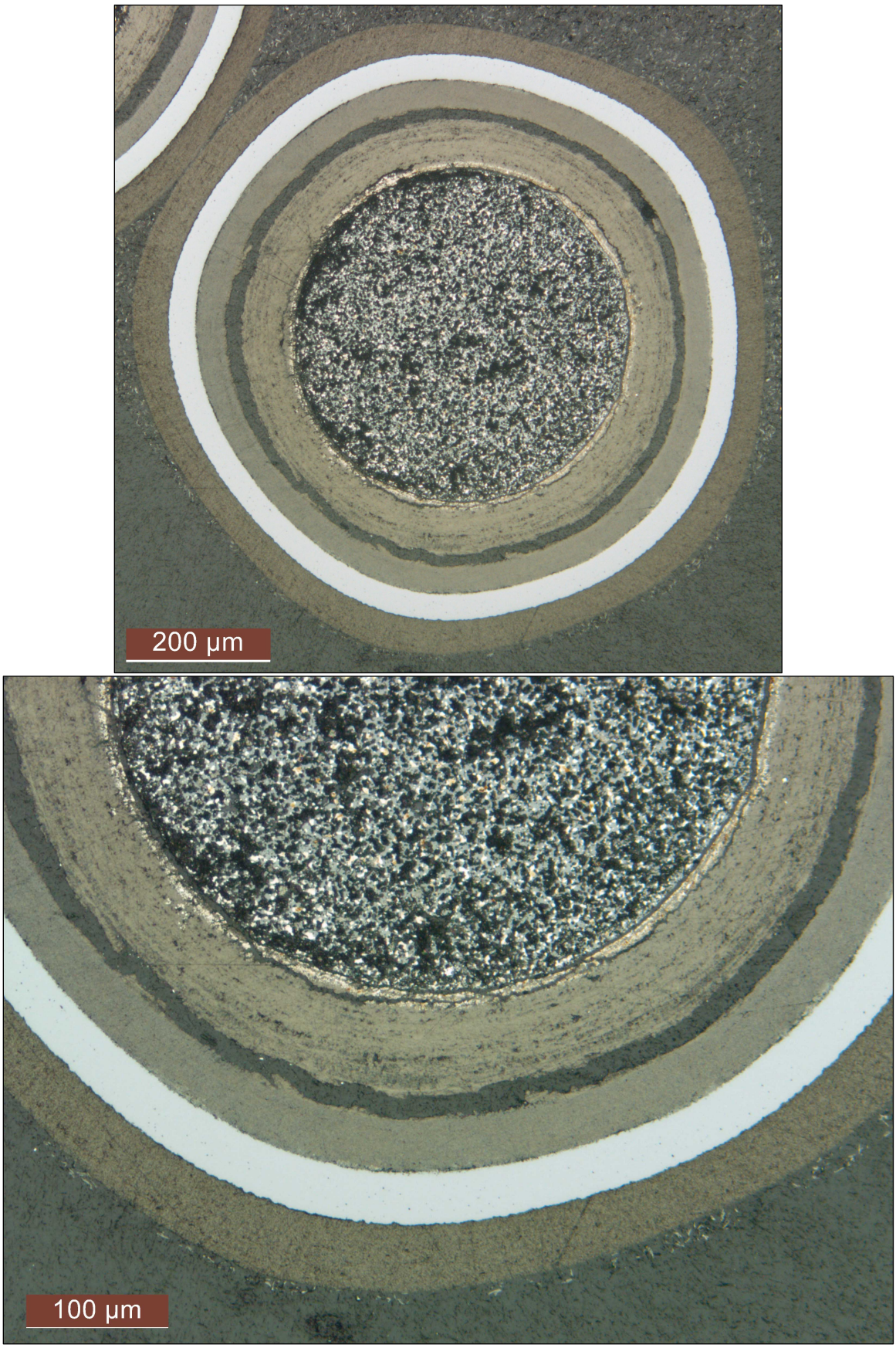

Figure 7-6. Optical micrographs of Particle 212-RS16 near midplane.

7.2 SEM IMAGING OF NORMAL PARTICLES

The polished cross sections of the normal particles from the RS particle set (listed in Table 7-1 and shown in the optical micrographs in Figure 7-1 through Figure 7-6) were examined with SEM and EDS as described in Section 2.3. Figure 7-7 through Figure 7-18 present a series of BEC micrographs that show selected areas of each particle cross section at two magnifications. Bright spots that appear within each coating layer usually indicate the presence of clustered high-Z material embedded in the lower-Z layers. Many of the high-Z features observed in the IPyC and SiC layers were common to all analyzed particles, but variation was observed in position and population of the features within each layer. To aid in the analysis of the observed high-Z features in the IPyC and SiC, the features were catalogued into four general classes based on the regions in which they were located. Features that appeared to be in contact with the boundary between the IPyC and SiC layers were catalogued as *high-Z boundary features* (Figure 7-10), where the IPyC/SiC boundary was defined by the stepwise change in image contrast delineating these two layers. Features in the SiC layer that were not in contact with the boundary were catalogued as *high-Z SiC features* (Figure 7-7). Features on the IPyC side of the IPyC/SiC boundary that were less than 10 µm from the boundary were catalogued as *high-Z interface features* (Figure 7-7), while features in the IPyC that were more than 10 µm from the boundary were catalogued as *high-Z IPyC features* (Figure 7-11). This segregation of features in the IPyC layer was applied to account for the fact that fission products and actinides observed in the IPyC near the IPyC/SiC boundary were different due to interaction with the SiC present in this region that had infiltrated into IPyC open porosity during coating deposition. *High-Z interface features* were often concentrated in a band several microns from the IPyC/SiC boundary, suggesting stabilization of the constituent species due to interaction with the SiC fingers in this region. *High-Z IPyC features* were typically much smaller than features in or near the SiC (Figure 7-12), with the exception of regions where the overall feature concentration was higher (Figure 7-14). These fine-scale h*igh-Z IPyC features* have been previously observed to be unique to both particles from the Capsule 2 compacts, which experienced higher irradiation temperatures, and particles from safety-tested compacts (Gerczak et al. 2018). The population of *high-Z IPyC features* was lowest in the particle with the highest ^{110m}Ag retention, Particle 212-RS05 (Figure 7-15 and Figure 7-16).

Significant variations in the number density of high-Z features located in different sectors around the circumference of the particles were observed in five of the six particles, with Particle 212-RS44 being the exception (Figure 7-9). Similar variations have been observed to sometimes be associated with locations in a particle where the buffer was not separated from the IPyC (Hunn et al. 2019, Section 7.2). Figure 7-1 through Figure 7-6 show that only Particle 212-RS45 had a visible sector where buffer/IPyC attachment was evident (Figure 7-4 and Figure 7-13). The high-Z features in Particle 212-RS45 were significantly more prominent in the sector where the buffer was attached to the IPyC, which is consistent with previous observations. The correlation between visible locations of buffer attachment and the local population of fission products and actinides suggests that transport of these species from the kernel could be impacted by the state of the buffer/IPyC interface. An extension of this hypothesis would logically include the possibility that the timing of local buffer/IPyC separation could also impact the observed distributions. No conclusions can be drawn regarding a correlation between the state of the buffer/IPyC interface and the high-Z feature distribution in the other four particles that had significant variation of feature density around the circumference of the imaged cross section. This is because there is insufficient information for these particles regarding the existence and location of a sector where the buffer may be attached to the IPyC or the timing of buffer detachment if no connection between the IPyC and buffer remains. Other mechanisms may also impact the distribution of fission products and actinides in the layers, such as thermal gradients in the particles, asymmetries at the kernel/buffer interface, or asymmetries in the coating microstructures.

A gap was observed between the SiC and OPyC layers around the entire circumference of the SiC/OPyC interface of all particles except Particle 212-RS16 (Figure 7-17). This gap has often been observed in irradiated AGR fuel particles and appears to widen during safety testing, especially at 1,800°C (Hunn et al. 2013c, Figure 27).

PARTICLE 212-RS08 OVERVIEW

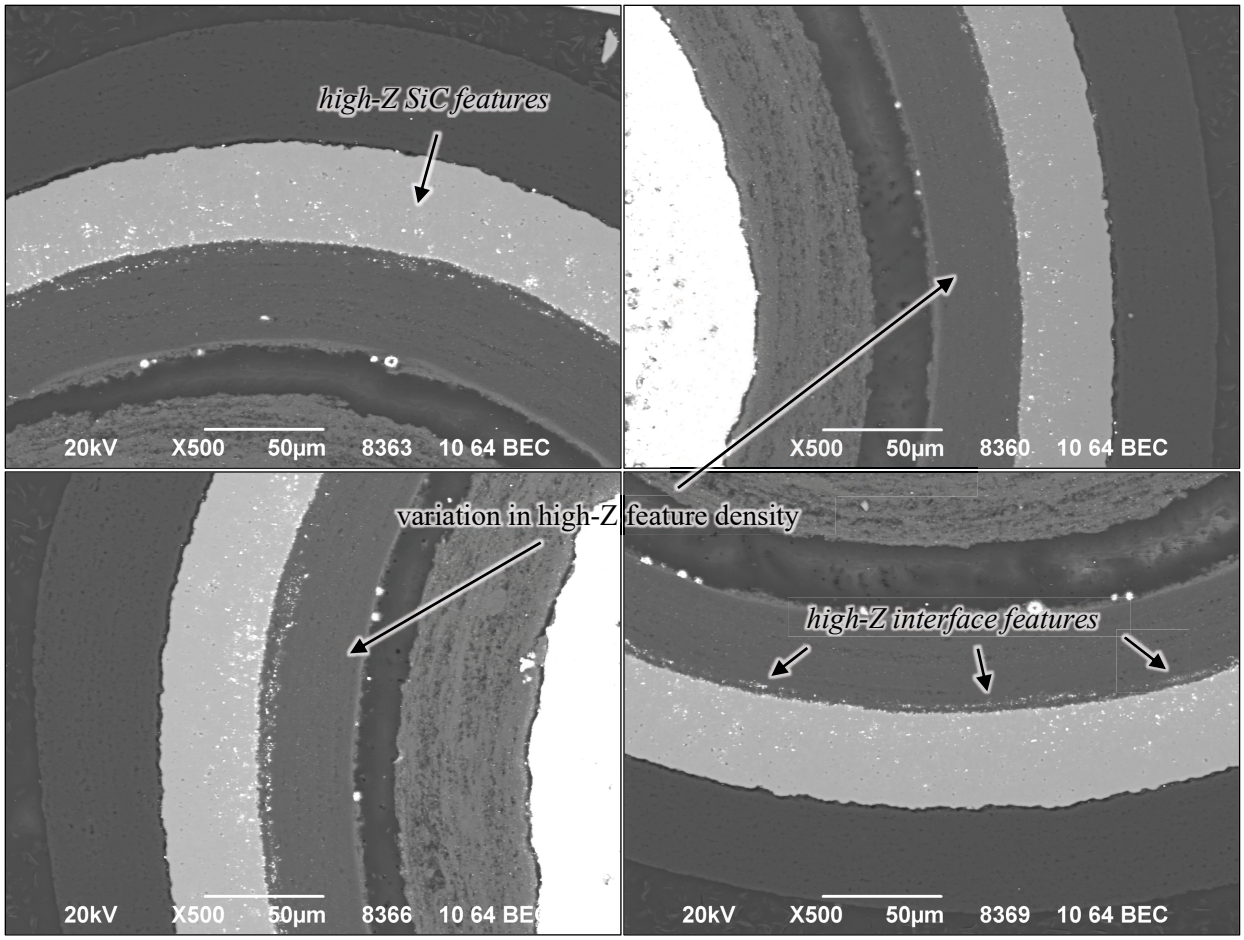

Figure 7-7. Four 500× SEM magnification BEC images of Particle 212-RS08 with ^{110m}Ag M/C < 0.35.

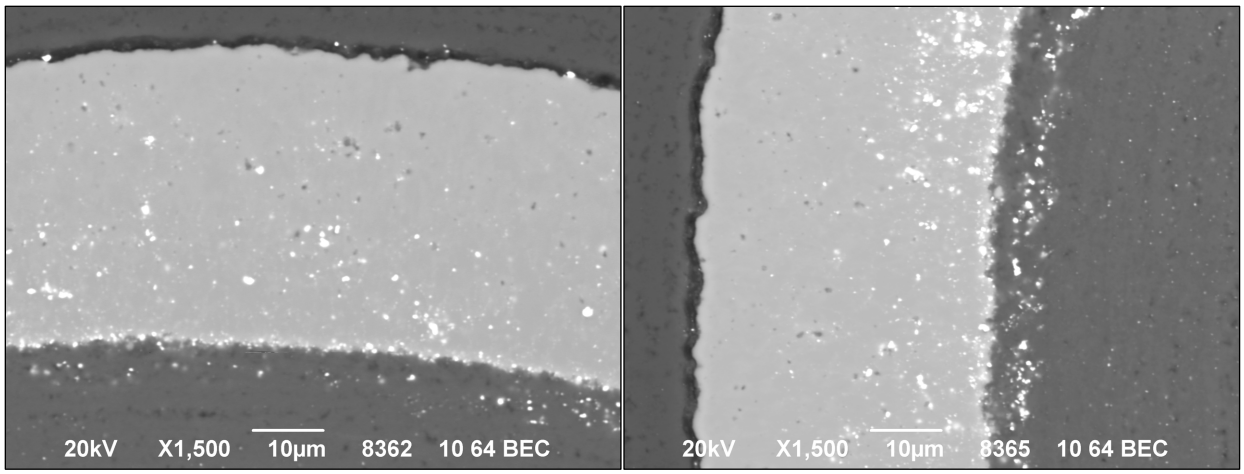

Figure 7-8. Two 1,500× SEM magnification BEC images of Particle 212-RS08 with ^{110m}Ag M/C < 0.35.

PARTICLE 212-RS44 OVERVIEW

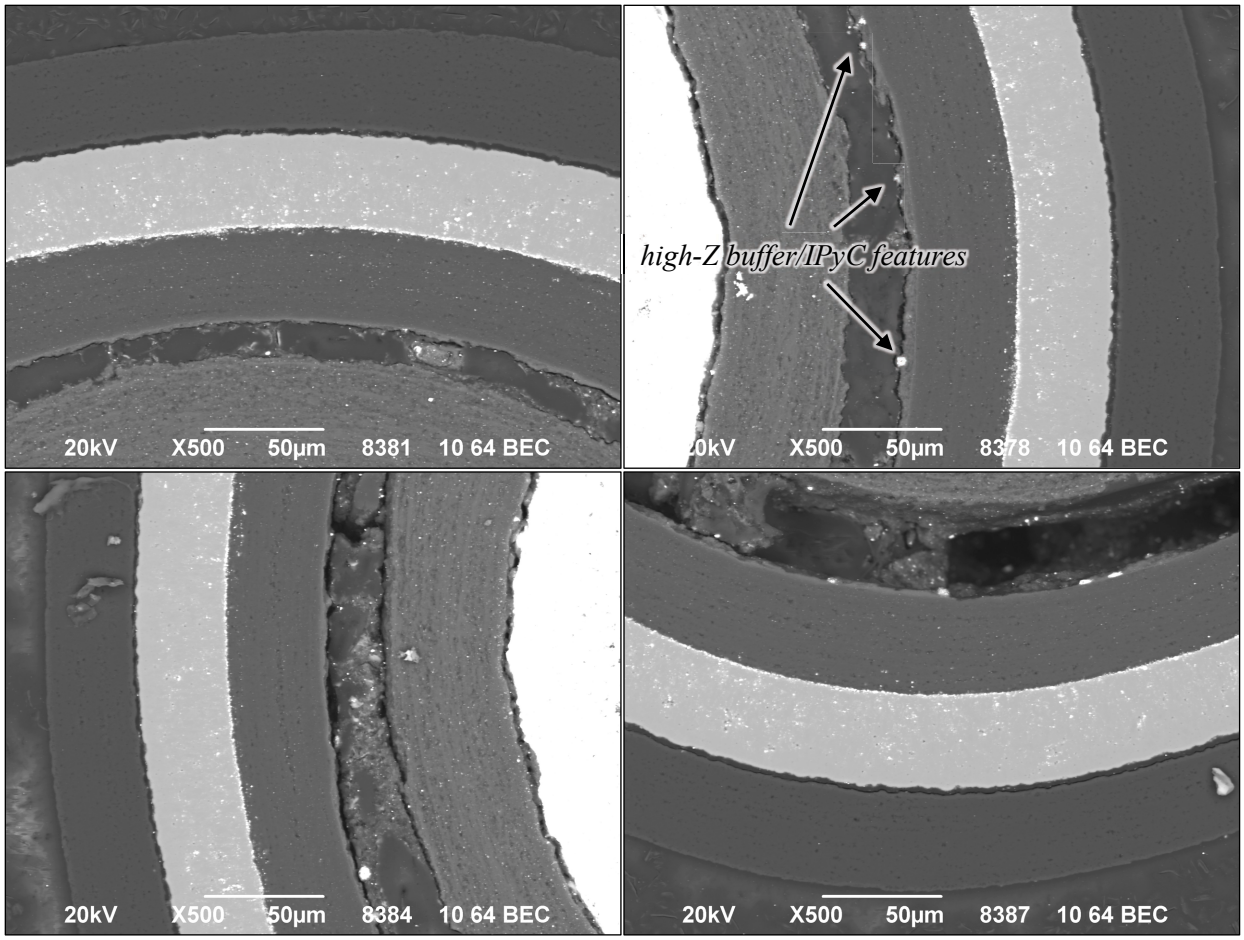

Figure 7-9. Four 500× SEM magnification BEC images of Particle 212-RS44 with ^{110m}Ag M/C < 0.42.

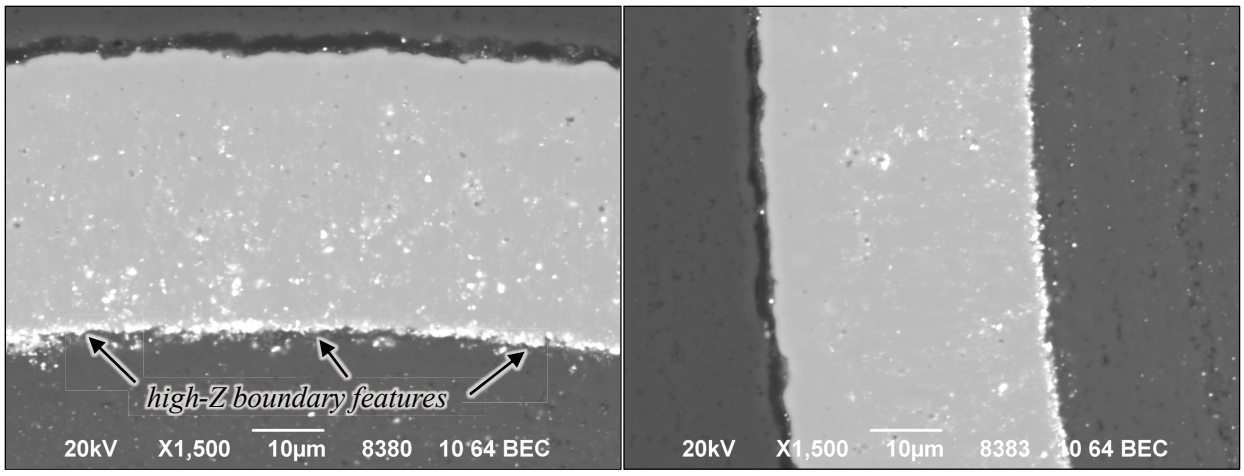

Figure 7-10. Two 1,500× SEM magnification BEC images of Particle 212-RS44 with ^{110m}Ag M/C < 0.42.

PARTICLE 212-RS43 OVERVIEW

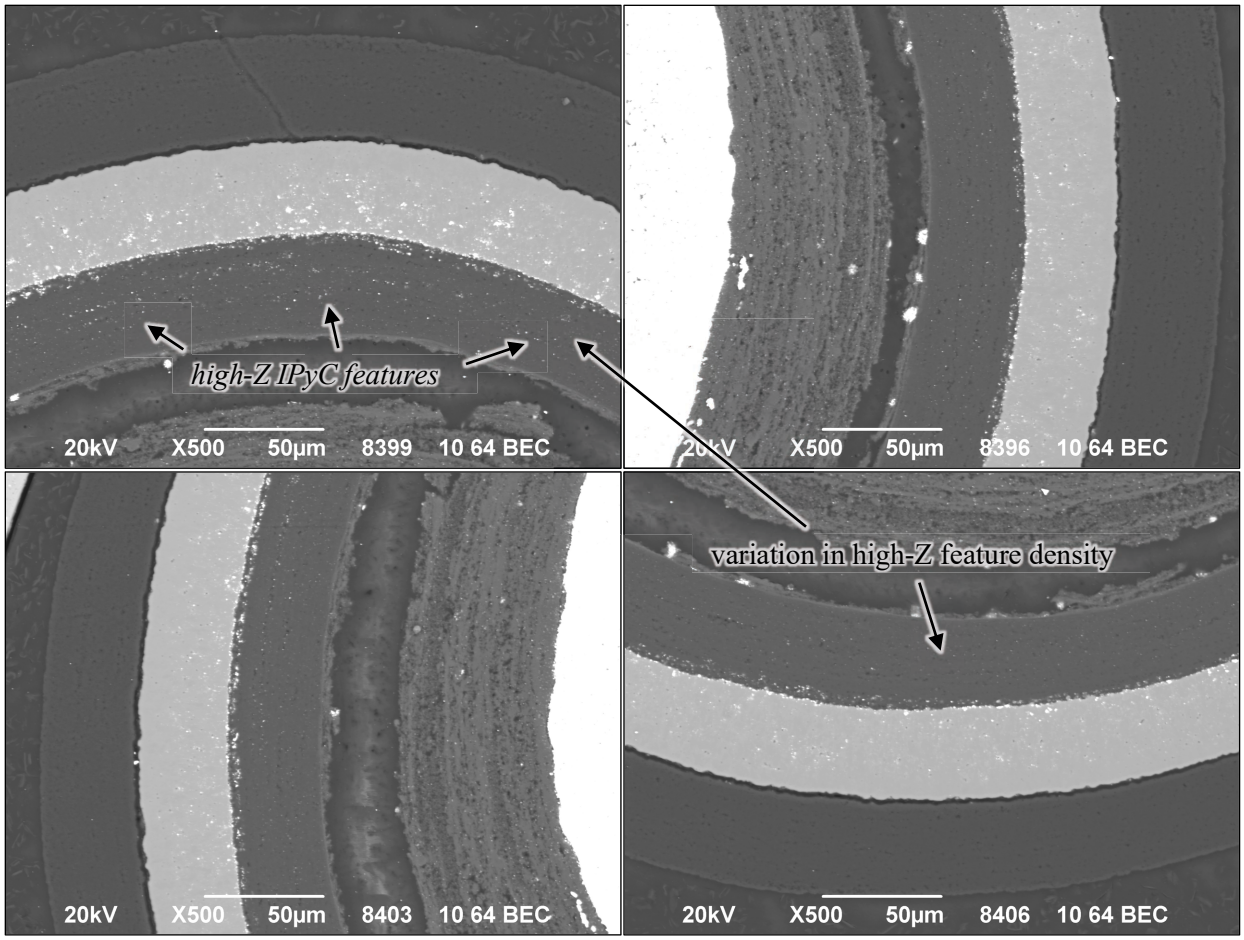

Figure 7-11. Four 500× SEM magnification BEC images of Particle 212-RS43 with ^{110m}Ag M/C < 0.40.

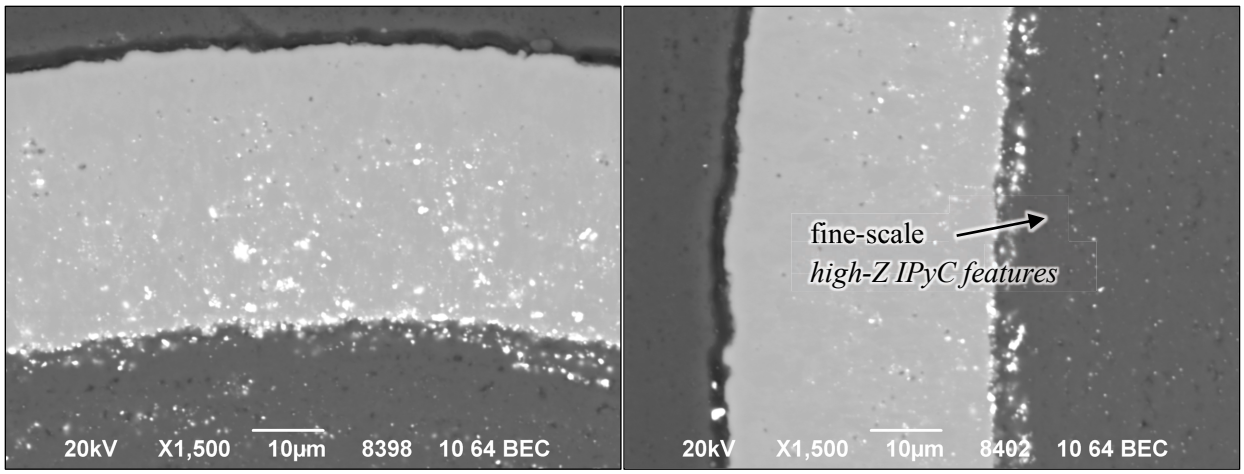

Figure 7-12. Two 1,500× SEM magnification BEC images of Particle 212-RS43 with ^{110m}Ag M/C < 0.40.

PARTICLE 212-RS45 OVERVIEW

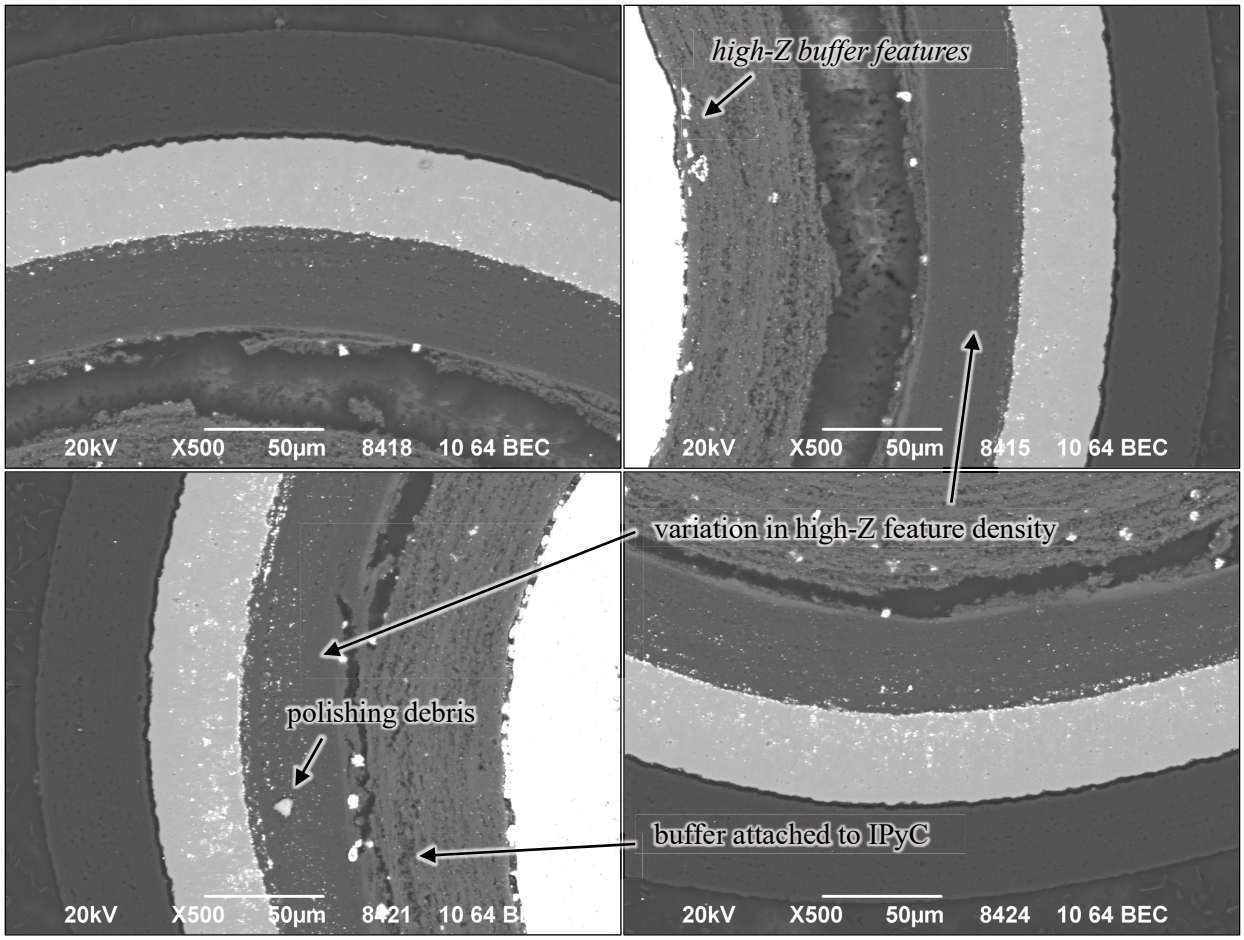

Figure 7-13. Four 500× SEM magnification BEC images of Particle 212-RS45 with ^{110m}Ag M/C < 0.40.

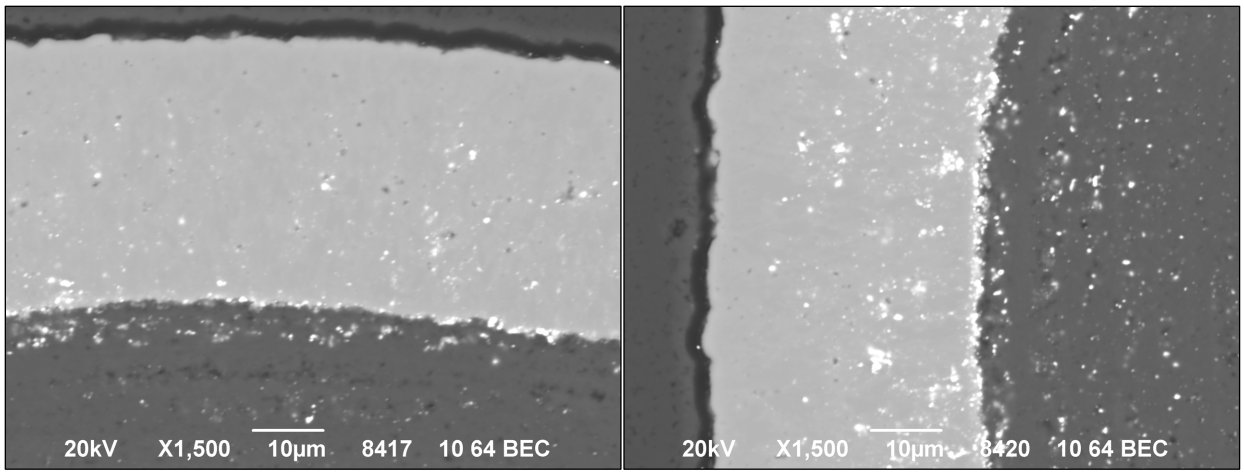

Figure 7-14. Two 1,500× SEM magnification BEC images of Particle 212-RS45 with ^{110m}Ag M/C < 0.40.

PARTICLE 212-RS05 OVERVIEW

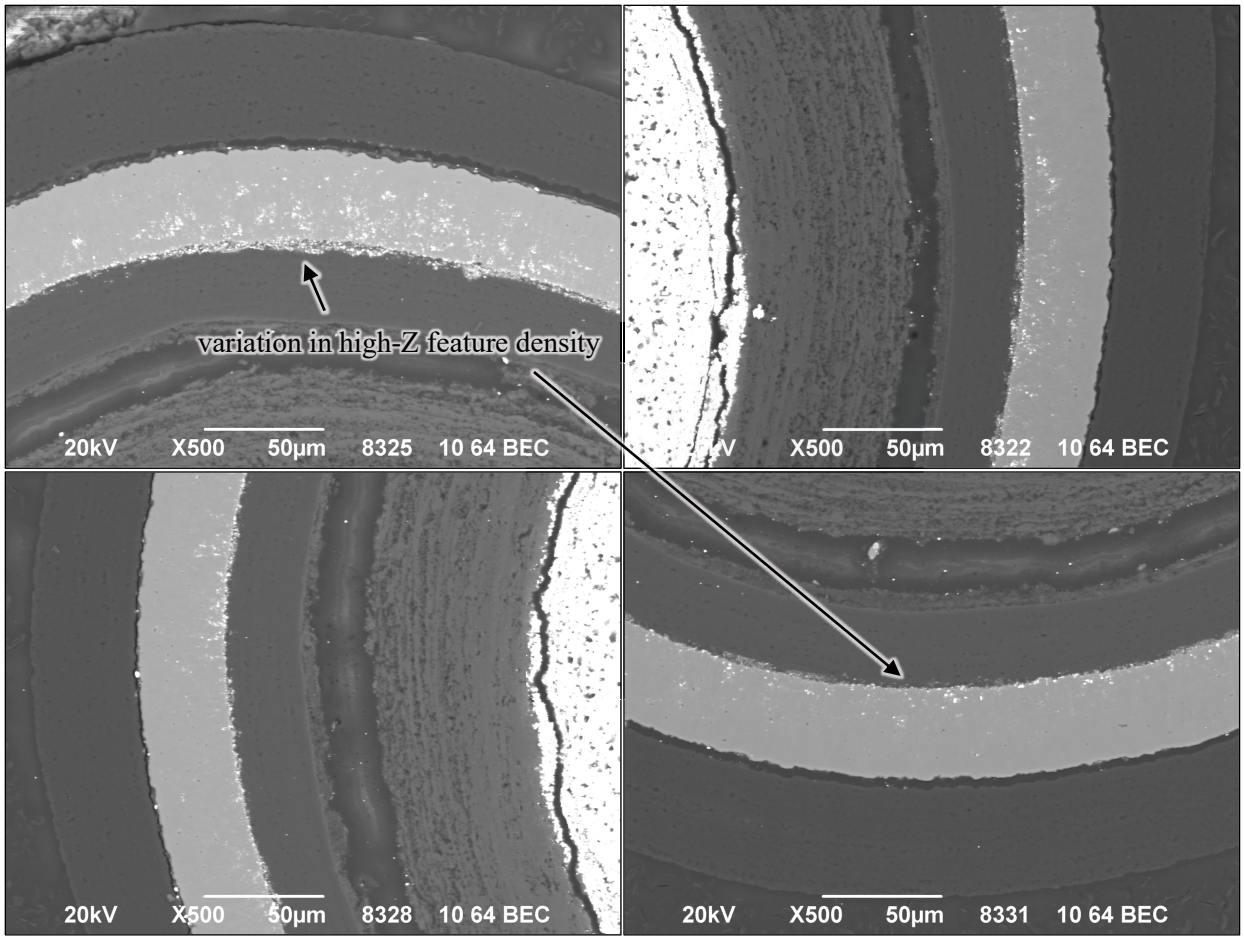

Figure 7-15. Four 500× SEM magnification BEC images of Particle 212-RS05 with ^{110m}Ag M/C = 0.68.

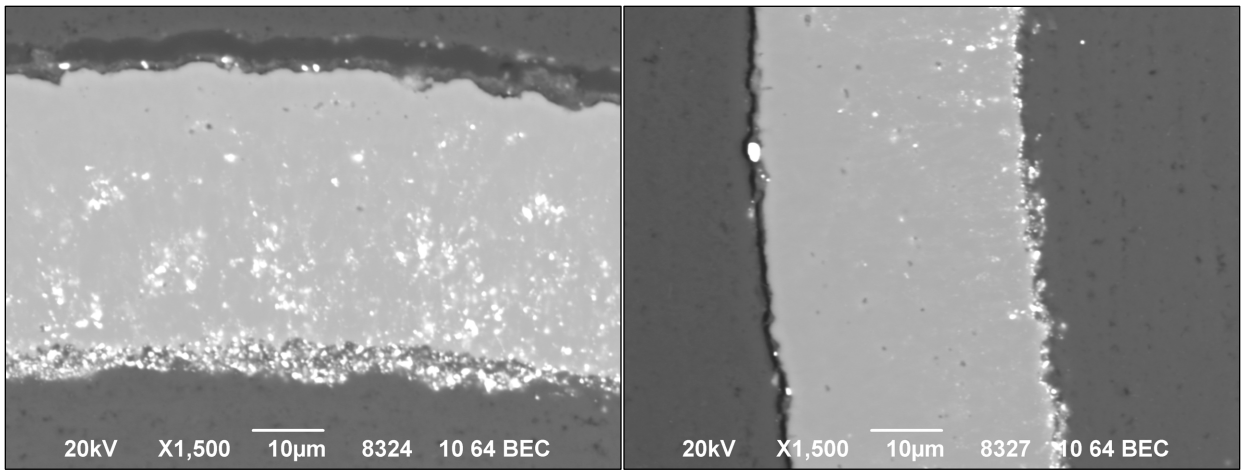

Figure 7-16. Two 1,500× SEM magnification BEC images of Particle 212-RS05 with ^{110m}Ag M/C = 0.68.

PARTICLE 212-RS16 OVERVIEW

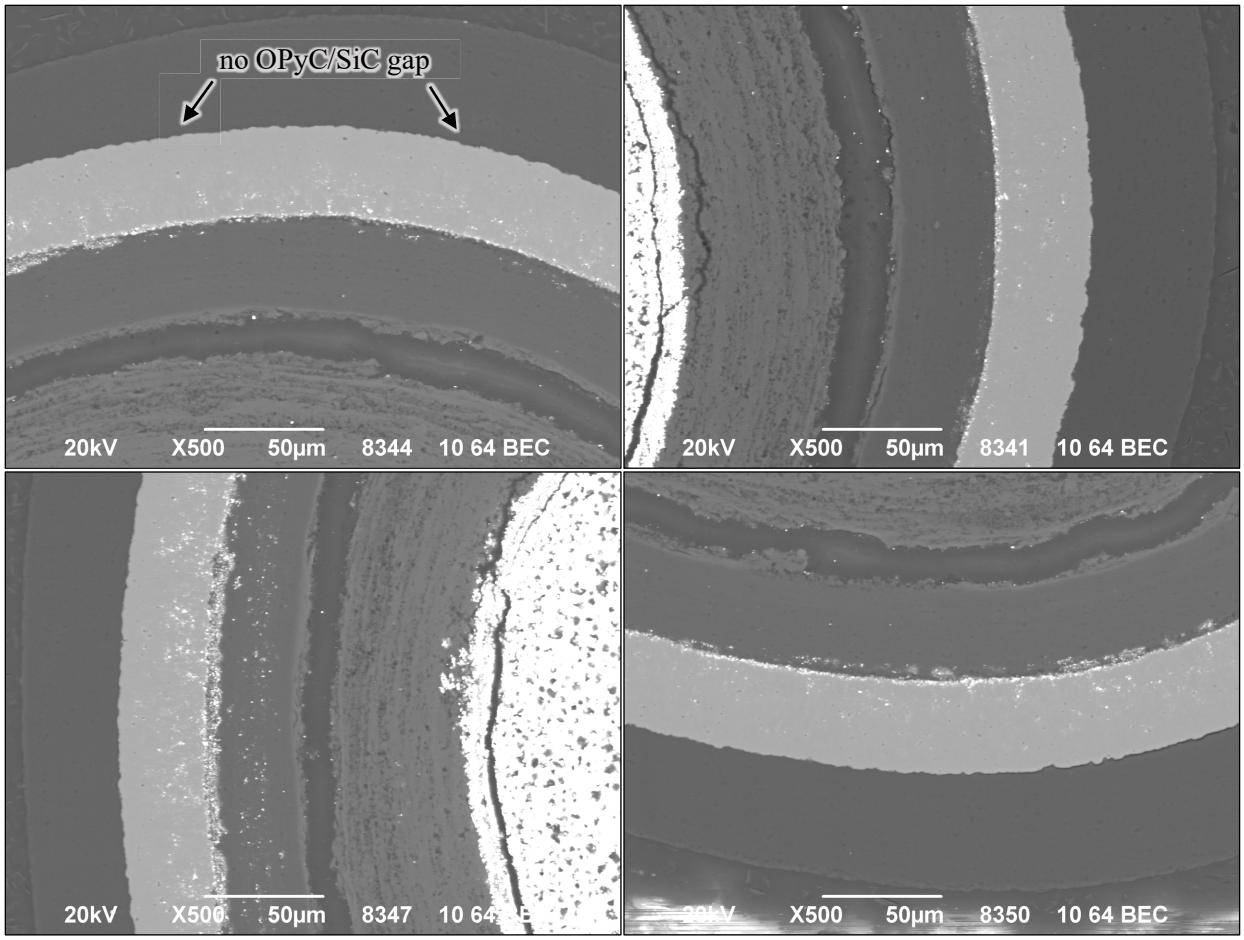

Figure 7-17. Four 500× SEM magnification BEC images of Particle 212-RS16 with ^{110m}Ag M/C = 0.60.

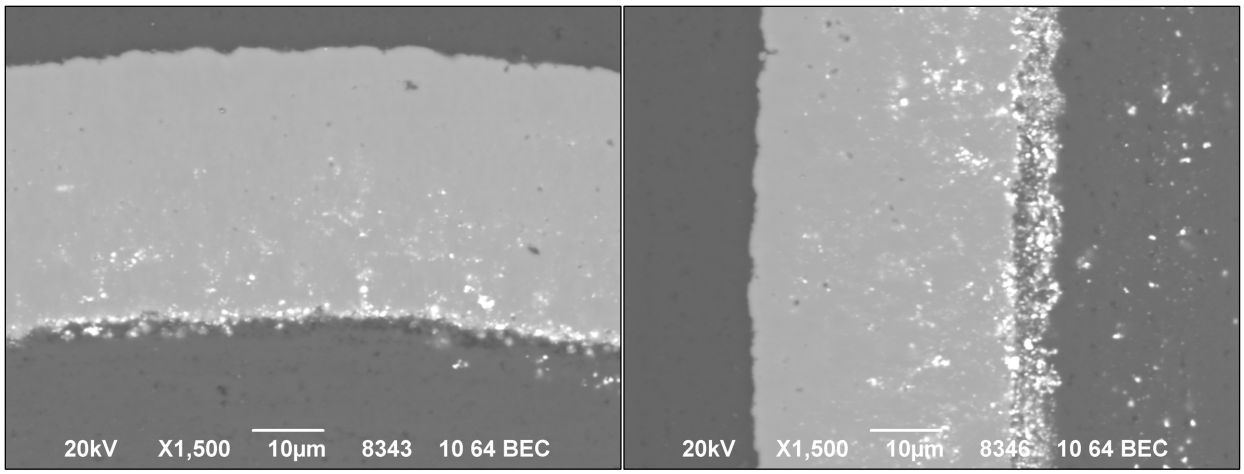

Figure 7-18. Two 1,500× SEM magnification BEC images of Particle 212-RS16 with ^{110m}Ag M/C = 0.60.

There were two additional location-based classes of high-Z features that involved the buffer layer. The four RS-series particles listed in Table 7-1 that released the most silver (having residual ^{110m}Ag inventories below the MDL) exhibited bright spots in the residual buffer material that was still attached to the IPyC. These were catalogued as *high-Z buffer/IPyC features* (Figure 7-9) and were not observed in the two RS-series particles with measurable ^{110m}Ag. Large isolated bright spots were also observed in the buffer layer within 25 µm of the kernel. These were catalogued as *high-Z buffer features* (Figure 7-13). *High-Z buffer features* were not widespread, but they were observed in all of the RS-series particles that were analyzed.

In addition to the bright spots from the numerous *high-Z SiC features*, there were also dark spots associated with *low-Z SiC features* in all particles that were analyzed. These features appeared to be more prevalent in the outer half of the SiC layer. Micrographs were acquired of the same region using either BEC or SEI to determine whether dark spots were dense regions of lower-Z or surface topography as a result of grain pull-out during polishing. Figure 7-19 and Figure 7-20 show corresponding BEC/SEI micrographs of locations in Particle 212-RS08 and Particle 212-RS08, respectively. Both dense, low-Z regions and surface topography were observed in the SEI micrographs, with corresponding features in the BEC micrographs. The *low-Z SiC features* are likely carbon-rich regions resulting from formation and out-diffusion of silicides. Some dark spots visible in the BEC micrographs without corresponding features in the SEI micrographs indicate *low-Z SiC features* below the surface. The paired BEC/SEI micrographs in Figure 7-19 and Figure 7-20 a show the embedded nature of the *high-Z SiC features*, and many bright spots in the BEC micrographs do not have corresponding features in the SEI micrographs.

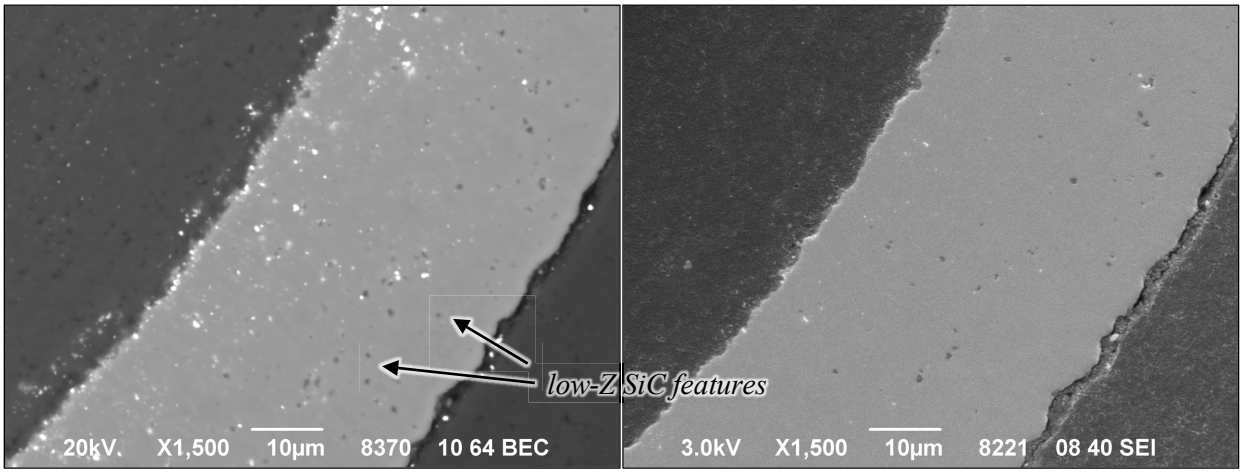

Figure 7-19. BEC and SEI micrographs of the same region of Particle 212-RS08 with ^{110m}Ag M/C < 0.35.

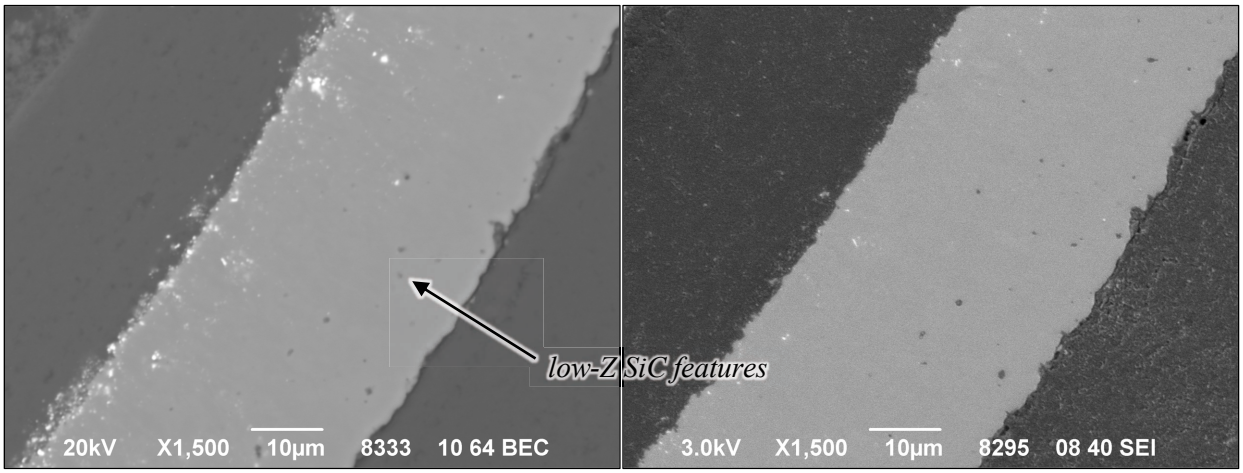

Figure 7-20. BEC and SEI micrographs of the same region of Particle 212-RS05 with ^{110m}Ag M/C = 0.68.

7.3 ELEMENTAL ANALYSIS OF NORMAL PARTICLES

The compositions of select features observed in the TRISO layers were determined by EDS using Point-ID analysis. *High-Z SiC features, high-Z boundary features, high-Z interface features,* and *high-Z IPyC features* in all particles were selected for analysis. These features were further categorized into four composition types: *U-rich*, *Pd-rich*, *U-complex*, and *Pd-complex*. Complex features contained varying contributions from uranium, palladium, rhodium, and ruthenium and were further identified by their predominant species, which was always either uranium or palladium. The complex features showed significant variation in the concentration of the non-predominant species, especially rhodium and ruthenium. In some instances, no rhodium or ruthenium were observed in the complex features, with only measurable EDS peaks from palladium, uranium, and the surrounding native layer. Some complex features also showed the presence of plutonium. Features that included uranium with an apparent concentration that was five times higher than the apparent concentration of palladium, rhodium, and ruthenium were categorized as *U-rich features*. Features that included palladium with an apparent concentration that was five times higher than the apparent concentration uranium, rhodium, and ruthenium were categorized as *Pd-rich features*.

Some *U-rich features* included significant concentrations of zirconium and/or molybdenum; nevertheless, these were counted as *U-rich features*. Figure 7-21 shows a *U-rich SiC feature* and a *U-rich boundary feature* that included zirconium. The corresponding EDS spectra for these features are plotted in Figure 7-22, along with the spectra from a featureless reference area in the SiC layer. All analyzed particles had *U-rich features*. The majority of the analyzed *high-Z boundary features* were determined to be *U-rich*, and many of the *high-Z SiC features* were *U-rich*. In addition, a few *U-rich features* were observed in the IPyC/SiC interface region in Particle 212-RS08 and Particle 212-RS43.

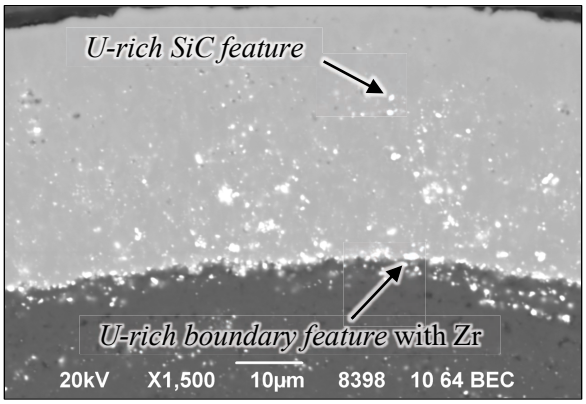

Figure 7-21. Examples of a *U-rich SiC feature* and a *U-rich boundary feature* in Particle 212-RS43.

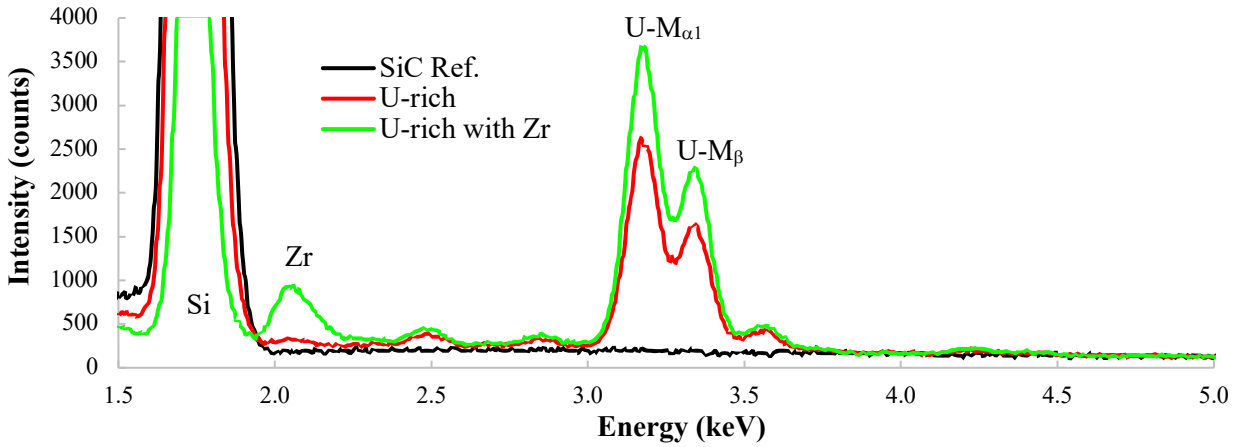

Figure 7-22. EDS spectra from the *U-rich features* labeled in Figure 7-21.

Figure 7-23 shows examples of a *Pd-rich SiC feature* and a *Pd-complex SiC feature* in Particle 212-RS16, and Figure 7-24 shows the corresponding EDS spectra. The *Pd-rich features* were only observed in the outer half of the SiC layer of Particle 212-RS16.

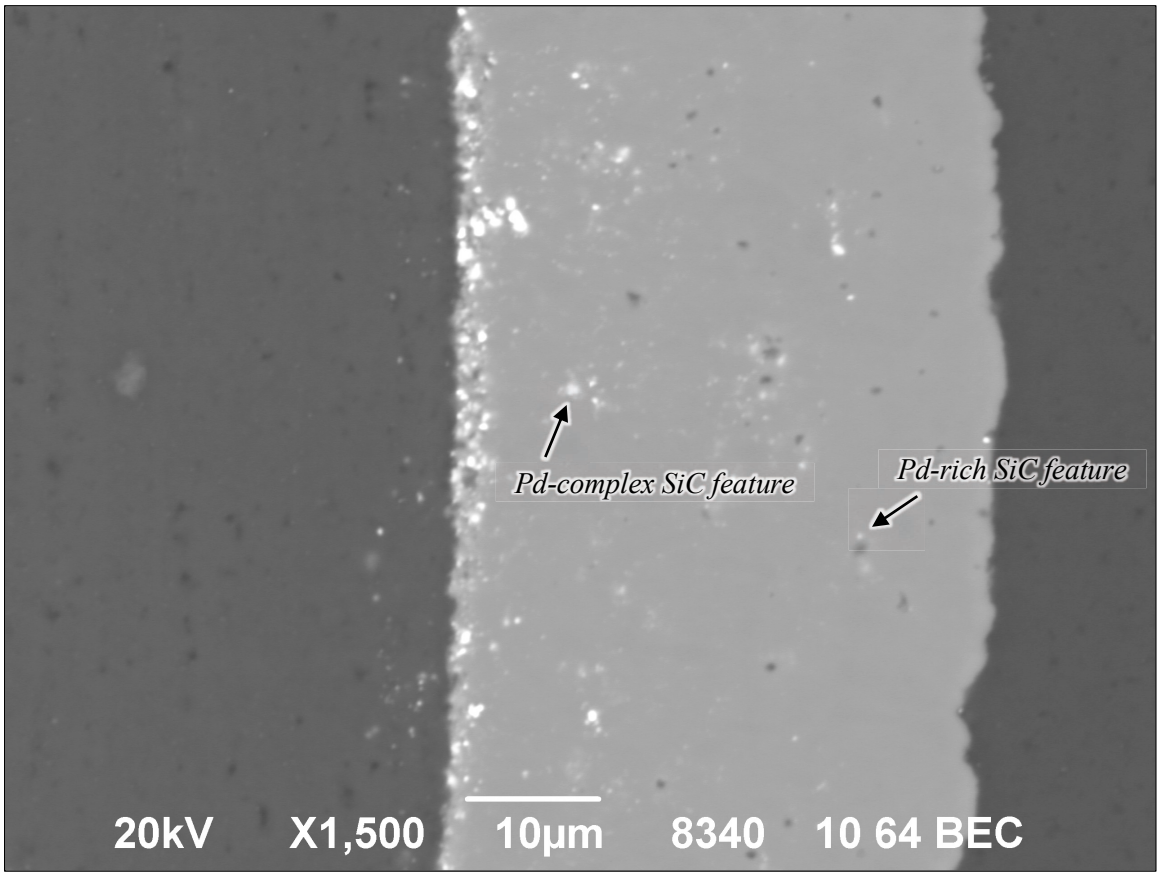

Figure 7-23. Examples of a *Pd-rich SiC feature* and a *Pd-complex SiC feature* in Particle 212-RS16.

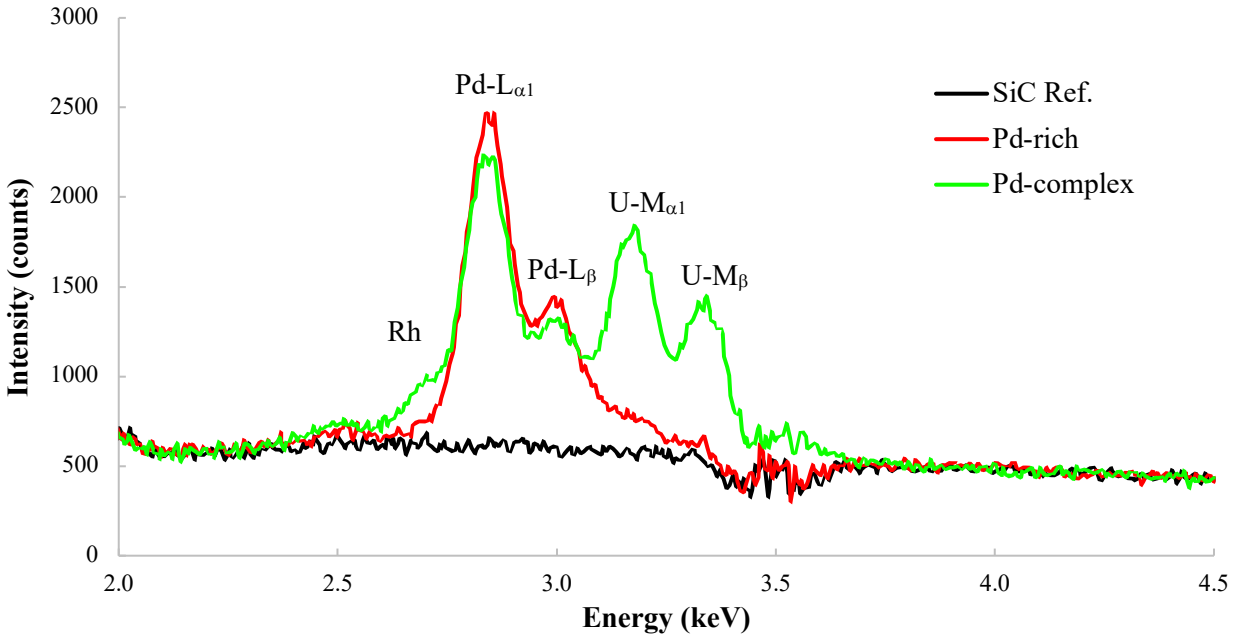

Figure 7-24. EDS spectra from the *Pd-rich* and *Pd-complex features* labeled in Figure 7-23.

The *Pd-complex* and *U-complex features* varied considerably in composition, and this compositional variation was generally associated with the location of the feature. The *Pd-complex* and *U-complex* composition types were observed for all four location-based classes in the IPyC and SiC layers: *high-Z SiC features, high-Z boundary features, high-Z interface features,* and *high-Z IPyC features*. Figure 7-25 and Figure 7-26 show an example of a *Pd-complex SiC feature* that included significant rhodium, ruthenium, and plutonium, as well as a *Pd-complex SiC feature* that was primarily just palladium and uranium. A *U-complex SiC feature* is also shown. The identification of plutonium in Figure 7-26 was based on the relative intensity of the peak from 3.178 keV U-M_α x-rays compared to the intensity of a higher energy peak that could be from overlapping signal from 3.337 keV U-M_β and 3.350 keV Pu-M_α x-rays. The peak for the *Pd-complex* in Figure 7-26 is higher than expected from just U-M_β x-rays. The *Pd-complex* and *U-complex features* that included rhodium, ruthenium, and plutonium were primarily located in the IPyC, in the IPyC/SiC interface, or in the inner half of the SiC layer closest to the IPyC. The *Pd-complex* and *U-complex features* with only measurable EDS peaks from palladium, uranium, and the surrounding native layer were mostly observed in the outer half of the SiC layer; this was similar to observations made during SEM/EDS analysis of AGR-2 Compact 6-4-2 (Hunn et al. 2018c).

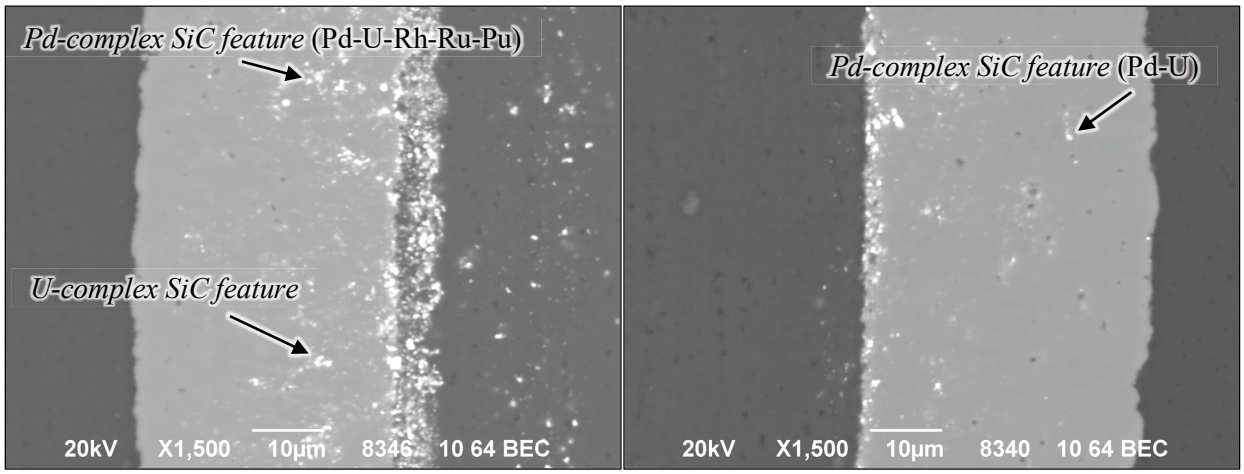

Figure 7-25. Examples of *Pd-complex features* and a *U-complex feature* in Particle 212-RS16.

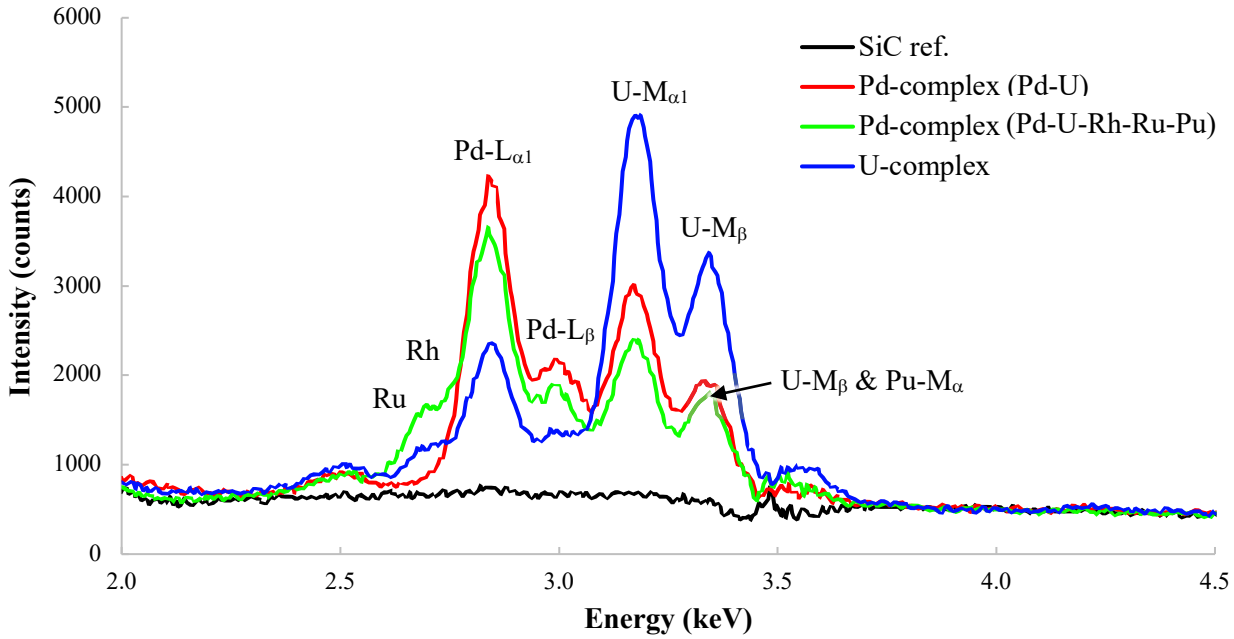

Figure 7-26. EDS spectra from the *Pd-complex* and *U-complex features* labeled in Figure 7-25.

The *high-Z interface features* were mostly *Pd-complex* and *U-complex* composition types, while the composition of the *high-Z IPyC features* were commonly *Pd-complex*, *U-complex*, or *U-rich* composition types. Figure 7-27 and Figure 7-28 show the location and composition, respectively, of a *Pd-complex interface feature* and a *Pd-complex IPyC feature* in Particle 212-RS16. As mentioned in the preceding paragraph, the *Pd-complex* and *U-complex features* observed in the IPyC and IPyC interface shared a common composition with the complexes in the SiC layer that contained rhodium, ruthenium, and palladium, in addition to palladium, uranium, and silicon. Whereas the incorporation of silicon in the metal complexes can only be inferred in the *high-Z SiC features* using SEM/EDS analysis, because of the silicon x-ray contribution from the SiC layer, the silicon x-ray peak for the *Pd-complex IPyC feature* shown in Figure 7-28 indicates the complexes contain silicides. Because this feature was remote from the SiC layer, the silicon x-ray peak is not considered a matrix effect; in addition, the intensity of the peak is too high to be associated with a system artifact.

Figure 7-28 also shows the presence of cesium and barium in the IPyC reference signal. This was a common observation, indicating the general presence of these fission products throughout the IPyC.

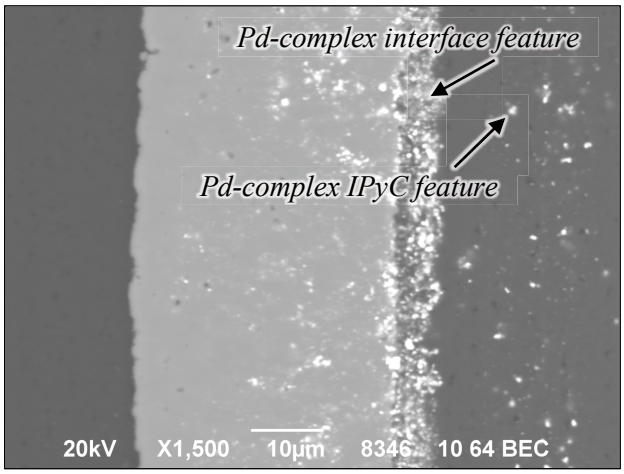

Figure 7-27. Examples of a *Pd-complex interface feature* and a *Pd-complex IPyC feature* in Particle 212-RS16.

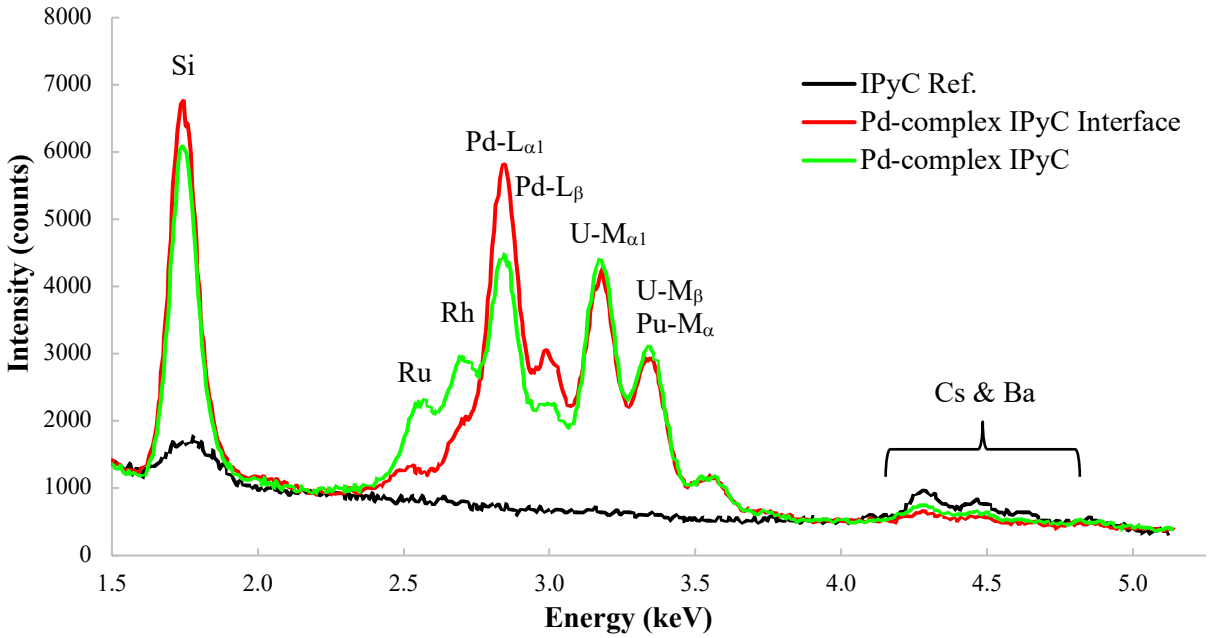

Figure 7-28. EDS spectra from the *Pd-complex features* labeled in Figure 7-27.

The fine-scale *high-Z IPyC features* had a composition that was different than the *high-Z IPyC features* appearing in the BEC micrographs with a higher intensity, such as those shown in Figure 7-27 and Figure 7-28. Figure 7-29 and Figure 7-30 show an example of a fine-scale h*igh-Z IPyC features* that exhibited the most typical composition for this type of feature. The spectrum in Figure 7-30 shows that this fine-scale feature was of the *U-rich* composition type, with a significant concentration of zirconium. The EDS spectrum for this feature also showed silicon, strontium, cesium, and barium. The trace silicon, which also appeared in the IPyC reference spectrum, was likely a system artifact from internal fluorescence of the Oxford X-Max 50 silicon drift detector. The strontium, cesium, and barium were likely from the surrounding IPyC, as they were observed in nearly all Point-ID analyses of high-Z feature or reference areas in the IPyC layer.

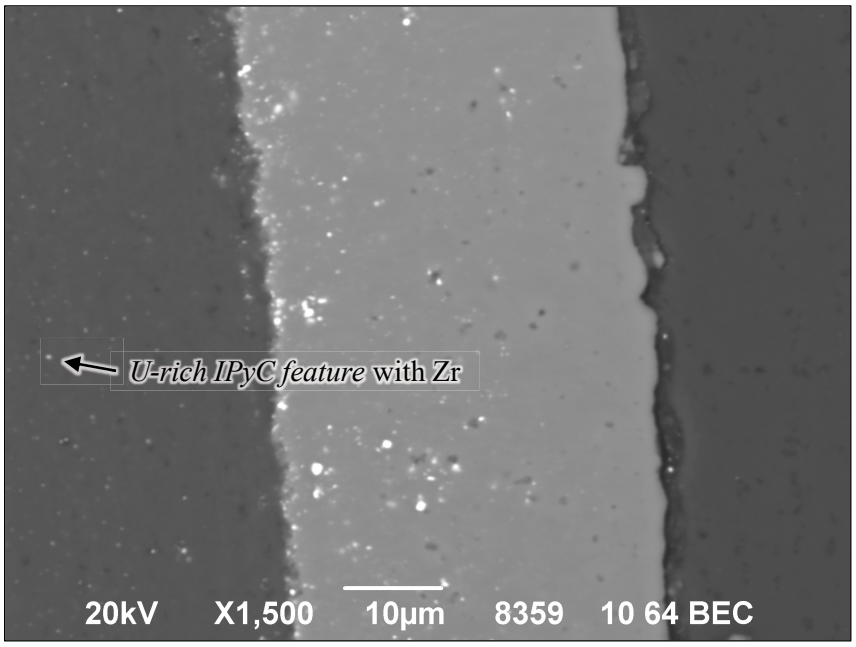

Figure 7-29. Example of a *U-rich IPyC feature* in the fine-scale *high-Z IPyC features* in Particle 212-RS08.

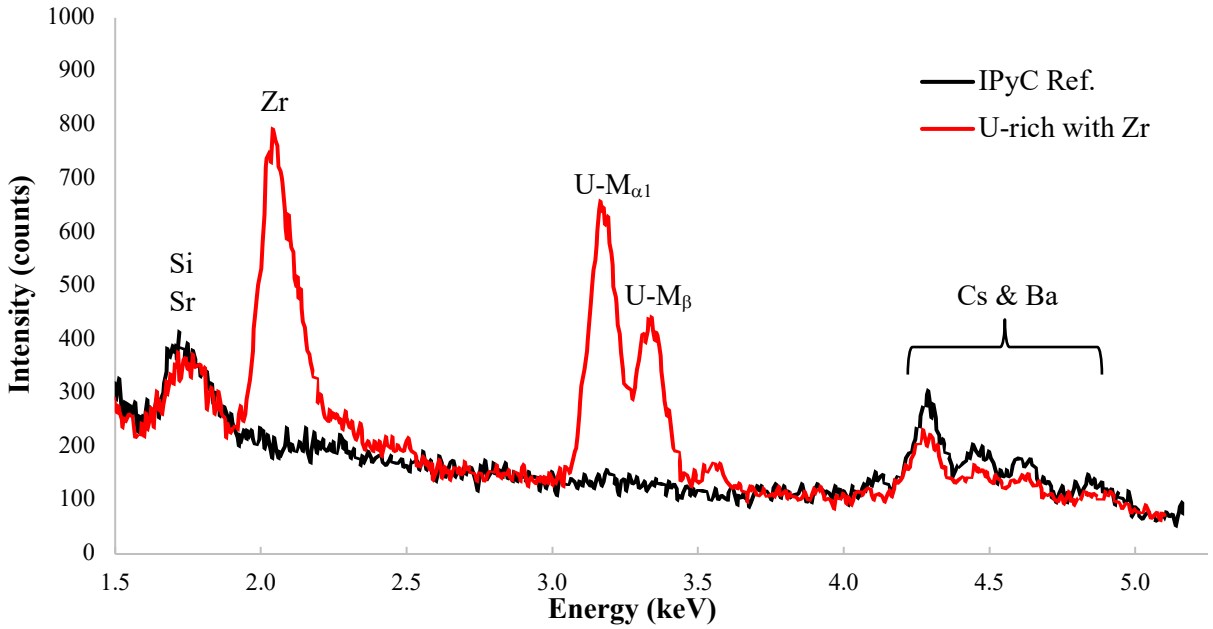

Figure 7-30. EDS spectra from the *U-rich IPyC feature* labeled in Figure 7-29.

The compositional types observed for each location-based category were tabulated, and Table 7-2 through Table 7-6 list the results as the fraction observed in each particle out of all features analyzed in that particle. For the tabulated results presented in Table 7-2 and Table 7-3, the *high-Z SiC features* were divided into two sub-categories, namely, *high-Z outer SiC features* and *high-Z inner SiC features*. This delineation helps to illustrate the trends observed as a function of feature location within the SiC layer. The compiled results in Table 7-2 through Table 7-6 represent the combined data from about 500 individual EDS spectra.

Table 7-2. Relative population of each compositional type observed in *high-Z outer SiC features*

	^{110m}Ag retention below MDL				Measurable ^{110m}Ag	
Type	**212-RS08**	**212-RS44**	**212-RS43**	**212-RS45**	**212-RS05**	**212-RS16**
U-rich [a]	0.92 (0.00)	0.10 (1.00)	0.35 (0.17)	0.53 (0.00)	0.00 (0.00)	0.06 (0.00)
U-complex	0.08	0.20	0.00	0.06	0.13	0.06
Pd-rich	0.00	0.00	0.00	0.00	0.00	0.31
Pd-complex [b]	0.00 (0.00)	0.70 (0.71)	0.65 (0.09)	0.41 (0.29)	0.88 (0.71)	0.56 (0.44)

[a] Values in parentheses indicate the fractions of *U-rich features* that included significant Zr.
[b] Values in parentheses indicate the fractions of *Pd-complex features* that did not include significant Rh or Ru.

Table 7-3. Relative population of each compositional type observed in *high-Z inner SiC features*

	^{110m}Ag retention below MDL				Measurable ^{110m}Ag	
Type	**212-RS08**	**212-RS44**	**212-RS43**	**212-RS45**	**212-RS05**	**212-RS16**
U-rich [a]	0.76 (0.00)	0.75 (0.17)	0.50 (0.23)	0.43 (0.11)	0.27 (0.50)	0.30 (0.50)
U-complex	0.14	0.06	0.12	0.19	0.13	0.15
Pd-rich	0.00	0.00	0.00	0.00	0.00	0.00
Pd-complex [b]	0.10 (0.00)	0.19 (0.00)	0.38 (0.00)	0.38 (0.38)	0.60 (0.11)	0.55 (0.00)

[a] Values in parentheses indicate the fractions of *U-rich features* that included significant Zr.
[b] Values in parentheses indicate the fractions of *Pd-complex features* that did not include significant Rh or Ru.

Table 7-4. Relative population of each compositional type observed in *high-Z boundary features*

	^{110m}Ag retention below MDL				Measurable ^{110m}Ag	
Type	**212-RS08**	**212-RS44**	**212-RS43**	**212-RS45**	**212-RS05**	**212-RS16**
U-rich [a]	1.00 (0.50)	0.50 (0.75)	0.83 (0.60)	0.57 (0.25)	0.50 (0.33)	0.78 (0.29)
U-complex	0.00	0.00	0.17	0.14	0.33	0.11
Pd-rich	0.00	0.00	0.00	0.00	0.00	0.00
Pd-complex [b]	0.00 (0.00)	0.50 (0.00)	0.00 (0.00)	0.29 (0.00)	0.17 (0.00)	0.11 (0.00)

[a] Values in parentheses indicate the fractions of *U-rich features* that included significant Zr.
[b] Values in parentheses indicate the fractions of *Pd-complex features* that did not include significant Rh or Ru.

Table 7-5. Relative population of each compositional type observed in *high-Z interface features*

	^{110m}Ag retention below MDL				Measurable ^{110m}Ag	
Type	**212-RS08**	**212-RS44**	**212-RS43**	**212-RS45**	**212-RS05**	**212-RS16**
U-rich [a]	0.13 (0.00)	0.00 (0.00)	0.15 (0.50)	0.00 (0.00)	0.00 (0.00)	0.00 (0.00)
U-complex	0.25	0.14	0.31	0.30	0.00	0.00
Pd-rich	0.00	0.00	0.00	0.00	0.00	0.00
Pd-complex [b]	0.63 (0.00)	0.86 (0.00)	0.54 (0.00)	0.70 (0.00)	1.00 (0.00)	1.00 (0.00)

[a] Values in parentheses indicate the fractions of *U-rich features* that included significant Zr.
[b] Values in parentheses indicate the fractions of *Pd-complex features* that did not include significant Rh or Ru.

Table 7-6. Relative population of each compositional type observed in *high-Z IPyC features*

	^{110m}Ag retention below MDL				Measurable ^{110m}Ag	
Type	**212-RS08**	**212-RS44**	**212-RS43**	**212-RS45**	**212-RS05**	**212-RS16**
U-rich [a]	1.00 (1.00)	0.50 (1.00)	0.75 (1.00)	0.73 (1.00)	1.00 (0.00)	0.00 (0.00)
U-complex	0.00	0.50	0.13	0.18	0.00	0.75
Pd-rich	0.00	0.00	0.00	0.00	0.00	0.00
Pd-complex [b]	0.00	0.00	0.13	0.09	0.00	0.25

[a] Values in parentheses indicate the fractions of *U-rich features* that included significant Zr.
[b] Values in parentheses indicate the fractions of *Pd-complex features* that did not include significant Rh or Ru.

Clear trends in fission product distribution as a function of silver retention have been identified by SEM and EDS analyses of AGR fuel particles when particles that released almost all their silver inventory were compared to those that retained almost all their silver inventory (Gerczak et al. 2018). These trends were likely related to the irradiation temperatures of the individual particles, for which silver retention was a convenient indicator. The six RS-series particles selected from AGR-2 Compact 2-1-2 do not represent the bounding behaviors for silver retention that are most useful for this type of trending analysis. The four particles with ^{110m}Ag retention below the MDL likely lost most of their silver, but it is possible that their remaining inventory may have been as high as the MDL (Table 7-1). While the two particles with measurable ^{110m}Ag inventory retained more silver than the other four, they still lost a significant part of their starting inventory and may not have experienced irradiation conditions markedly different from particles with ^{110m}Ag inventory that was approximately equal to the average MDL. The compiled results in Table 7-2 through Table 7-6 suggest that there may be a few trends in the distribution fractions for the two particles with measurable ^{110m}Ag vs. those with ^{110m}Ag inventory below the MDL. However, such analysis is better suited to samples that provide clearer bounding conditions, so these trends are not discussed herein. Future studies are planned to include Particles 212-RS01 and 212-RS03, which had significantly higher retained ^{110m}Ag inventories and likely released very little silver.

The compositions of the large high-Z features located in the residual buffer material that remained attached to the IPyC layer where the bulk of the buffer had detached were consistent in all examined features. These *high-Z buffer/IPyC features*, such as the feature identified in Figure 7-31, contained uranium and zirconium (Figure 7-32). Trace amounts of cesium, barium, and strontium were also apparent in the EDS spectra, but these probably came from the surrounding material. The apparent concentrations of U:Zr in atomic percent ranged from 0.9:1.0 to 1.6:1.0 for all features analyzed. The compositions in the *high-Z buffer/IPyC features* were similar to the compositions in the *U-rich SiC features* and *U-rich boundary features* like those shown in Figure 7-21 and Figure 7-22.

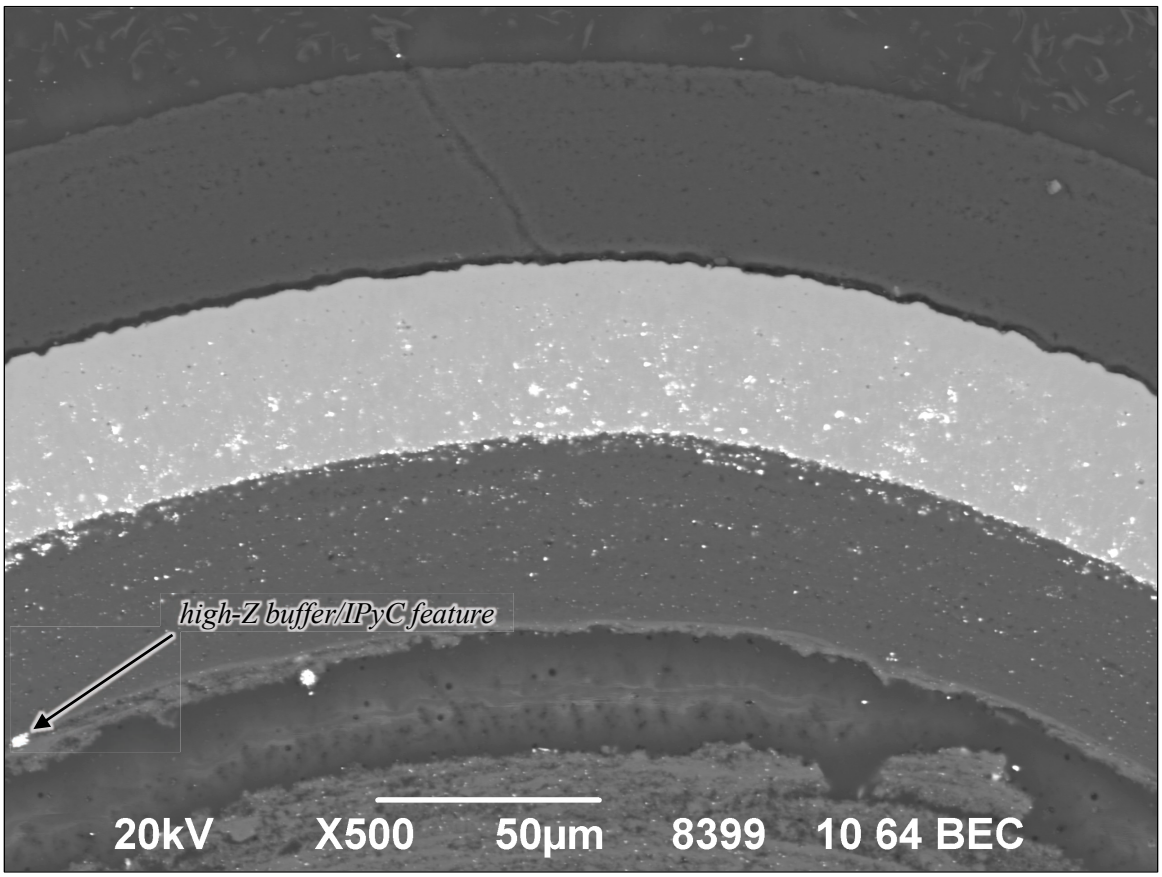

Figure 7-31. Example of a *U-rich buffer/IPyC feature* with Zr in Particle 212-RS43.

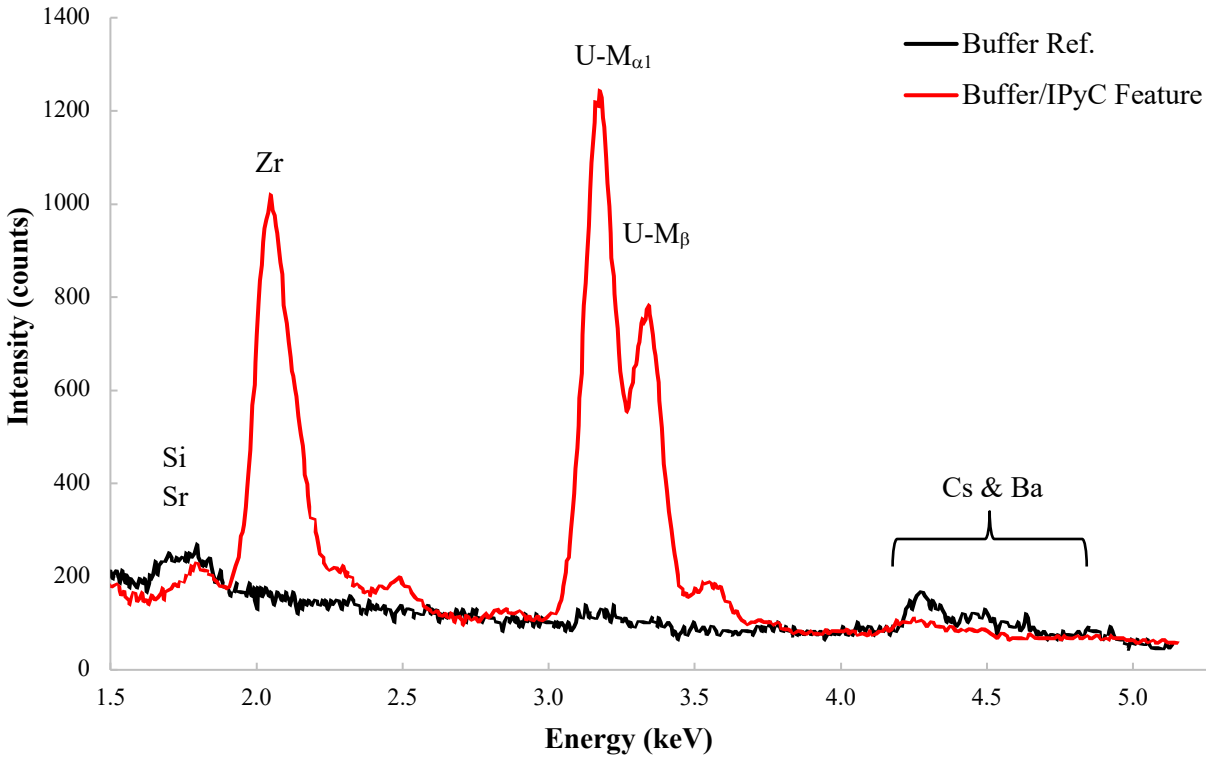

Figure 7-32. EDS spectra from the *U-rich buffer/IPyC feature* with Zr labeled in Figure 7-31.

The *high-Z buffer features* that were analyzed had a consistent composition, with major constituents of carbon, oxygen, ruthenium, and uranium. Some features also included cadmium, molybdenum, technetium, silicon, rhodium, zirconium, and minor amounts of palladium. Figure 7-33 shows three locations that were analyzed in Particle 212-RS05. Figure 7-34 shows the spectra for the two high-Z features in the buffer layer, 10–20 µm from the kernel, compared to a spectrum from nearby material within the kernel. The ruthenium peak for the *high-Z buffer features* was relatively higher than that seen in EDS spectra of features elsewhere in the layers. This may provide insight into the limited ruthenium presence in the *Pd-complex* and *U-complex features observed in the* IPyC and SiC layers. The presence of silicon in one of the *high-Z buffer features* suggests silicide diffusion toward the kernel.

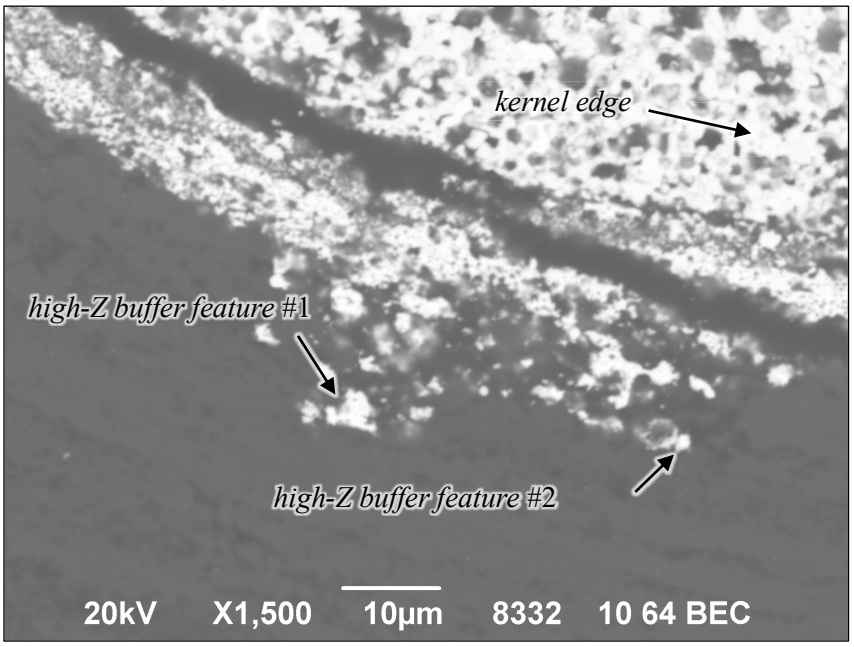

Figure 7-33. Example of *high-Z buffer features* in Particle 212-RS05.

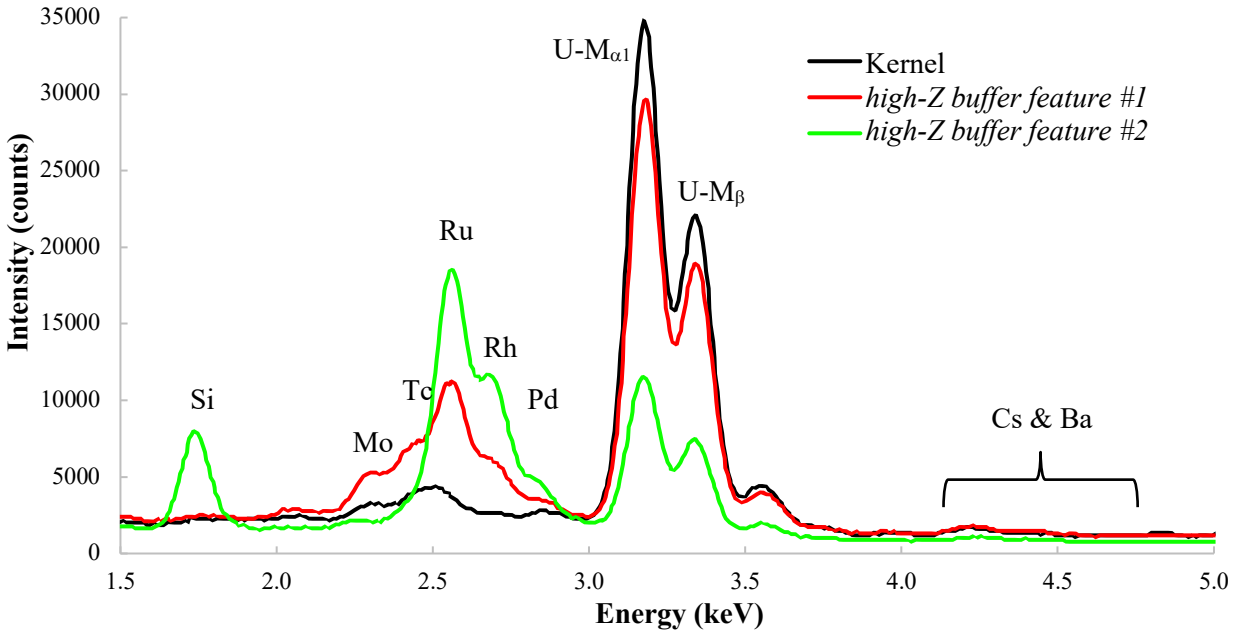

Figure 7-34. EDS spectra from the *high-Z buffer features* labeled in Figure 7-33.

7.4 X-RAY TOMOGRAPHY AND OPTICAL IMAGING OF FAILED-SIC PARTICLE

Particle 212-SP01 was the one particle found with the IMGA that had significant preferential release of cesium (Section 5.1, Figure 5-5). Six-hour gamma counting of Particle 212-SP01 determined that it had a residual ^{134}Cs inventory that was 18% of the average calculated ^{134}Cs inventory in one particle (Section 5.2, Table 5-1). This was sufficient to account for the ^{134}Cs released midway through the 1,800°C safety test of Compact 2-1-2 (Figure 3-1, Table 3-1), suggesting that the observed release was from this single particle. Particle 212-SP01 also released cerium and europium (Table 6-1). Particle 212-SP01 was subjected to XCT for nondestructive three-dimensional (3D) examination of its internal microstructure. Figure 7-35 shows two orthogonal tomograms through the center of Particle 212-SP01. These tomograms are oriented such that the rotation axis is aligned in the vertical direction and the image planes are relative to the orientation in which the particle was loaded on the tomograph stage. Figure 7-36 shows another tomogram through the center of the particle oriented at an oblique angle to the tomograph coordinate system. The orientation of this tomogram was selected to optimize the view of the through-layer SiC degradation. The XCT imaging confirmed that the OPyC layer was intact as expected from the low release of ^{85}Kr during safety testing, which was only 3% of one particle-equivalent (Figure 3-1). Figure 7-36 shows a darker contrast sector in the SiC spanning the layer and one that only partially spans the layer. The darker contrast indicates lower atomic density. The brighter contrast material in the IPyC that appears in the x-ray image to be piled up where the IPyC/SiC boundary would be indicates that the darker contrast in the degraded SiC region was not a void, but rather it was filled with low-Z material. There is evidence in the x-ray image that some of the kernel was consumed, and the missing material appears to be oriented toward the large region of degraded SiC. There was also much more high-Z material distributed throughout the buffer and piled up at the IPyC interface than was observed in the normal particles shown in Figure 6-1 and Figure 6-2.

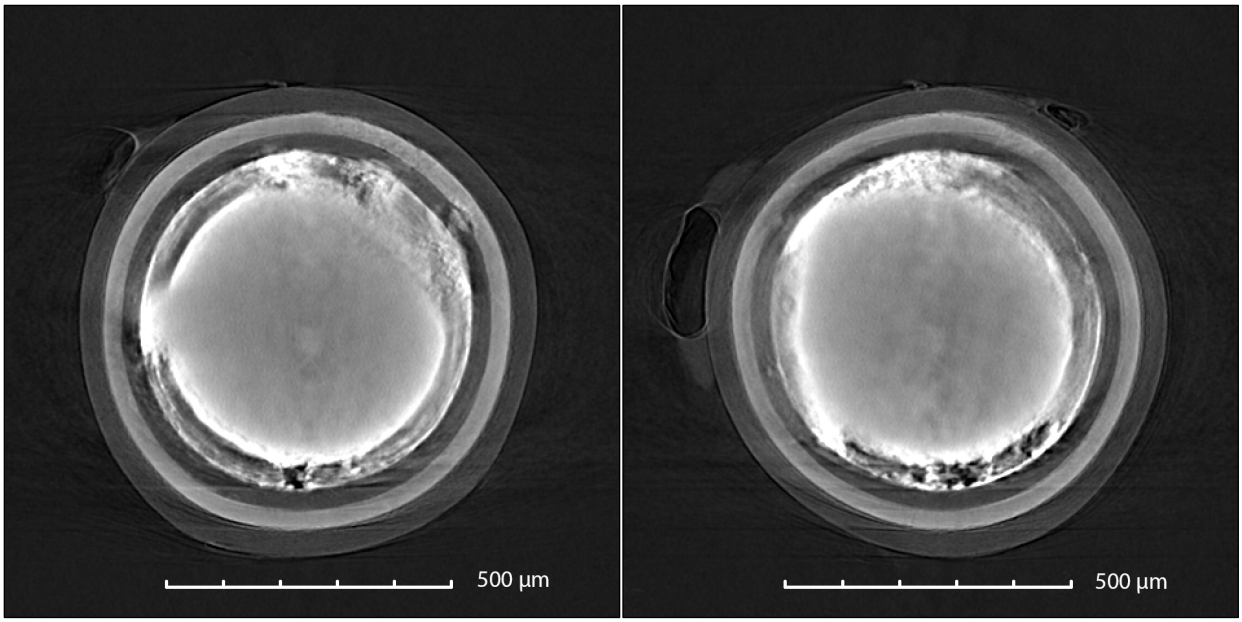

Figure 7-35. Orthogonal tomograms through the center of Particle 212-SP01.

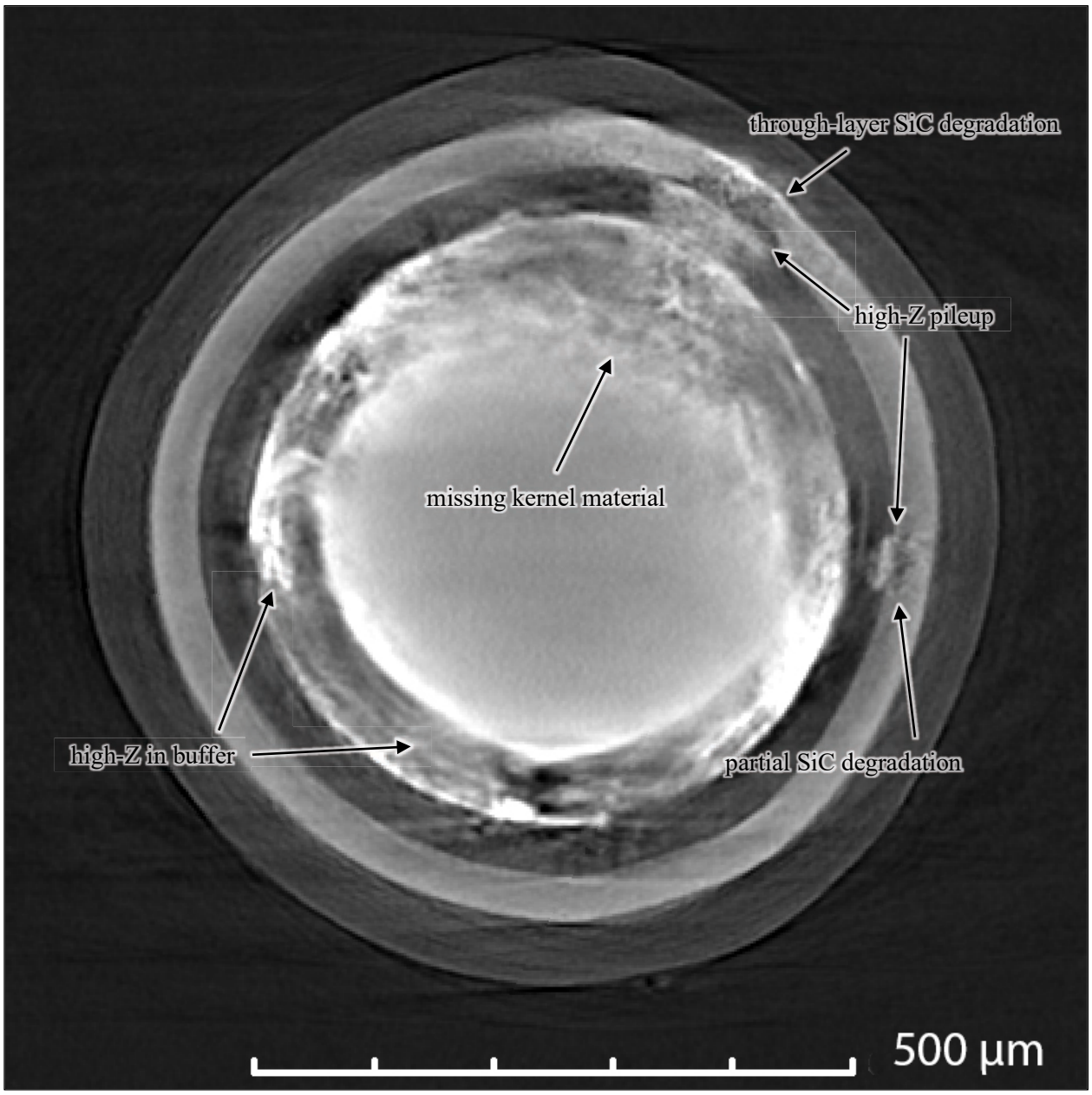

Figure 7-36. X-ray tomogram through the center of Particle 212-SP01 oriented to best view the SiC failure.

The 3D XCT data were used to determine the optimum particle orientation for mounting and planar grinding to reveal the SiC degradation. Because the particle had two sites of particular interest, two parallel target planes were selected. The particle was imaged after polishing to reveal each targeted plane. Figure 7-37 shows the first polished cross section where both SiC degradation features were visible. At this target point, the particle was not at midplane, so the layers appear thicker than actual and the kernel is not fully revealed. Figure 7-38 and Figure 7-39 are higher magnification optical micrographs. Pitting of the inside surface of the SiC was evident around each degradation site. The degradation sites were filled with a material that was optically different from the SiC and pyrocarbon layers. Some of this material crumbled away during sample preparation, so the void space seen in the images between the unknown material and the SiC is probably an artifact. Material with a similar appearance was visible in the IPyC and the OPyC on either side of the through-layer degradation site (Figure 7-38) and in the IPyC adjacent to the smaller degradation site (Figure 7-39). The wide circumferential crack in the SiC was found to contain high-Z material, so it occurred during safety testing. Imaging of these features by SEM is discussed in Section 7.5 and EDS analysis of the high-Z inclusions is provided in Section 7.6.

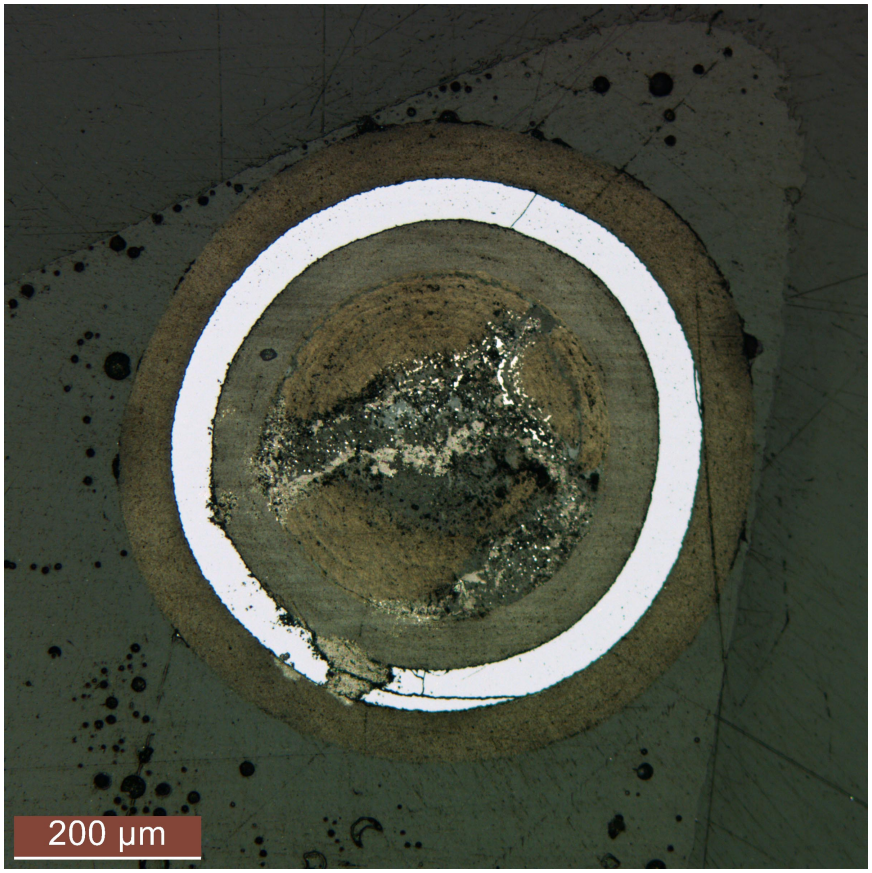

Figure 7-37. First polished cross section of Particle 212-SP01 showing SiC degradation.

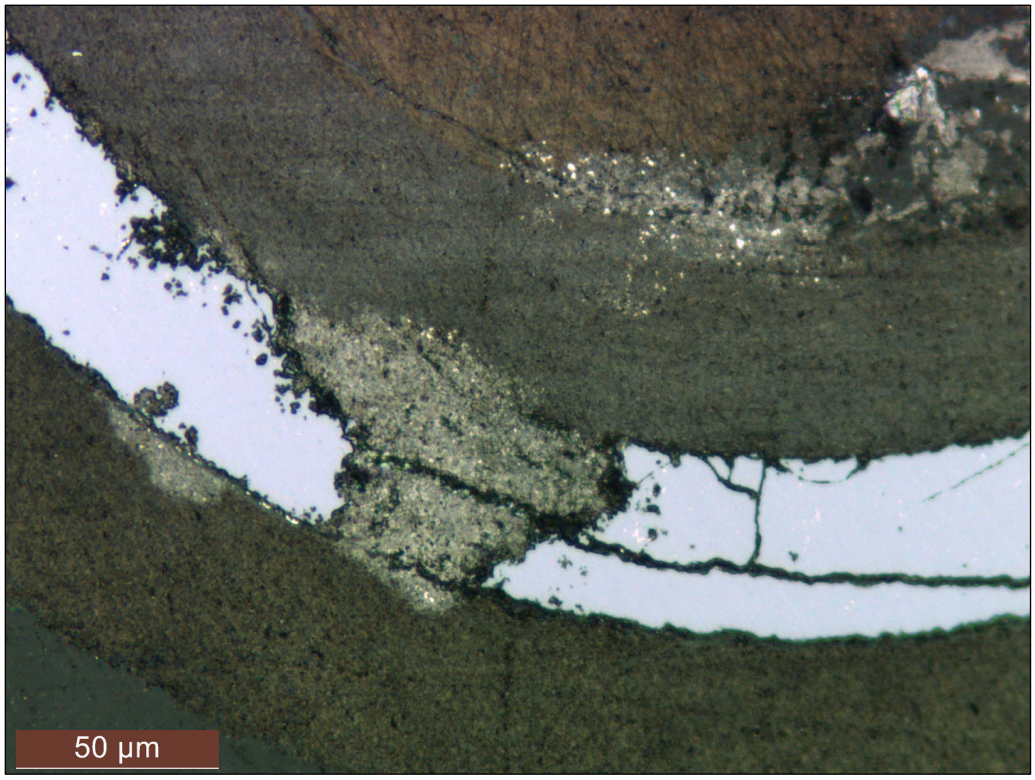

Figure 7-38. First polished cross section of Particle 212-SP01 showing the through-layer SiC degradation feature.

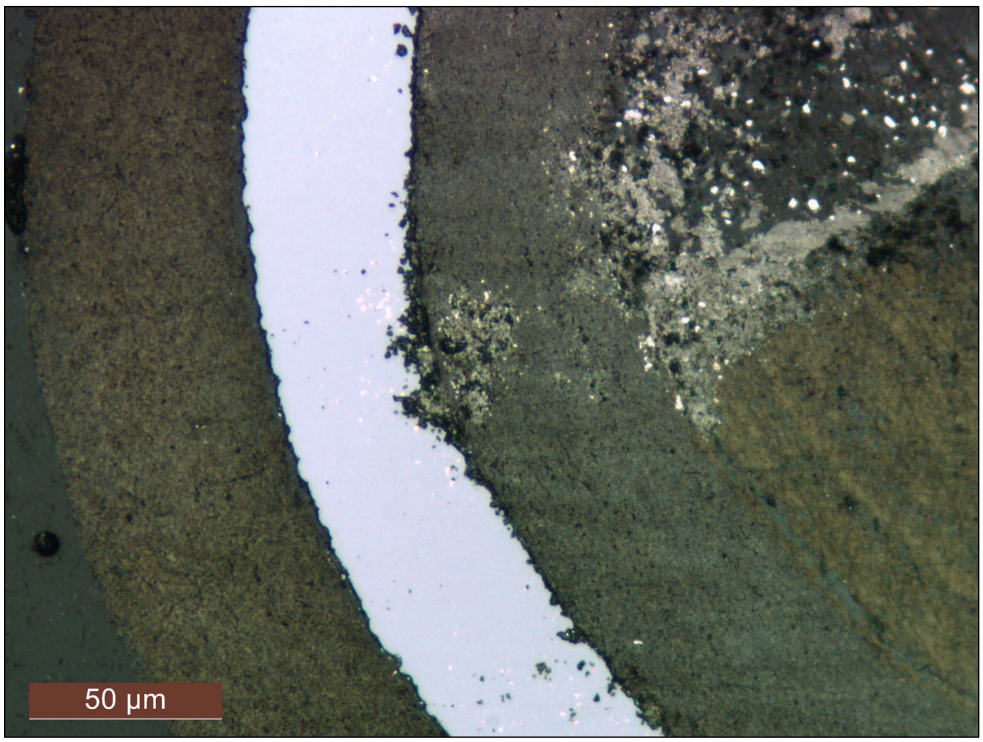

Figure 7-39. First polished cross section of Particle 212-SP01 showing the partial SiC degradation feature.

The second plane of interest was where there were several SiC cracks, as well as an IPyC crack that was filled with high-Z material and aligned with a SiC crack. Figure 7-40 is an oblique tomogram showing the target plane and Figure 7-41 shows the polished cross section, which shows the cracks in the SiC layer. Figure 7-42 and Figure 7-43 show two SiC cracks that are aligned with faint cracks in the IPyC layer. Figure 7-44 shows a sector of the buffer layer where the layer was fractured. These features were imaged further by SEM (Section 7.5) and EDS was used to examine the fission products and actinides around each feature (Section 7.6).

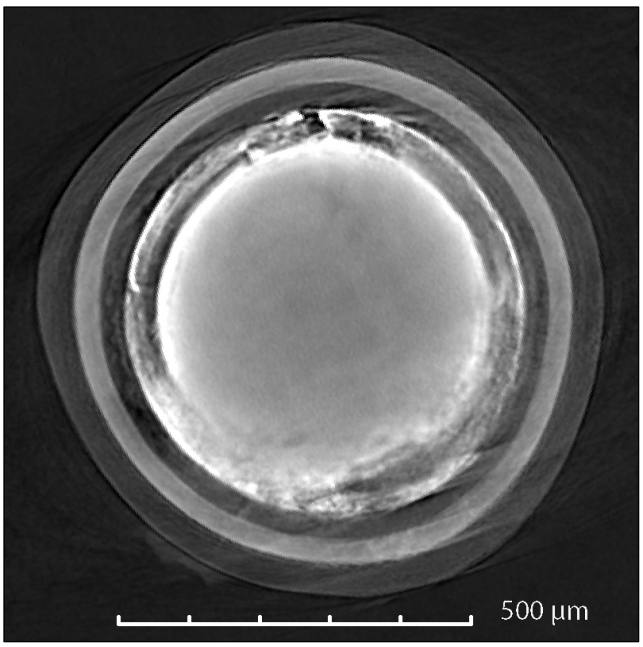

Figure 7-40. X-ray target plane for second polish where a crack filled with high-Z material was visible.

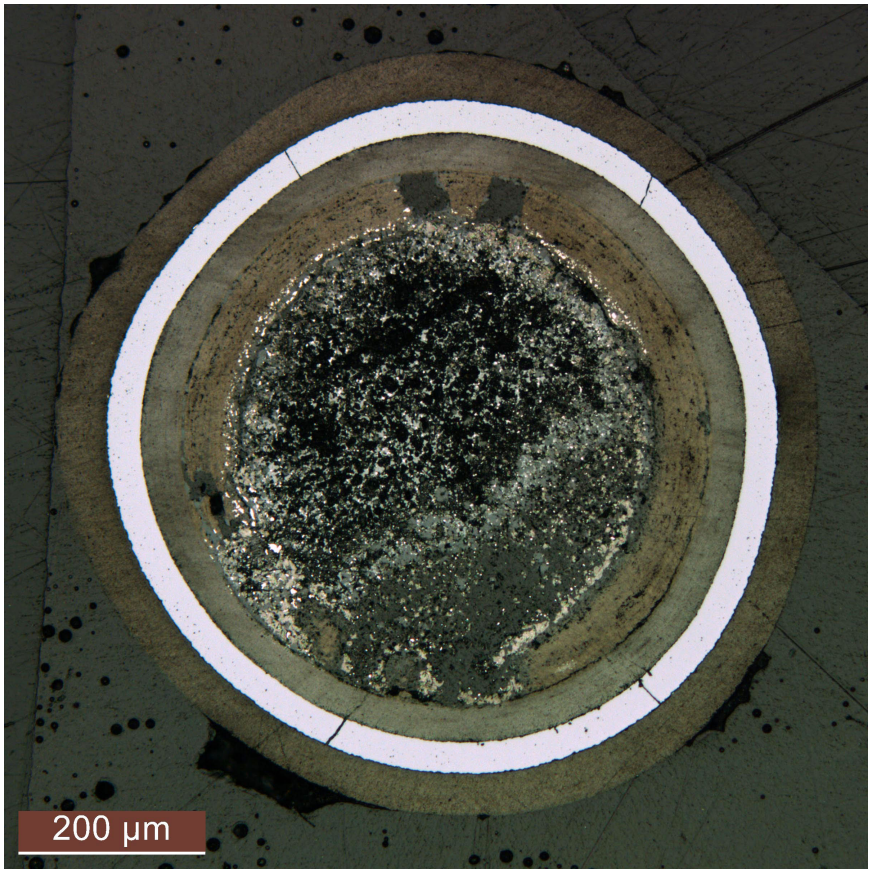

Figure 7-41. Second polished cross section of Particle 212-SP01 showing cracks in the IPyC and the SiC.

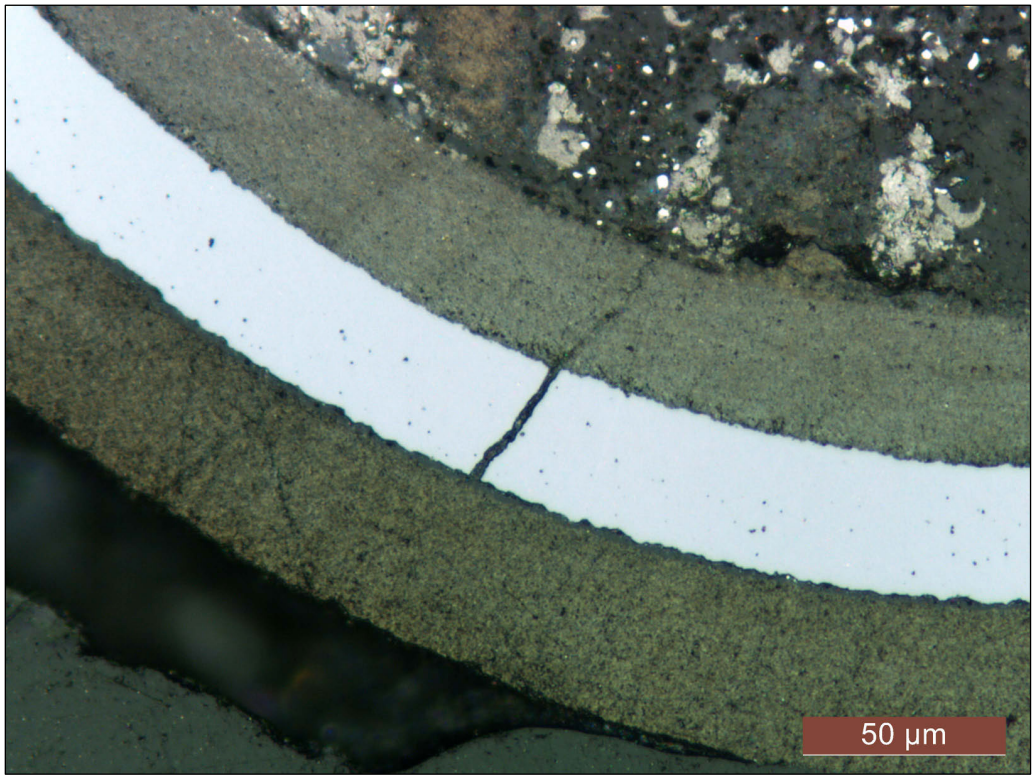

Figure 7-42. Second polished cross section of Particle 212-SP01 showing a crack through the IPyC layer that was aligned with a wide crack through the SiC layer.

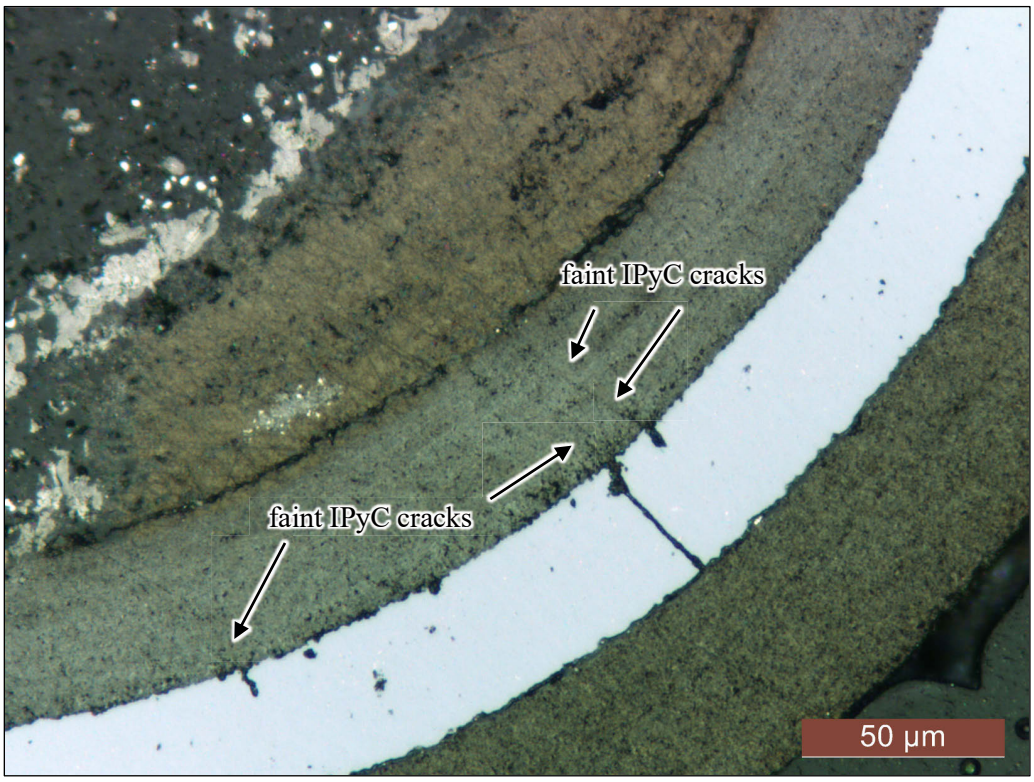

Figure 7-43. Second polished cross section of Particle 212-SP01 showing faint cracks through the IPyC layer aligned with degraded areas and a crack in the SiC layer.

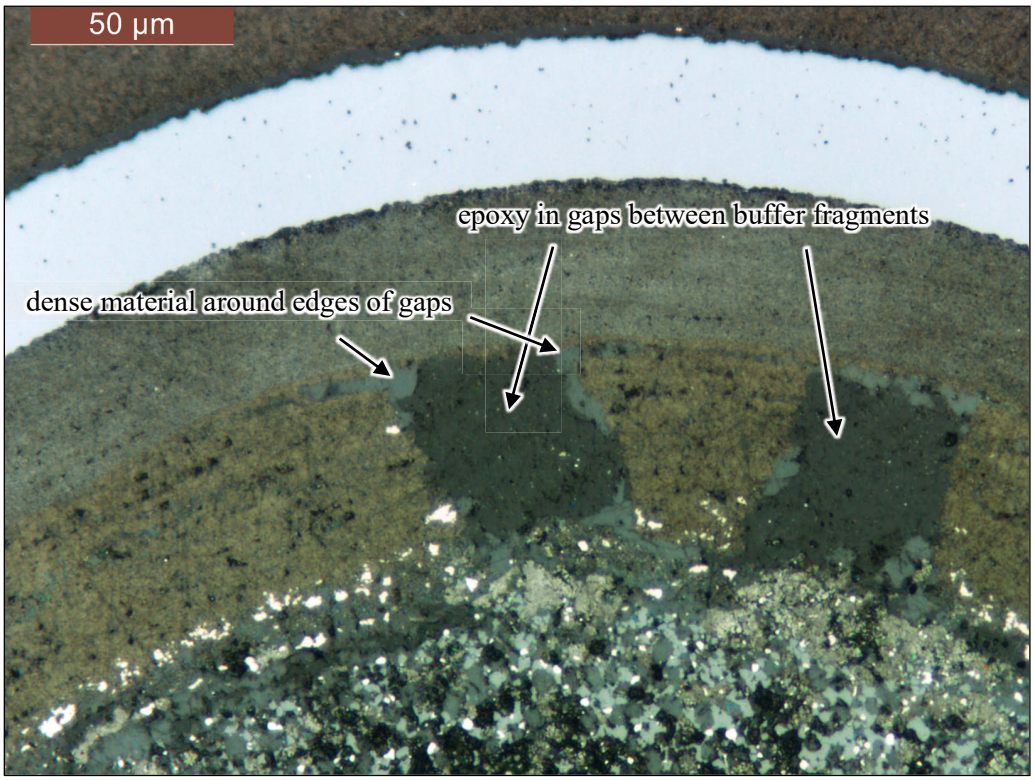

Figure 7-44. Second polished cross section of Particle 212-SP01 showing two gaps in the buffer that were filled with epoxy during vacuum back-potting.

7.5 SEM IMAGING OF FAILED-SIC PARTICLE

Particle 212-SP01 was analyzed at two different polished cross sections. The first cross section contained the SiC failure site. Figure 7-45 and Figure 7-46 show the large through-layer SiC degradation feature that was identified by XCT. Numerous clusters of high-Z material can be seen in the center of the feature, with low-Z material around the edges. The through-layer SiC degradation appeared to be centered on a crack in the IPyC layer, which was also filled with high-Z material. The IPyC crack may have facilitated transport of actinides and fission products to the SiC layer, resulting in the observed SiC degradation. The location of the IPyC crack at the buffer interface coincided with a location where the buffer was attached on one side and missing on the other. These observations are consistent with the predominate failure mechanism for AGR 1 TRISO fuel, where incomplete buffer detachment caused IPyC fracture, which in turn caused enhanced fission product transport to the SiC, resulting in SiC degradation (Hunn et al. 2014). Figure 7-45 shows a large circumferential crack in the SiC leading away from the degradation site. High-Z material in this crack indicates it is not an artifact of the grinding and polishing. There was also high-Z material in the OPyC layer adjacent to the through-layer SiC degradation, which did not appear to have penetrated through the OPyC to the TRISO particle surface.

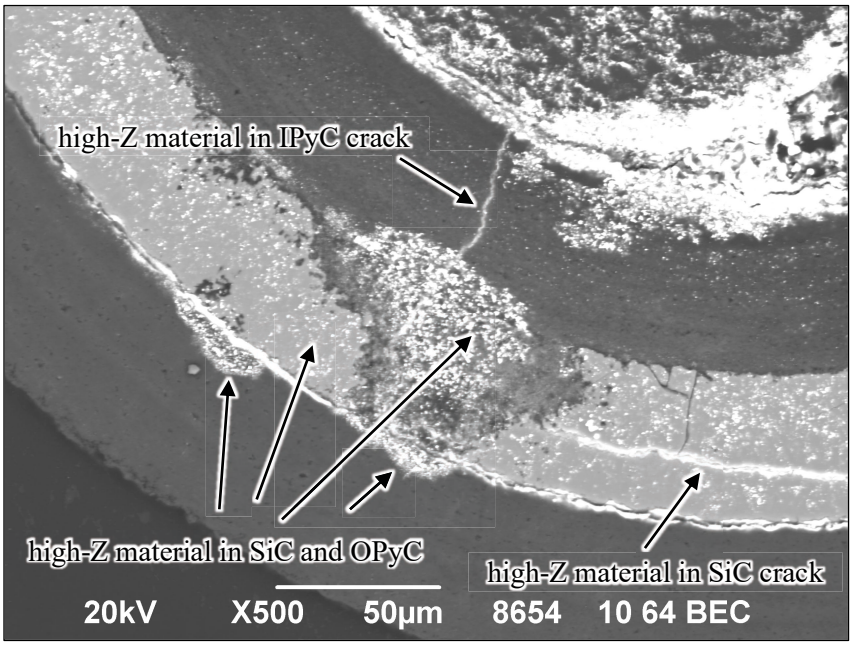

Figure 7-45. BEC image of Particle 212-SP01 showing through-layer SiC degradation.

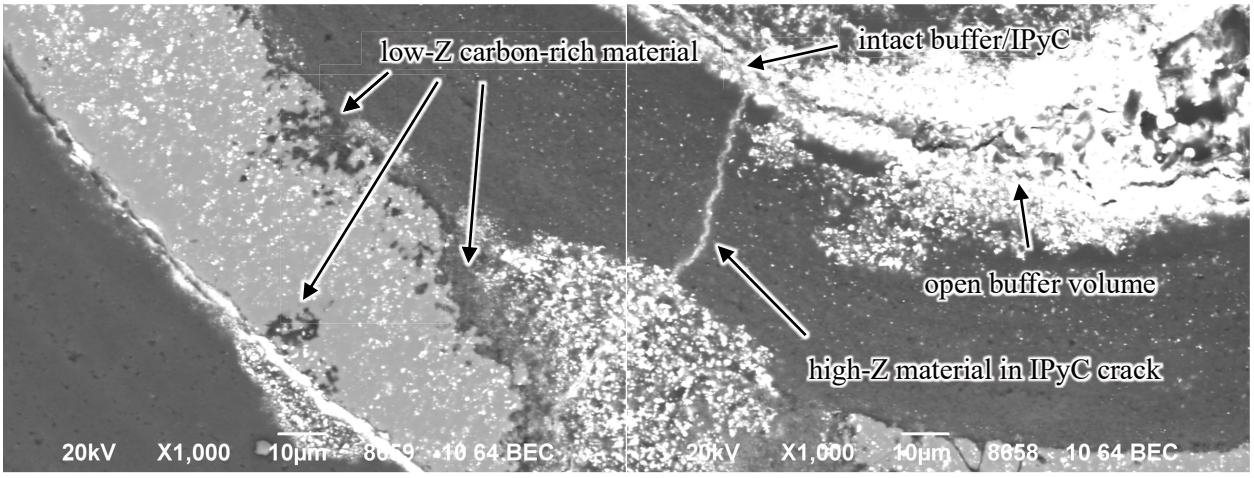

Figure 7-46. BEC images of Particle 212-SP01 showing area around the through-layer SiC degradation site.

Figure 7-47 shows the partial SiC degradation feature. This feature was not associated with an obvious IPyC crack. However, significant high-Z material was clustered in the IPyC adjacent to the degradation and this was also a sector where the buffer had fractured. The buffer fracture apparently allowed more material from the kernel to enter the IPyC and SiC. There was a significant amount of high-Z material embedded throughout the SiC layer in this region.

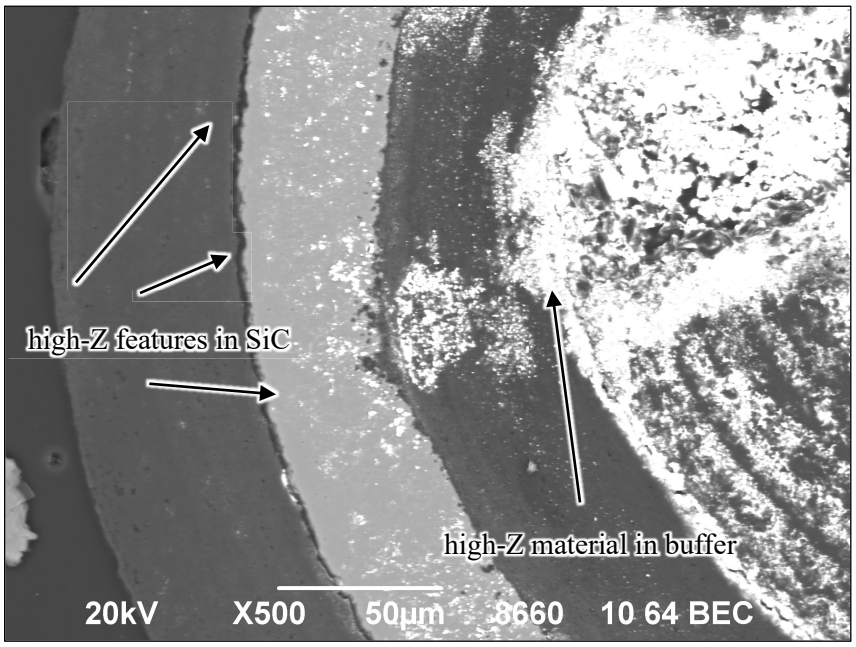

Figure 7-47. BEC image of Particle 212-SP01 showing the partial SiC degradation site and a high concentration of high-Z material in the buffer, IPyC, and SiC layers in this region.

Figure 7-48 presents an overview of the second cross section through Particle 212-SP01, and higher magnification images of various regions of interest are shown in Figure 7-49 through Figure 7-54. Figure 7-36 shows that the low density region of the fuel kernel visible in Figure 7-48 was oriented toward the through-layer SiC degradation visible in Figure 7-45.

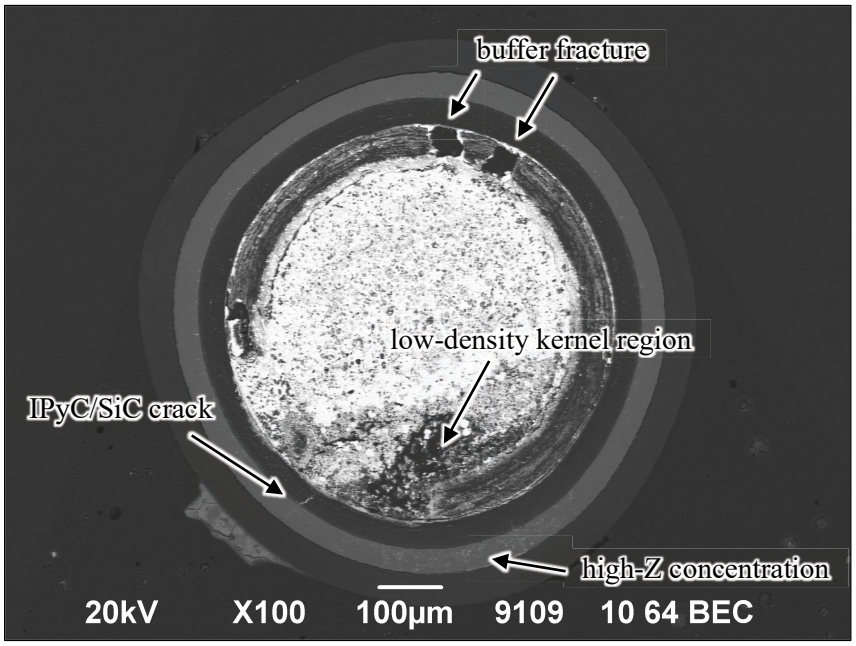

Figure 7-48. Overview BEC image of Particle 212-SP01 in second plane showing low-density region in kernel.

Figure 7-49 shows the presence of *high-Z IPyC features*, *high-Z interface features*, *high-Z SiC features*, and *low-Z SiC features* that appear similar to those found in the RS-series particles (Section 7.2). *High-Z boundary features* were less prevalent in Particle 212-SP01 than in the RS-series particles. Figure 7-48 shows that the microstructure in Figure 7-49 was common to most of the observed cross section, except for the sector of the SiC layer adjacent to the low-density kernel region, which had a higher density of *high-Z SiC features*. This region is shown at higher magnification in Figure 7-50. In addition to the high concentration of high-Z features in the SiC, there were also low-Z regions in the SiC near the IPyC/SiC boundary where localized SiC degradation had occurred.

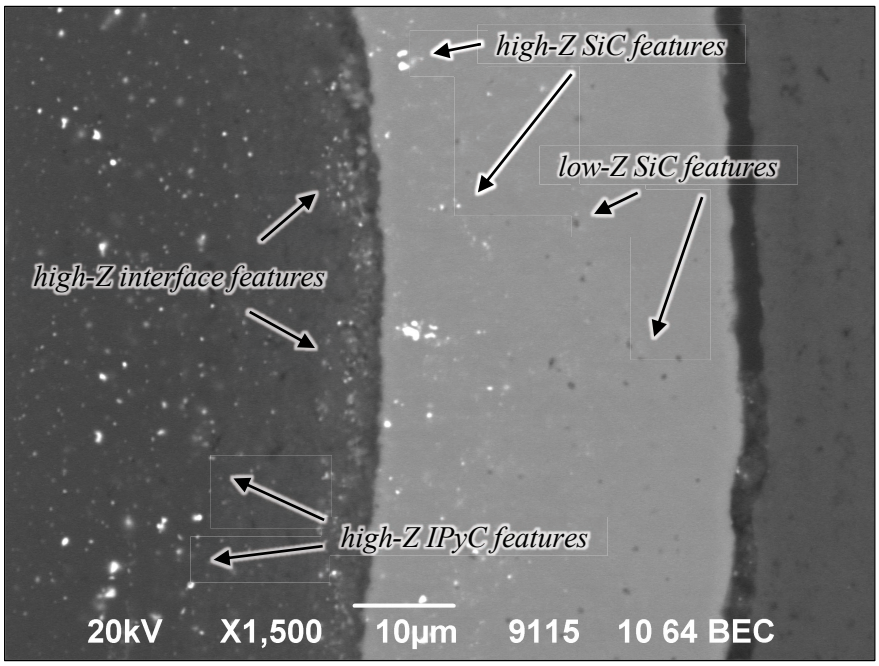

Figure 7-49. BEC image of Particle 212-SP01 in second plane showing high-Z features in the IPyC and the SiC.

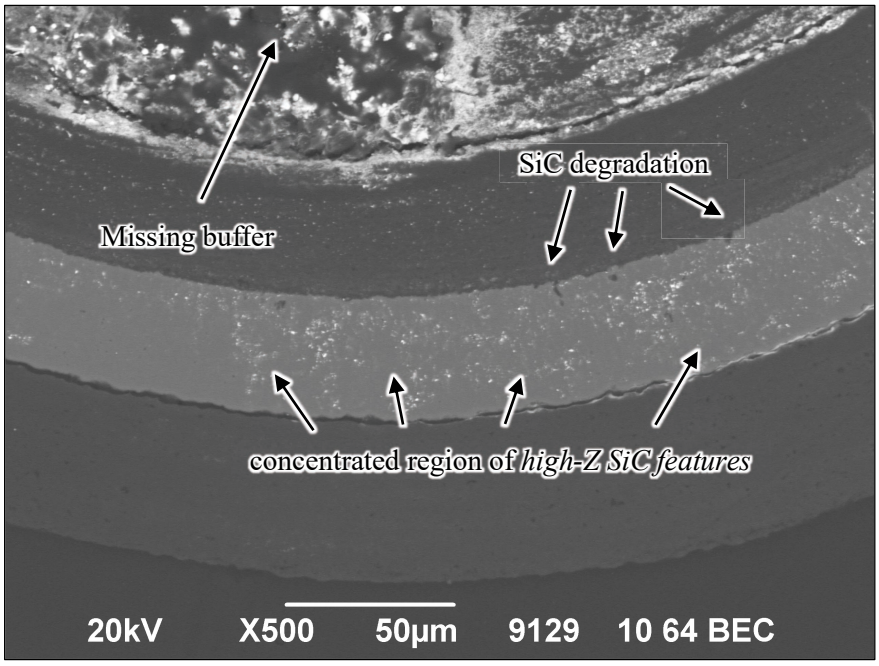

Figure 7-50. BEC image of Particle 212-SP01 in second plane showing localized SiC degradation.

Dense clusters of high-Z material can be seen at the edges of the fractured buffer and at the buffer/IPyC interface in Figure 7-51. Most of the gaps between the buffer fragments were filled with epoxy that was injected into these regions by vacuum infiltration after grinding had exposed the buffer gaps. The x-ray tomogram in Figure 7-40 shows that these buffer gaps were originally empty. A few diffuse high-Z regions were observed in the buffer of Particle 212-SP01 (Figure 7-52) that were different from the denser high-Z features observed in the buffer of the RS-series particles. The high-Z features located in these regions of the Particle 212-SP01 buffer were analyzed with EDS and are discussed in Section 7.6.

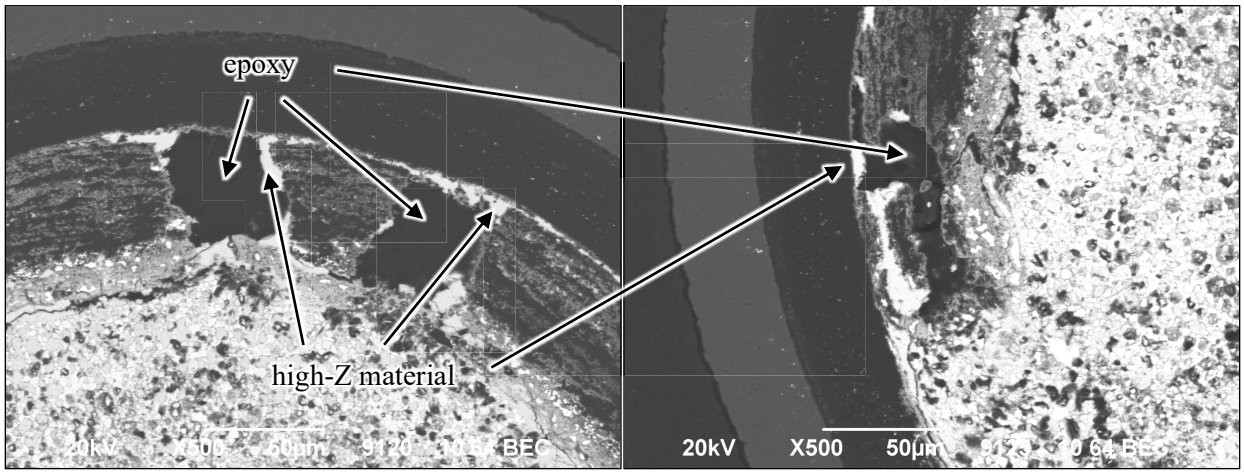

Figure 7-51. BEC images of Particle 212-SP01 in second plane showing high-Z material associated with the fractured buffer layer.

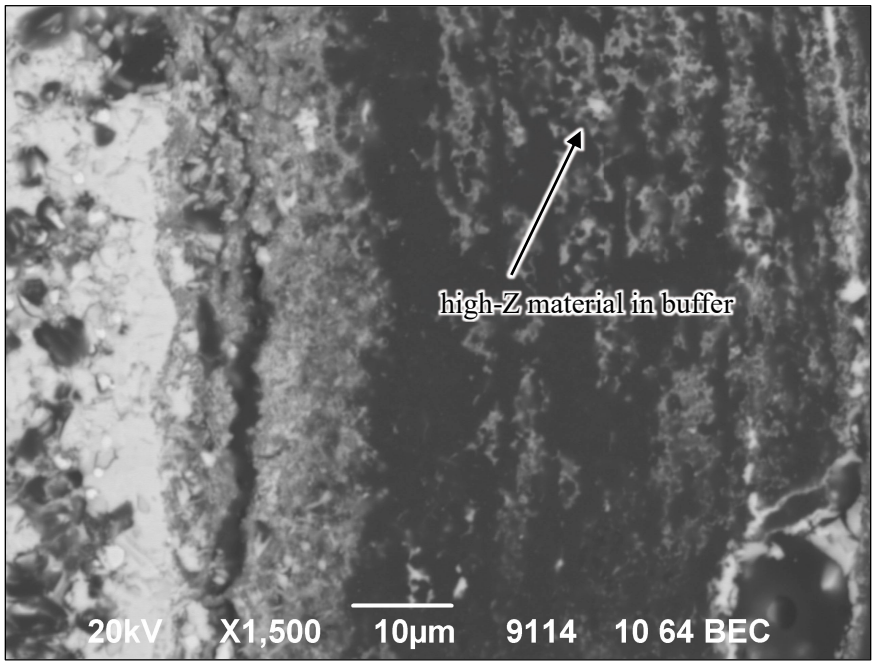

Figure 7-52. BEC image of Particle 212-SP01 in second plane showing diffuse high-Z material in the buffer.

Figure 7-53 shows the same crack through the IPyC and the SiC that is shown in the optical micrograph in Figure 7-42, and Figure 7-54 shows the crack that is shown in Figure 7-43. In both cases, the cracks spanned the IPyC layer. This was not evident in the SEM micrographs but could be seen in the x-ray tomography and optical microscopy images. The IPyC cracks were aligned to the SiC cracks, which extended across the SiC layer and terminated at the gap between the SiC and the OPyC. The IPyC cracks were filled with high-Z material, which indicates that these features were not artifacts caused by the

grinding and polishing processes. Figure 7-54 shows that one of the SiC cracks included a low-Z region along the crack that indicates degradation. The SiC crack shown in Figure 7-54 also had some high-Z material embedded in the crack near the OPyC interface. These two observations of co-located features in the SiC crack provide further evidence that the crack occurred during safety testing.

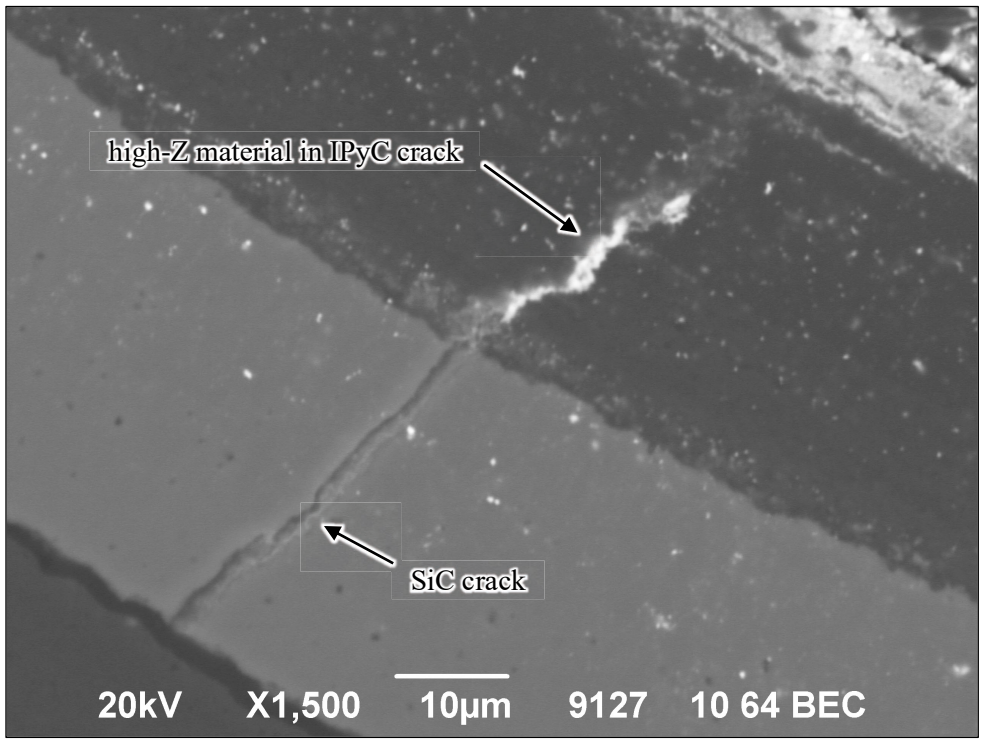

Figure 7-53. BEC image of Particle 212-SP01 in second plane showing one of the connected IPyC/SiC cracks.

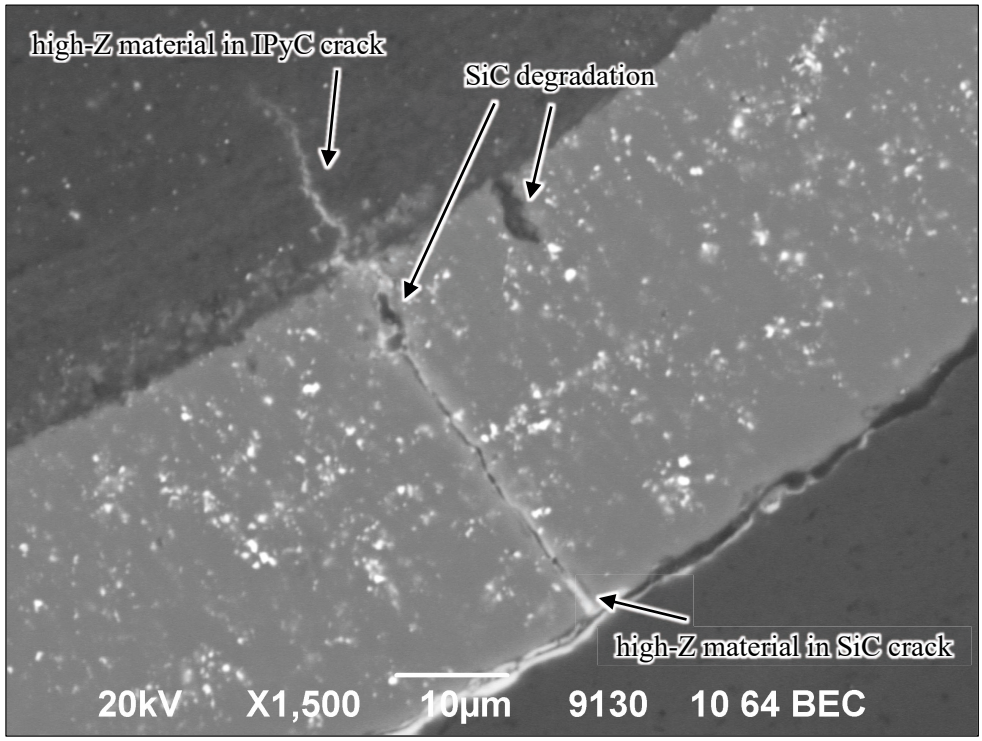

Figure 7-54. BEC image of Particle 212-SP01 in second plane showing another connected IPyC/SiC crack.

7.6 ELEMENTAL ANALYSIS OF FAILED-SIC PARTICLE

Figure 7-55 presents a series of EDS maps of the region around the through-layer SiC degradation feature in Particle 212-SP01. The silicon and carbon maps show that the degraded areas in the SiC were depleted of silicon and rich in carbon. There were lower-intensity silicon-containing regions in the OPyC, at the buffer/IPyC interface, and in the degradation feature itself. These regions corresponded to similar regions in the EDS maps for uranium, ruthenium, rhodium, palladium, and technetium, suggesting these high-Z metals reacted with the SiC to form silicides, and some of these silicides migrated into the OPyC and to the buffer/IPyC interface. These silicides were similar to those present in the complex features observed in the RS-series particles and discussed in Section 7.3. However, the predominant high-Z species were ruthenium, uranium, and rhodium, while palladium was only present as a minor constituent. Molybdenum was observed in conjunction with uranium and technetium at the SiC/OPyC interface, in the broad circumferential SiC crack, and in the buffer region.

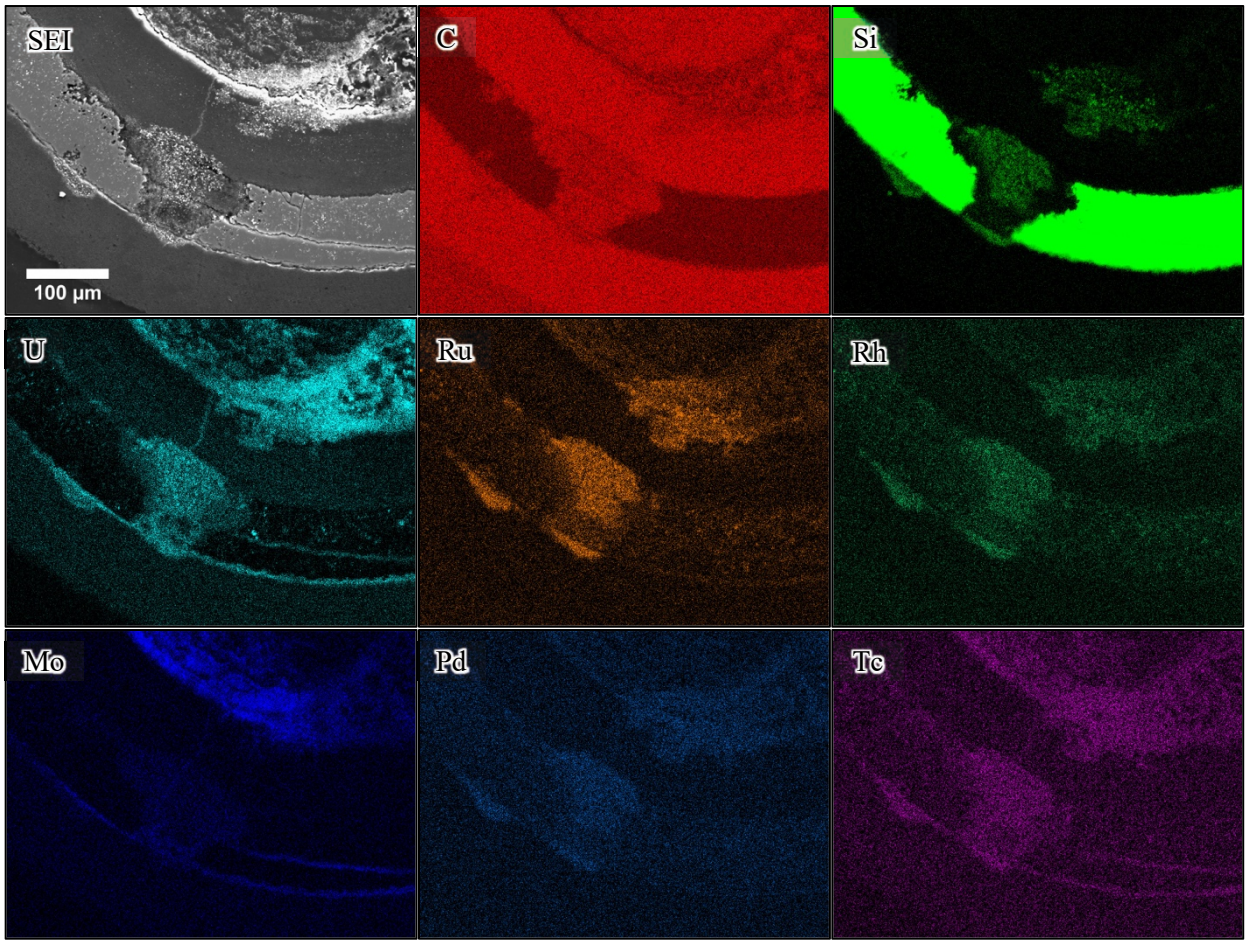

Figure 7-55. EDS map showing the distribution of carbon, silicon, uranium, and select fission products in the TRISO layers surrounding the through-layer SiC degradation feature; the color intensity reflects the relative counts above background for each element.

Point-ID analyses were performed on multiple locations around the through-layer SiC degradation feature to highlight both major and minor constituents present in the feature and in the adjacent areas. Figure 7-56 shows four representative areas that were analyzed and their corresponding spectra are provided in Figure 7-57. The spectra show Point-ID compositions that were consistent with the EDS maps in Figure 7-55. The high-Z material inside the through-layer SiC degradation feature, in the OPyC adjacent to the feature, and in the surrounding undegraded SiC showed similar compositions when analyzed by EDS. The high-Z elements were predominantly ruthenium, uranium, and rhodium, with minor concentrations of palladium,

technetium, and molybdenum. There were also significant x-rays from silicon, carbon, and oxygen in these regions. The high-Z elements in the gap between the SiC and the OPyC were primarily uranium, molybdenum, and plutonium. Aluminum was also observed in this region of the SiC/OPyC gap, but it probably came from the aluminum sample holder in which particles were mounted for grinding. This introduces the possible false conclusion that the high-Z elements in the SiC/OPyC gap with the aluminum were also grinding debris transferred from elsewhere in the particle, such as from the kernel. However, the x-ray images confirm the presence of high-Z material in this portion of the gap between the SiC and the OPyC prior to cross sectioning. In addition, aluminum was observed in other locations around the SiC/OPyC gap away from the high-Z material.

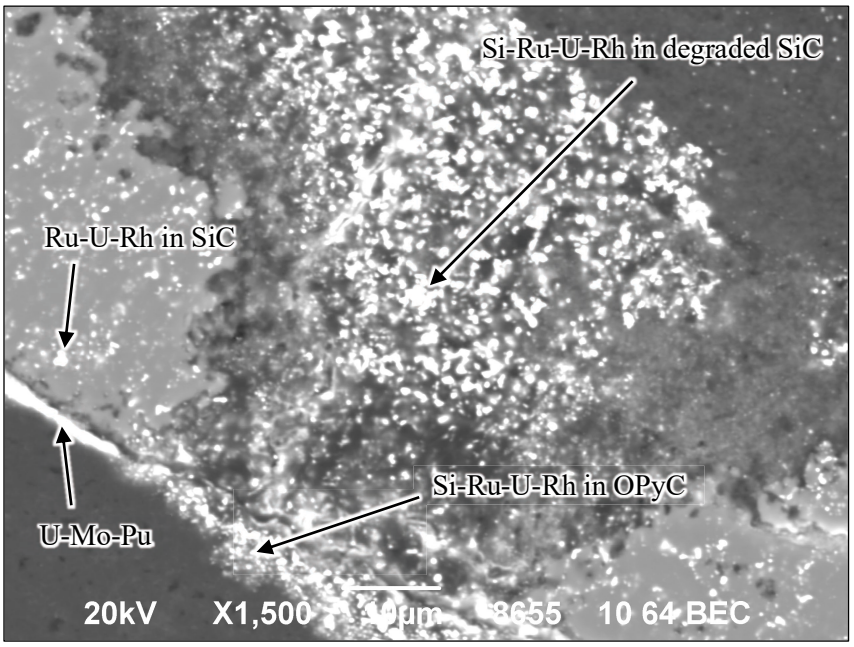

Figure 7-56. Examples of varied chemical compositions in and around the through-layer SiC degradation feature in Particle 212-SP01.

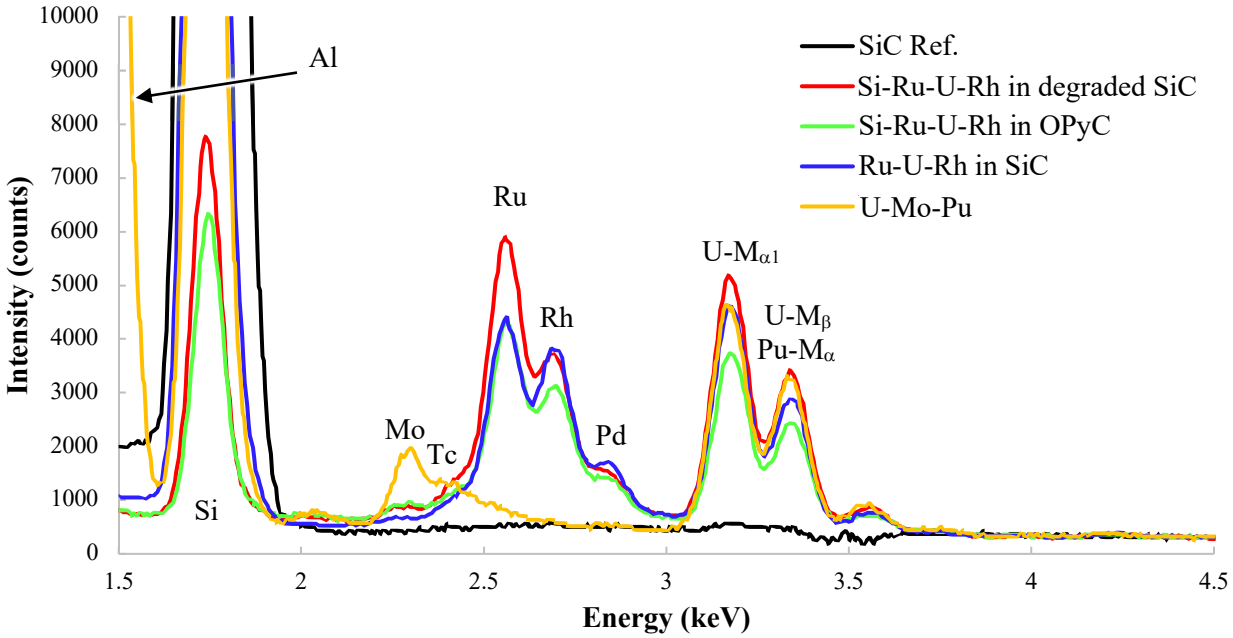

Figure 7-57. EDS spectra from locations labeled in Figure 7-56.

Figure 7-58 shows the IPyC crack that was associated with the through-layer SiC degradation feature. Three Point-ID locations are labeled in this figure and the corresponding spectra are shown in Figure 7-59. The region shown in Figure 7-58 is also shown in the optical micrograph in Figure 7-38. In Figure 7-58, there was buffer at the buffer/IPyC interface adjacent to the left of the IPyC crack, while the buffer was missing to the right of the IPyC crack and dense material was filling its place. There was a lot of high-Z material that appeared to have migrated into the IPyC from the dense material at the buffer/IPyC interface. Point-ID analysis of this high-Z material at the location close to the IPyC crack shown in Figure 7-58 yielded relatively high x-ray peaks from silicon, ruthenium, uranium, and rhodium, with minor peaks from technetium, palladium, and molybdenum. This was essentially the same composition observed in the high-Z material in the center of the degraded SiC. The high-Z material in the IPyC crack generally had the same make up. However, some locations in the IPyC crack, such as that labeled in Figure 7-58, had a different composition that was predominantly uranium and molybdenum, as shown in Figure 7-59.

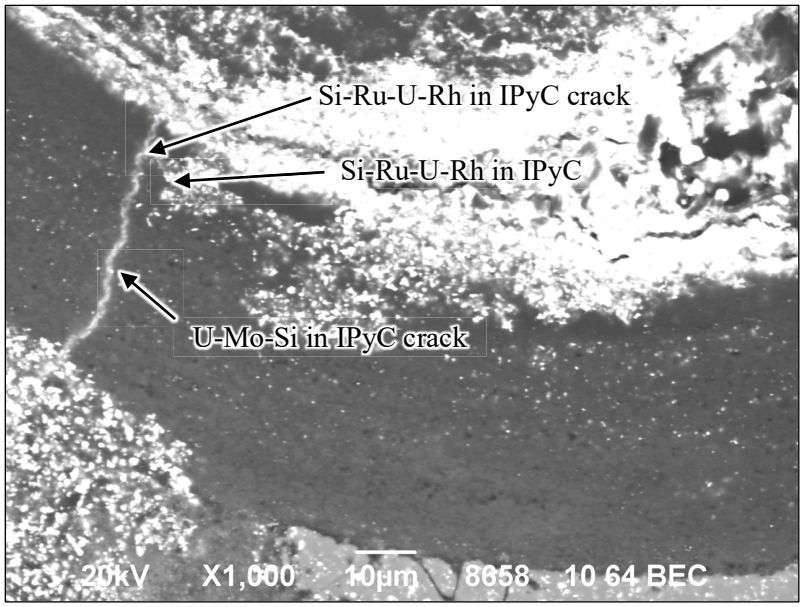

Figure 7-58. BEC image showing the IPyC crack that was associated with the through-layer SiC degradation feature, with labeled locations for the Point-ID spectra shown in Figure 7-59.

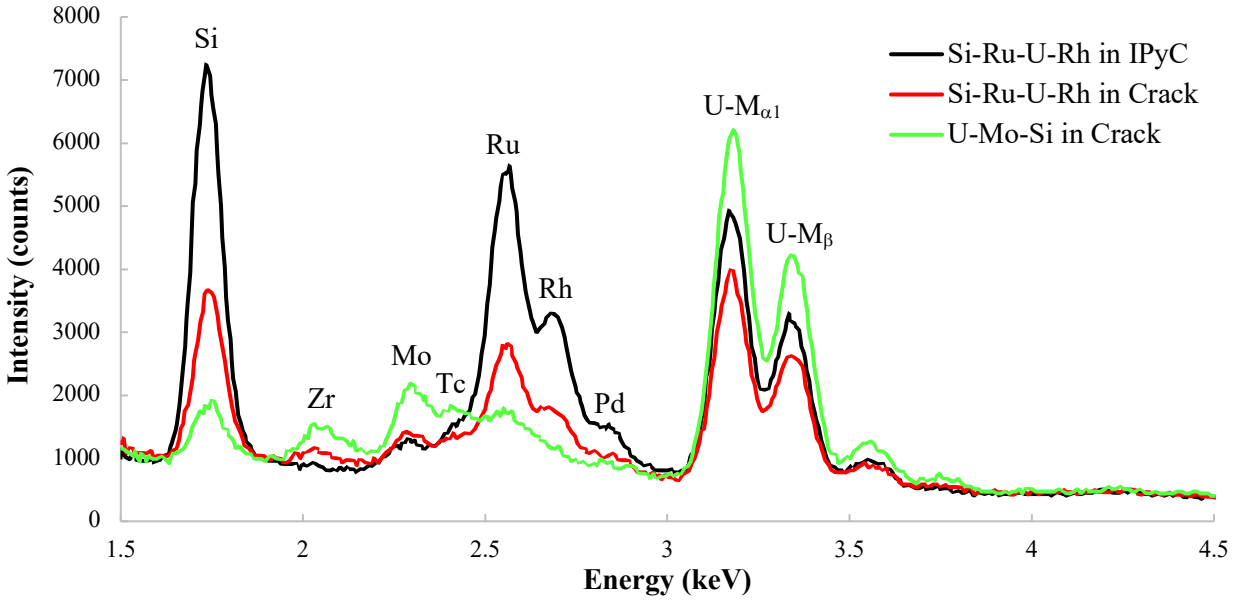

Figure 7-59. EDS spectra from locations labeled in Figure 7-58.

Figure 7-60 shows the partial SiC degradation feature, which is also shown in the optical micrograph in Figure 7-39. Similar to what was observed for the through-layer SiC degradation feature, Figure 7-39 shows that the partial SiC degradation feature was located opposite a region of the buffer/IPyC interface where the buffer was missing and dense material was filling its place. A large concentration of high-Z material was located in the IPyC layer close to the SiC degradation site. A representative Point-ID EDS spectrum of the high-Z material in the IPyC is shown in Figure 7-61. The composition was essentially the same as the material observed in the IPyC near the through-layer SiC degradation feature (Figure 7-59) and in the center of the degraded SiC (Figure 7-57). This shows a commonality in the reactions occurring at these two degradation sites and that the material in the IPyC is a product of the degradation reaction. There was a high density of *high-Z SiC features* surrounding the partial SiC degradation. The two features labeled in Figure 7-60 were *U-rich features* similar to those observed in the RS-series particles.

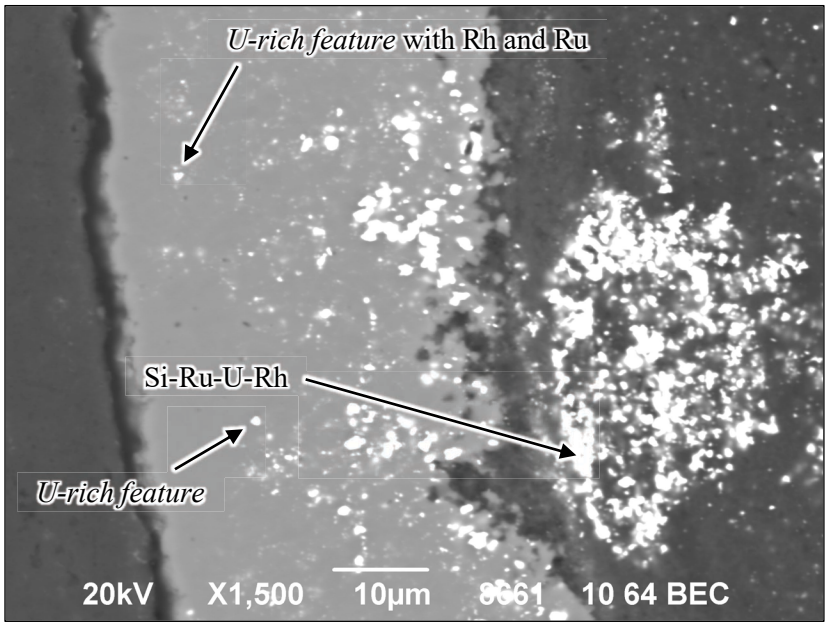

Figure 7-60. BEC image showing the partial SiC degradation site, with labeled locations for the Point-ID spectra shown in Figure 7-61.

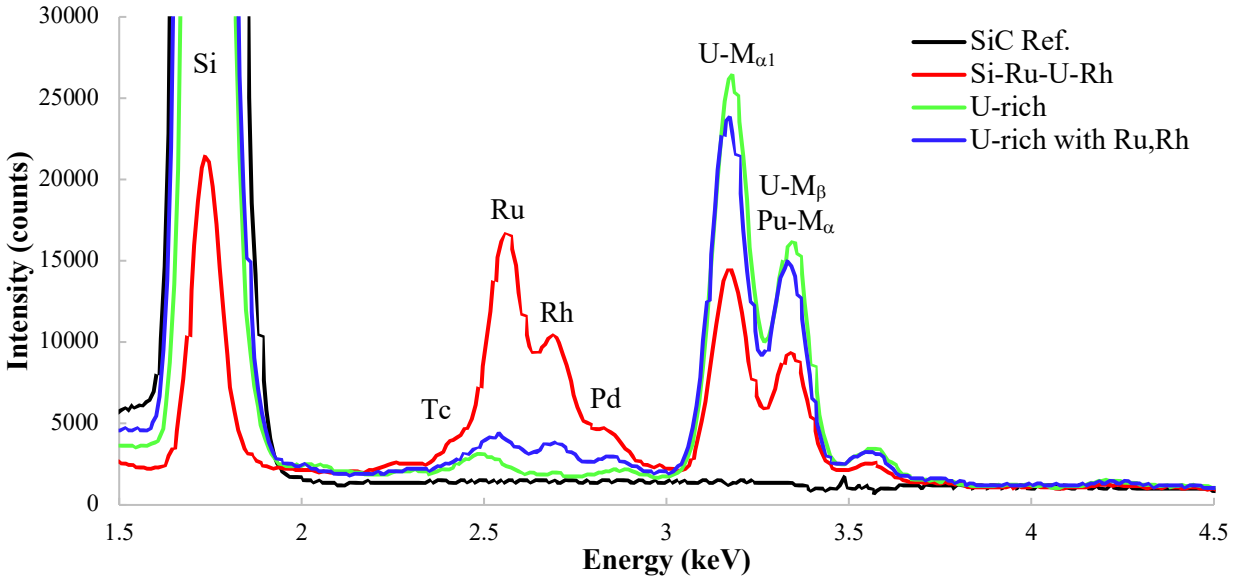

Figure 7-61. Composition of high-Z material near the partial SiC degradation site.

Figure 7-62 shows two regions of the Particle 212-SP01 SiC layer that were visible in the second inspection plane. As discussed in Section 7.5 and shown in Figure 7-48 through Figure 7-50, most of the SiC displayed high-Z features similar to those in the RS-series particles (Figure 7-62b), while there was a higher density of *high-Z SiC features* in the SiC sector near the low-density kernel region (Figure 7-62a), which was about 50 µm from the through-layer SiC degradation feature viewed in the first inspection plane. The *high-Z SiC features* in the SiC sector near the low-density kernel region were either *U-rich features* or complex features that were predominantly ruthenium, uranium, and rhodium, with trace amounts of palladium. An equal number of *U-rich features* and complex features were observed, and about one-third of the *U-rich features* contained molybdenum and/or zirconium. About 75% of the *high-Z SiC features* in the rest of the SiC were *U-rich features* and about 25% were complex features that contained predominantly rhodium and uranium in approximately equal apparent concentrations, with trace amounts of palladium and only a limited presence of ruthenium. Some *U-rich features* included minor amounts of rhodium and palladium. Figure 7-63 shows three representative spectra from the locations identified in Figure 7-62.

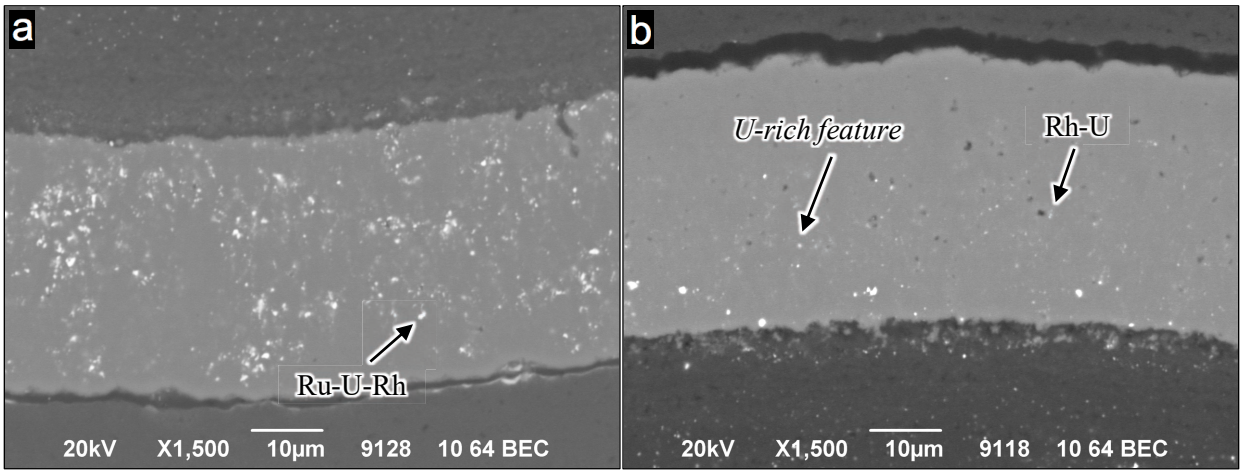

Figure 7-62. BEC images of Particle 212-SP01 in second plane of inspection showing (a) a SiC sector close to the through-layer SiC degradation feature visible in the first inspection plane (Figure 7-45) and (b) a SiC sector on the opposite side of the particle.

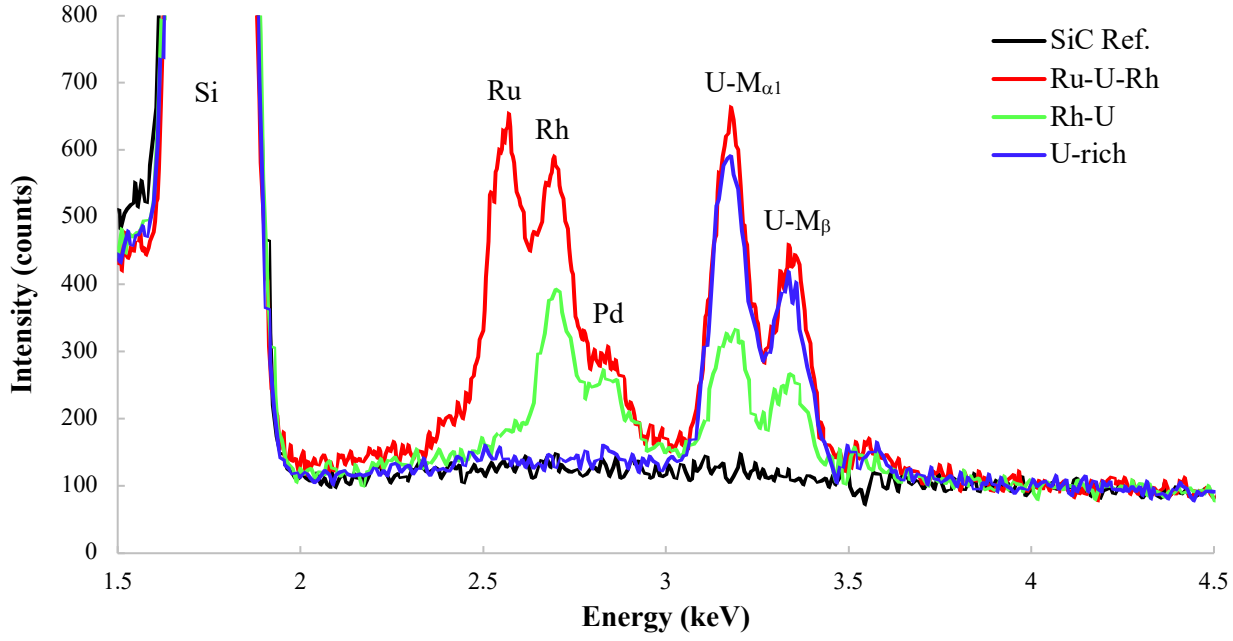

Figure 7-63. EDS spectra from locations labeled in Figure 7-62.

Significant deposits of high-Z material in the region surrounding two epoxy-filled gaps between buffer fragments were identified in Figure 7-51. Figure 7-64 shows an EDS map of uranium, which was the predominant high-Z element in these deposits. Figure 7-65 shows an EDS map of uranium for another area in the buffer that was also shown in BEC mode in Figure 7-52. The map shows that uranium was dispersed throughout the buffer.

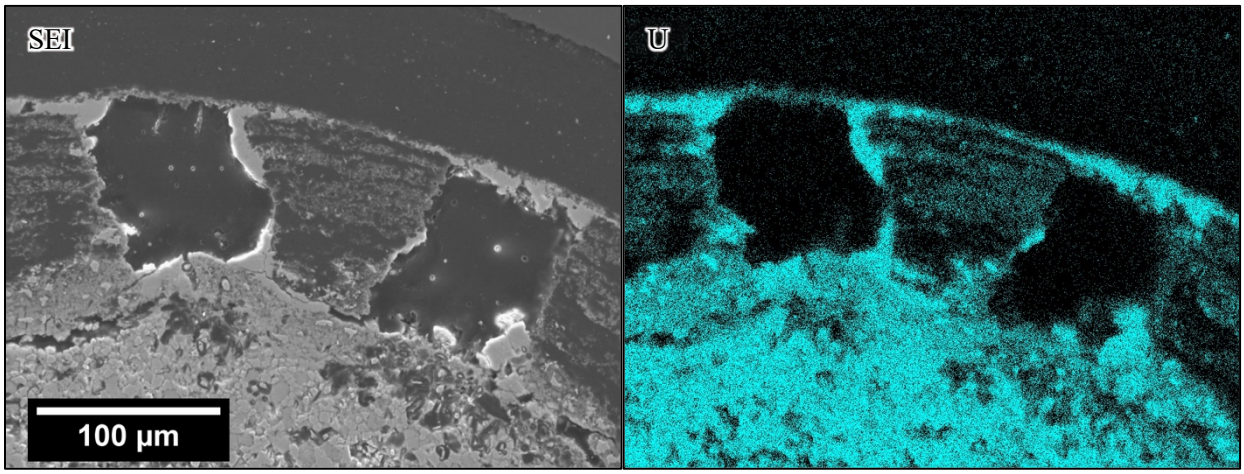

Figure 7-64. SEI image and corresponding EDS map of uranium in a region surrounding two gaps in the buffer layer of Particle 212-SP01.

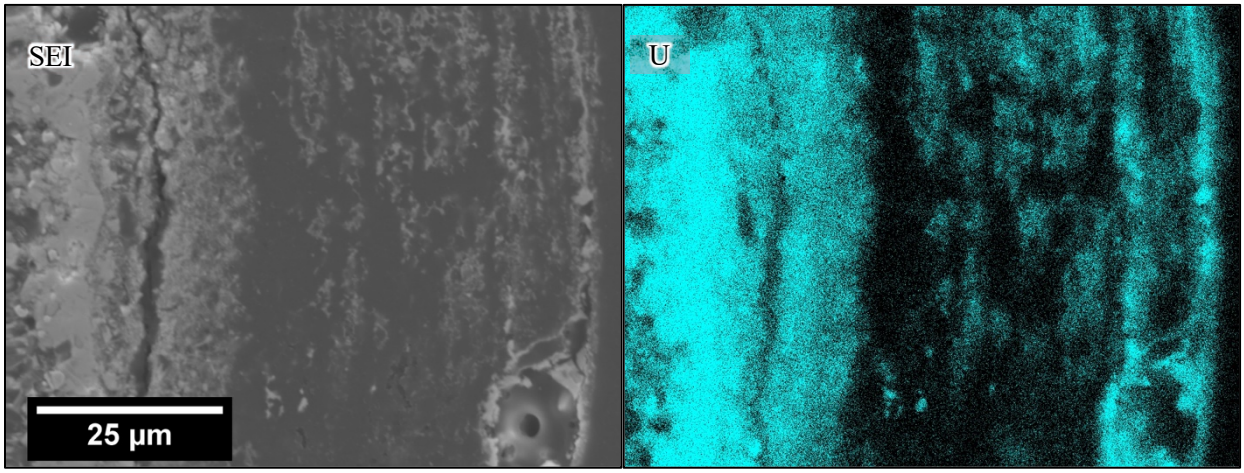

Figure 7-65. SEI image and corresponding EDS map of uranium in another region of the Particle 212-SP01 buffer layer.

8. CONCLUSION

Safety testing was completed at 1,800°C on high-temperature Capsule 2 AGR-2 UCO Compact 2-1-2. The compact was held at 1,800°C for ~300 h. Cesium release from the compact at the beginning of the test was relatively low at only ~2–3% of one particle-equivalent of ^{134}Cs. This indicated that there were no particles with defective or failed SiC at the start of the test. However, after 100–150 h at 1,800°C, a single particle experienced through-layer degradation of the SiC. This resulted in a sharp increase in the rate of cesium collected on the deposition cups due to cesium passing through the degraded SiC of the failed particle. Cesium release from the failed particle continued at a high rate for a period that spanned several 24-h deposition cup changes, and then the cesium release rate decreased due to depletion of the failed particle's cesium inventory. By the end of the test, the cesium release rate was almost down to the observed rate before the particle failed. The total ^{134}Cs release during the safety test was ~74% of one particle-equivalent, of which ~71% appeared to come from the failed particle. Krypton release remained low throughout the test, indicating that the single failed-SiC particle remained gas tight.

After the safety test, the compact was deconsolidated, and particles were scanned with the IMGA. One particle, Particle 212-SP01, was found that had lost enough cesium to account for the safety test release, and x-ray tomography showed localized degradation of the SiC layer. Subsequent optical microscopy and SEM analysis of a polished cross section through the failed-SiC particle revealed the failure to be related to a crack through the IPyC that exposed the SiC layer to localized attack by fission products passing through the crack in the IPyC.

Post-safety test destructive PIE included DLBL analysis of exposed fission products and actinides remaining in the compact after safety testing. There were no indications for exposed kernels in the DLBL solutions before or after the IMGA survey that would indicate any particles with failed or defective SiC layers were missed by the IMGA survey. This supported the conclusion that only one particle exhibited SiC failure during the safety test.

Gamma counting with a 6 h live time was performed on 46 randomly selected particles. Six particles were selected from this RS-series for examination with XCT and materialographic methods that included (1) optical microscopy, (2) SEM imaging with both scanning electrons and backscattered electrons, and (3) EDS analysis to study the composition of fission products and actinides clustered in the TRISO layers. Observations were consistent with previous studies of AGR-2 Capsule 2 compacts and other AGR-1 and AGR-2 compacts exposed to 1,800°C safety testing (Gerczak et al. 2018).

Particle 212-SP01 was examined by SEM imaging and EDS analysis. There were several sites where the SiC was partially degraded by reaction with metallic species migrating from the kernel through compromised IPyC regions, and there was one large through-layer SiC degradation feature. This through-layer SiC degradation and several SiC cracks were the cause of the failure of the SiC layer to retain cesium. Regions of degraded SiC were carbon-rich and silicon-depleted. Cracks in the IPyC layer appeared to have acted as pathways for accelerated transport of metallic species to the SiC and reaction products away from the degraded SiC. These reaction products, which were metal silicides containing predominantly ruthenium, uranium, and rhodium, were found in the degraded SiC, in the IPyC cracks, in the IPyC surrounding the cracks, on the buffer side of the IPyC, and in the OPyC layer adjacent to the through-layer SiC degradation feature. Palladium was not a major constituent of the metal silicides observed in Particle 212-SP01 but may still have been a primary reaction species, based on its observed role in SiC degradation leading to SiC failure in other TRISO particles (Hunn et al. 2014). Multiple observations of TRISO particles after 1,800°C safety testing have indicated that palladium does not remain in the particles at this temperature.

9. REFERENCES

Baldwin, C. A., J. D. Hunn, R. N. Morris, F. C. Montgomery, C. M. Silva, and P. A. Demkowicz. 2012. "First Elevated Temperature Performance Testing of Coated Particle Fuel Compacts from the AGR-1 Irradiation Experiment." Paper HTR2012-3-027. *Proc. 6th International Topical Meeting on High Temperature Reactor Technology (HTR-2012)*, Tokyo, Japan, October 28–November 1, 2012. Also published in *Nucl. Eng. Des.* 271: 131–141.

Barnes, C. M. and D. W. Marshall. 2009. *FY 2009 Particle Fabrication and Coater Test Report.* INL/EXT-09-16545, Revision 0. Idaho Falls, ID: Idaho National Laboratory.

Collin, B. P. 2014. *AGR-2 Irradiation Test Final As-Run Report.* INL/EXT-14-32277, Revision 2. Idaho Falls, ID: Idaho National Laboratory.

Demkowicz, P. A. 2013. *AGR-2 Post Irradiation Examination Plan.* PLN-4616, Revision 0. Idaho Falls, ID: Idaho National Laboratory.

Demkowicz, P. A., J. D. Hunn, R. N. Morris, I. J. van Rooyen, T. J. Gerczak, J. M. Harp, and S. A. Ploger. 2015. *AGR-1 Post Irradiation Examination Final Report.* INL/EXT-15-36407, Revision 0. Idaho Falls, ID: Idaho National Laboratory.

Demkowicz, P. A. and J. D. Stempien. 2019. *AGR-2 Irradiation Experiment Fission Product Mass Balance.* INL/EXT-19-53559, Revision 0. Idaho Falls, ID: Idaho National Laboratory.

Gerczak, T. J., J. D. Hunn, R. A. Lowden, and T. R. Allen. 2016. "SiC Layer Microstructure in AGR-1 and AGR-2 TRISO Fuel Particles and the Influence of Its Variation on the Effective Diffusion of Key Fission Products." *J. Nucl. Mater.* 480: 1–14.

Gerczak, T. J., J. D. Hunn, R. N. Morris, F. C. Montgomery, D. J. Skitt, C. A. Baldwin, J. A. Dyer, and B. D. Eckhart. 2018. "Analysis of Fission Product Distribution and Composition in the TRISO Layers of AGR-2 Fuel," Paper HTR2018-0048. *Proc. 9th International Topical Meeting on High Temperature Reactor Technology (HTR-2018)*, Warsaw, Poland, October 8–10, 2018.

Harp, J. M., P. A. Demkowicz, P. L. Winston, and J. W. Sterbentz. 2014. "An Analysis of Nuclear Fuel Burnup in the AGR-1 TRISO Fuel Experiment Using Gamma Spectrometry, Mass Spectrometry, and Computational Simulation Techniques." *Nucl. Eng. Des.* 278: 395–405.

Harp, J. M., P. A. Demkowicz, and J. D. Stempien. 2016. "Fission Product Inventory and Burnup Evaluation of the AGR-2 Irradiation by Gamma Spectrometry", Paper HTR2016-18593. *Proc. 8th International Topical Meeting on High Temperature Reactor Technology (HTR-2016)*, Las Vegas, Nevada, November 6–10, 2016. Also published in *Nucl. Eng. Des.* 329: 134–141.

Hawkes, G. L. 2014. *AGR-2 Daily As-Run Thermal Analyses.* INL/ECAR-2476, Revision 1. Idaho Falls, ID: Idaho National Laboratory.

Hunn, J. D. and R. A. Lowden. 2006. *Data Compilation for AGR-1 Variant 3 Coated Particle Composite LEU01-49T.* ORNL/TM-2006/022, Revision 0. Oak Ridge, TN: Oak Ridge National Laboratory.

Hunn, J. D. 2010. *AGR-2 Fuel Compacts Information Summary: Prepared for the NRC MELCOR Project*. ORNL/TM-2010/296, Revision 1. Oak Ridge, TN: Oak Ridge National Laboratory.

Hunn, J. D., F. C. Montgomery, and P. J. Pappano. 2010a. *Data Compilation for AGR-2 UCO Variant Compact Lot LEU09-OP2-Z.* ORNL/TM-2010/017, Revision 1. Oak Ridge, TN: Oak Ridge National Laboratory.

Hunn, J. D., F. C. Montgomery, and P. J. Pappano. 2010b. *Data Compilation for AGR-2 UO_2 Compact Lot LEU11-OP2-Z.* ORNL/TM-2010/055, Revision 1. Oak Ridge, TN: Oak Ridge National Laboratory.

Hunn, J. D., T. W. Savage, and C. M. Silva. 2010. *AGR-2 Fuel Compact Pre-Irradiation Characterization Summary Report.* ORNL/TM-2010/226, Revision 0. Oak Ridge, TN: Oak Ridge National Laboratory.

Hunn, J. D., T. W. Savage, and C. M. Silva. 2012. *AGR-1 Fuel Compact Pre-Irradiation Characterization Summary Report.* ORNL/TM-2012/295, Revision 0. Oak Ridge, TN: Oak Ridge National Laboratory.

Hunn, J. D., R. N. Morris, C. A. Baldwin, F. C. Montgomery, C. M. Silva, and T. J. Gerczak. 2013. *AGR-1 Irradiated Compact 4-4-2 PIE Report: Evaluation of As-Irradiated Fuel Performance with Leach-Burn-Leach, IMGA, Materialography, and X-ray Tomography*. ORNL/TM-2013/236, Revision 0. Oak Ridge, TN: Oak Ridge National Laboratory.

Hunn, J. D., R. N. Morris, C. A. Baldwin, F. C. Montgomery. 2013b. *Safety Tests on Irradiated AGR-1 Compacts 5-3-3 and 5-1-3*. ORNL/LTR-2013/603, Revision 0. Oak Ridge, TN: Oak Ridge National Laboratory.

Hunn, J. D., R. N. Morris, C. A. Baldwin, F. C. Montgomery, C. M. Silva, and T. J. Gerczak. 2013c. *PIE on Three Irradiated AGR-1 Compacts in FY2013*. ORNL/LTR-2013/291, Revision 0. Oak Ridge, TN: Oak Ridge National Laboratory.

Hunn, J. D., C. A. Baldwin, T. J. Gerczak, F. C. Montgomery, R. N. Morris, C. M. Silva, P. A. Demkowicz, J. M. Harp, S. A. Ploger, I. J. van Rooyen, and K. E. Wright. 2014. "Detection and Analysis of Particles with Failed SiC in AGR-1 Fuel Compacts." Paper HTR2014-31254. *Proc. 7th International Topical Meeting on High Temperature Reactor Technology (HTR-2014)*, Weihai, China, October 27–31, 2014. Also published in *Nucl. Eng. Des.* 360: 36–46.

Hunn, J. D., R. N. Morris, C. A. Baldwin, and F. C. Montgomery. 2015. *Safety-Testing of AGR-2 UO_2 Compacts 3-3-2 and 3-4-2*. ORNL/TM-2015/388, Revision 0. Oak Ridge, TN: Oak Ridge National Laboratory.

Hunn, J. D., R. N. Morris, C. A. Baldwin, and F. C. Montgomery. 2016a. *Safety-Testing of AGR-2 UCO Compacts 5-2-2, 2-2-2, and 5-4-1*. ORNL/TM-2016/423, Revision 1. Oak Ridge, TN: Oak Ridge National Laboratory.

Hunn, J. D., C. A. Baldwin, F. C. Montgomery, T. J. Gerczak, R. N. Morris, G. W. Helmreich, P. A. Demkowicz, J. M. Harp, and J. D. Stempien. 2016b. "Initial Examination of Fuel Compacts and TRISO Particles from the US AGR-2 Irradiation Test." Paper HTR2016-18443. *Proc. 8th International Topical Meeting on High Temperature Reactor Technology (HTR-2016)*, Las Vegas, Nevada, November 6–10, 2016. Also published in *Nucl. Eng. Design* 329: 89–101.

Hunn, J. D., R. N. Morris, C. A. Baldwin, Z. M. Burns, F. C. Montgomery, and D. J. Skitt. 2017. *Safety-Testing of AGR-2 UCO Compacts 6-4-2 and 2-3-1*. ORNL/TM-2017/439, Revision 0. Oak Ridge, TN: Oak Ridge National Laboratory.

Hunn, J. D., R. N. Morris, F. C. Montgomery, T. J. Gerczak, D. J. Skitt, G. W. Helmreich, B. D. Eckhart, and Z. M. Burns. 2018a. *Safety-Testing and Post-Safety-Test Examination of AGR-2 UCO Compact 2-3-2 and AGR-2 UO_2 Compact 3-4-1*. ORNL/TM-2018/956, Revision 0. Oak Ridge, TN: Oak Ridge National Laboratory.

Hunn, J. D., R. N. Morris, F. C. Montgomery, T. J. Gerczak, D. J. Skitt, C. A. Baldwin, J. A. Dyer, G. W. Helmreich, B. D. Eckhart, Z. M. Burns, P. A. Demkowicz, and J. D. Stempien. 2018b. "Post-Irradiation Examination and Safety Testing of US AGR-2 Irradiation Test Compacts." Paper HTR2018-0010. *Proc. 9th International Topical Meeting on High Temperature Reactor Technology (HTR-2018)*, Warsaw, Poland, October 8–10, 2018.

Hunn, J. D., T. J. Gerczak, F. C. Montgomery, D. J. Skitt, C. A. Baldwin, G. W. Helmreich, B. D. Eckhart, and J. A. Dyer. 2018c. *AGR-2 Safety-Tested UCO Compact 6-4-2 PIE Report*. ORNL/TM-2018/864, Revision 0. Oak Ridge, TN: Oak Ridge National Laboratory.

Hunn, J. D., T. J. Gerczak, R. N. Morris, F. C. Montgomery, D. J. Skitt, B. D. Eckhart, Z. M. Burns. 2019. *Safety-Testing and Destructive Examination of AGR-2 UCO Compact 6-4-3*. ORNL/TM-2019/1200, Revision 0. Oak Ridge, TN: Oak Ridge National Laboratory.

Lowden, R. A. 2006. *Fabrication of Baseline and Variant Particle Fuel for AGR-1*. ORNL/CF-2006/02, Revision 0. Oak Ridge, TN: Oak Ridge National Laboratory.

Morris, R. N., P. A. Demkowicz, J. D. Hunn, C. A. Baldwin, and E. L. Reber. 2014. "Performance of AGR-1 High Temperature Reactor Fuel During Post-Irradiation Heating Tests." Paper HTR2014-31135. *Proc. 7th International Topical Meeting on High Temperature Reactor Technology (HTR-2014)*, Weihai, China, October 27–31, 2014. Also published in *Nucl. Eng. Des.* 306: 24–35.

Phillips, J. A., C. M. Barnes, and J. D. Hunn. 2010. "Fabrication and Comparison of Fuels for Advanced Gas Reactor Irradiation Tests." Paper HTR2010-236. *Proc. 5th International Topical Meeting on High Temperature Reactor Technology (HTR-2010)*, Prague, Czech Republic, October 18–20, 2010.

Sterbentz, J. W. 2014. *JMOCUP As-Run Daily Depletion Calculation for the AGR-2 Experiment in the ATR B-12 Position.* ECAR-2066, Revision 2. Idaho Falls, ID: Idaho National Laboratory.